This is to certify that the

dissertation entitled

TEMPERATURE AND CONCENTRATION OF IONIC
AND NEUTRAL SPECIES IN
RESONANT MICROWAVE CAVITY PLASMA DISCHARGES

presented by

GREGORY LOUIS KING

has been accepted towards fulfillment
of the requirements for

Ph.D. **degree in** Electrical Engineering

Timothy Gutpa
Major professor

Date August 31, 1994

TEMPERATURE AND CONCENTRATION OF IONIC AND NEUTRAL SPECIES IN RESONANT MICROWAVE CAVITY PLASMA DISCHARGES

By

Gregory Louis King

A DISSERTATION

Submitted to
Michigan State University
in partial fulfillment of the requirements
for the degree of

DOCTOR OF PHILOSOPHY

Department of Electrical Engineering

1994

ABSTRACT

TEMPERATURE AND CONCENTRATION OF IONIC
AND NEUTRAL SPECIES IN
RESONANT MICROWAVE CAVITY PLASMA DISCHARGES

By

Gregory Louis King

Microwave resonant cavity plasma discharges are currently being utilized for a wide variety of processing applications. Multipolar electron cyclotron resonance (ECR) discharges are being used in semiconductor processing applications. Resonant cavity discharges without the ECR magnets are being used for diamond thin film deposition on a variety of surfaces. To facilitate successful processing, both technologies place certain requirements on the plasma discharge. The semiconductor etching application requires an activated gas--dissociation and/or ionization of a complex molecule--and a controllable, low energy ion distribution arriving at the surface. The deposition technology requires a controlled processing surface temperature and also, the proper plasma species for the specified growth to occur.

In order to examine the properties of the multipolar ECR discharge related to successful etching a number of diagnostic techniques were utilized. To examine the energy properties of the ions in the discharge laser induced fluorescence (LIF) experiments were developed. LIF provides a non-intrusive means of examining the energy of a particular ion in any region of the discharge. The neutral species in the discharge were examined using optical emission spectroscopy. From the emission spectrum of the neutral species, the temperature of the background gas is determined.

The diamond deposition discharge has been experimentally evaluated using optical emission spectroscopy techniques. Atomic translational and electronic temperatures,

as well as molecular rotational temperatures have been determined from the optical emission. Hydrogen based discharges have been examined over a wide pressure range. In the pressure ranges where diamond growth has been demonstrated the discharge contained methane and the temperature of the processing surface was also determined.

All of the diagnostics mentioned have been performed under the guidance of sets of statistically designed experiments. The number of experimental runs was reduced while maximizing the amount of information gathered. Hence, the experimental cost associated with determining the plasma properties was reduced. Response surfaces were developed relating the diagnostic results to the most significant experimental factors. These surfaces provide an excellent means for verification of computational models and provide data for subsequent reactor design.

For Jim

ACKNOWLEDGMENTS

No large task is completed alone. This dissertation is no exception. Dr. Timothy Grotjohn has been my guide, my mentor. His consultation, his suggestions and his patience are greatly appreciated. He provided the impetus for the work presented here, the means to complete the task and then opened his door for countless hours of discussion. I would like to thank Dr. Jes Asmussen and Dr. Donnie Reinhard for their insights into the research presented and their willingness to discuss and advise me on that research. Thank you to Dr. Jeffery Ledford for his comments and willingness to read the manuscript. To Aseem Srivastava, Peng-Un Mak and Dr. Jie Zhang, special thanks for the lab discussions which furthered the work here.

TABLE OF CONTENTS

CHAPTER 4

Diamond Deposition Discharge Diagnostics

CHAPTER 5

Hydrogen-based Discharge Diagnostics at Extended Pressures

CHAPTER 6

Argon/Sulfur Hexafluoride Discharge Diagnostics

LIST OF TABLES

LIST OF FIGURES

Chapter 1

Introduction

1.1 Motivation

Microwave cavity plasma reactors have shown their ability to produce useful discharges for depositing diamond thin films as well as for silicon and III-V etching. In etching applications, low pressure, low temperature discharges have demonstrated excellent etching of silicon with feature sizes of 0.2 micron in SF_6/Ar gas mixtures [1] and similar results in etching of GaAs, AlGaAs and GaSb in CH_4/H_2/Ar chemistries [2]. For depositing diamond films the microwave plasma has established its ability to grow high quality films at moderate pressures (10-100 Torr) [3] and has shown potential to grow diamond films at lower pressures (0.1-10 Torr) [4].

The etching applications utilize electron cyclotron resonance (ECR) microwave cavity reactors. The microwave energy in the presence of a static magnetic field is coupled to the electron gas which in turn ionizes the neutral gas creating the plasma. The diamond deposition applications apply the microwave cavity technology without the static magnetic field. The plasma is created and maintained, without aid of electron cyclotron resonance, using purely collisional excitation.

The plasma state in general is unique in that it consists of appreciable quantities of three distinct but intermixed subgases. Ions, electrons and neutral species interact and react with one another and the surfaces confining the plasma. Understanding how the microwave plasma behaves requires an understanding of each of these subgases. The ion

energy, the distribution of electrons and the density of neutral species are examples of properties that can be measured and examined through a variety of diagnostic methods.

The electron gas serves as the ignition gas and the basis of much of the kinetics in the plasma. In the resonant cavity discharges, the microwave energy is coupled into the electron gas and is disbursed to the neutral gas through elastic collisions and inelastic ionizing collisions. A knowledge of the electron kinetics is essential to understand the kinetics of other plasma species.

To understand most processing discharges a detailed knowledge of the ions in the plasma is necessary. The density, energy and velocity of these plasma workhorses and how they are effected by external variables such as reactor size, input parameters (microwave power, pressure, gas flow) and ECR magnet configuration will determine how well the plasma reactor performs especially in ion-enhanced etching applications.

The radical and neutral species may play an important role in growing useful diamond films at useful rates. The mixtures of gases in diamond thin film discharges is known to affect the growth quality and growth rate of the films. Since the plasmas studied here are weakly ionized, the number of neutral species present is significant and worthy of study.

1.2 Objective

The consummate goal of any work in this area is the successful design of the ideal processing reactor and a materials manufacturing process using the reactor. For instance, the ideal reactor for etching applications would produce a controllable low energy, uniform beam of ions to the processing surface in useful numbers for efficient production. This study, though, has a more succinct goal of an improved plasma reactor designed for etching and for the deposition of diamond thin films. Design of this reactor would be hastened by the ability to model the physical and chemical properties of the plasma. These

reactors have been in use for a number of years now, so there is access to the most recent iterations toward the goal. Study of the current design can logically lead to a useful, accurate model, an improved design, and, ultimately, to the optimum design.

The complete processing apparatus is shown schematically in Figure 1. Paths one and two shown on Figure 1 symbolize the simplest view of the materials processing scheme. Varying the external inputs, such as microwave power, will have obvious effects on the outputs, such as etch rate. A more detailed analysis of the reactor would examine paths three and four since path one is only a virtual path. The external inputs actually directly affect the internal variables--path three--such as species energy and concentrations. These factors then, in turn, facilitate the processing--path four. Additionally, process control can utilize the knowledge of observable internal variables to modify the inputs as necessary for a specific output--path five.

More specifically, meeting the goal of an improved plasma reactor and a useful model partially entails determining the role of the internal variables, such as ion and neutral species energies and concentrations, within both the plasma source and downstream from the source in the processing region. For example, within the source, determining the probable excitation processes is important in modeling the discharge properly. While in the processing region, understanding the energy and velocity of species in the vicinity of a processing surface and the interaction of the species with that surface will further the correct modeling of that region.

Beyond determining the role of these species, the goal includes discovering what controls the energy, velocity and density of each particle. The effects of discharge parameters such as microwave power, pressure and gas flow on ion motion, neutral temperature or species density will determine the role of external inputs in the excitation process or in the chemical activity at a processing surface. These elements are crucial to modeling the

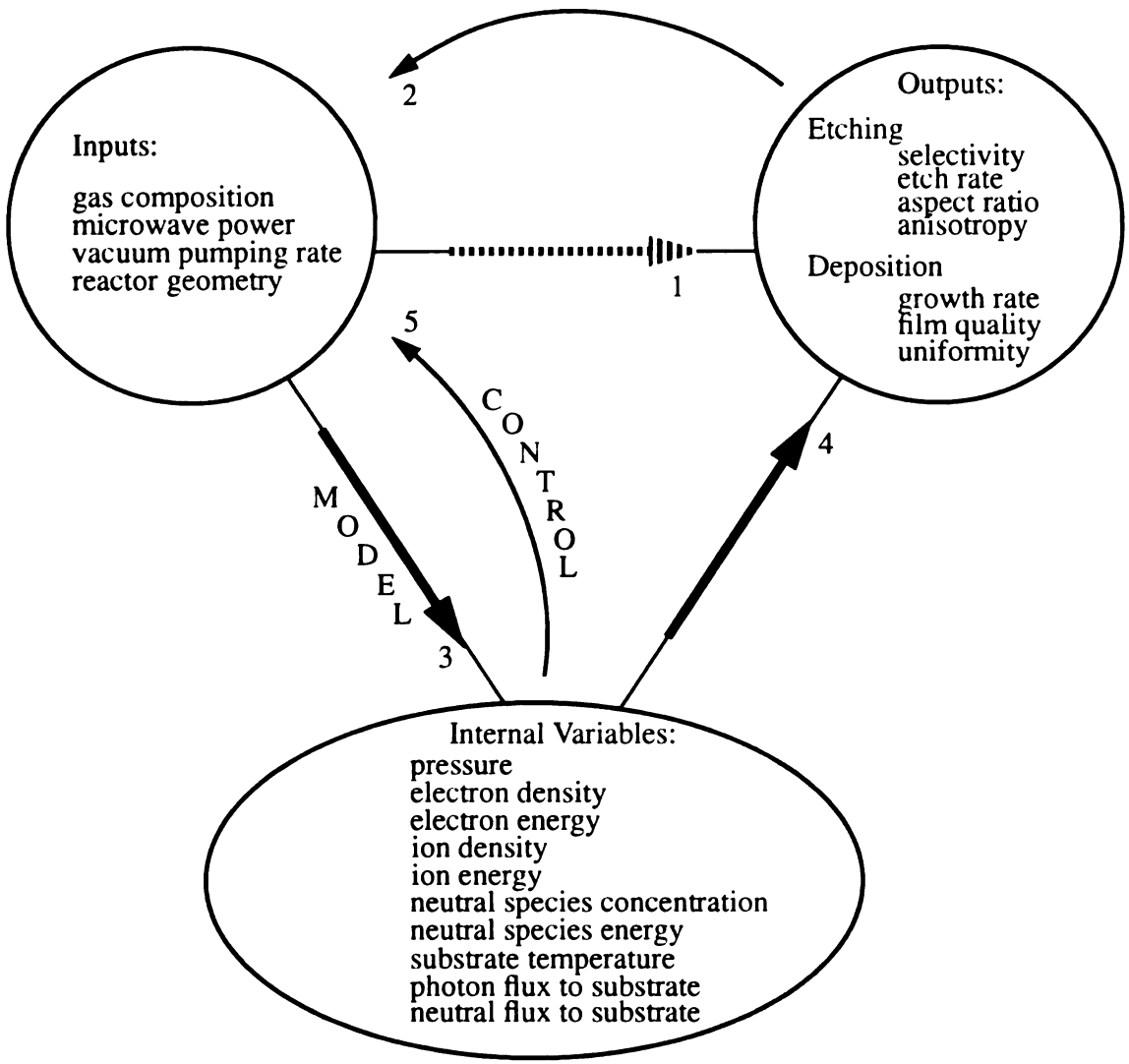

Figure 1.1: Microwave processing of materials schematic. 1 and 2: Processing path for the optimized reactor. 3: Path representing the interaction between the reactor inputs and the internal variables. 4: Interaction between the internal variables and the output variables. 5: Path showing the process control basedon internal variables.

plasma correctly and a correct model is a paramount step toward designing a better plasma reactor.

The objective of this study is to determine the densities and energies of ion and radical species in the processing region and at the substrate in CH_4/H_2 diamond deposition discharges, pure hydrogen discharges and SF_6/Ar silicon etching discharges created in a microwave plasma reactor. Modeling of the diamond deposition discharge will focus on two aspects: (1) the concentration of hydrogen species, in particular, atomic hydrogen and (2) the energy mix within the methane-hydrogen discharges in terms of the temperature of the consituent subgasses. Plasma diagnostic studies performed include H_2/CH_4 discharge diagnostics at moderate pressures (1-100 Torr) directed at atomic hydrogen concentration, various plasma temperatures, and species identification. The pure hydrogen discharge is examined at discharge pressures less than 1 Torr where current research is moving toward growing films of diamond on delicate substrates. Statistical models of low pressure SF_6/ Ar discharges (0.5-4 mTorr) will focus on plasma species energies and concentrations in the discharge source region. Low pressure argon and argon/sulfur hexafluoride discharge diagnostic measurements of ion energies and densities and neutral temperatures and concentrations will be performed to produce the model.

1.3 Dissertation outline

This work will focus on the use of nonintrusive optical plasma diagnostics to develop useful pictures of the materials processing plasma discharges. Chapter 2 describes optical diagnostics and statistical models in the literature. Chapter 3 discusses the discharge reactor and the use of statistical experimental design in plasma diagnostics. The discussion includes a tutortial in the use of the statistical principles such as analysis of variance to extract the most information from the data with a minimum of experiments. Chapter 3 also lays out the regression methods used to model the response of the diagnostic measurements to input parameters.

Chapters 4, 5 and 6 describe the results of the diagnostics of the three major experimental regimes. In Chapter 4, the temperature and concentration measurements in the moderate pressure diamond deposition discharge are pressented. This chapter details the optical emission spectroscopy methods and the statistical design of experiments. Chapter 5 applies the techniques developed in Chapter 4 to discharges operating in extended pressure regimes. The temperatures and concentrations of a higher pressure hydrogen/methane discharge are discussed as they relate to the diamond deposition discharge of Chapter 4. A low pressure hydrogen discharge is also discussed in Chapter 5 in terms of statistical models of hydrogen atomic temperatures. Chapter 6 presents the results of the laser induced fluorescence and neutral temperature measurements in the SF_6/Ar low pressure ECR discharges. The response of these plasma properties to discharge input variables are statistically modeled. Finally, Chapter 7 sums up the research presented and discusses future experiments that may further increase the knowledge of these discharges.

Chapter 2

Plasma Diagnostics and Statistical Modeling in the Literature

2.0 Introduction to plasma discharge studies and modeling

A number of diagnostic tools will be utilized to reach the goals set up in Chapter 1. Many of these diagnostic tools are explained in the literature. Researchers in search of species densities, energies and fluxes have used optical techniques, laser techniques and various other techniques. The literature describes the use of statistically designed experiments and also describes some models of H_2/CH_4 and Ar/SF_6 discharges in various reactor types. A few of these tools and models are described here.

For the purposes of this review the research literature can be divided into three types. In the first type, the processing literature describes the reactor briefly but is used to discuss results of processing: etch rates, uniformity, deposition times, etc. [5, 6, 7, 8, 9]. In the seconde type, the reactor literature focuses on the particular reactor and discusses the theory of operation [10, 11, 12]. Descriptions of ECR theory, divergent magnetic fields and sheath voltages are some of the topics in these papers. The third type of research paper, important for the background of this dissertation, is the diagnostic paper. The literature here, describes the techniques used to diagnose the properties of a particular reactor with specific attention to optical non-intrusive techniques. Often the papers in this group focus primarily on the theory of the diagnostic and simply refer to the reactor literature to describe the theory of operation. These works provide a valuable resource for this proposal. Some of the techniques described, suitably modified, will be proposed for use in diagnosing microwave cavity reactors.

2.1 Optical emission techniques in the literature

Study of the natural emission of the discharge is probably the most widely utilized optical plasma diagnostic technique [13]. A number of papers discuss the general aspects of optical emission spectroscopy (OES) [14, 15, 16, 17, 18]. The characteristic spectra found in OES is used to identify the species present in the discharge. For example, in the literature discussing plasma processing of silicon, OES is used to determine the effects of the dissociation of hydrogen in closed silane-germane rf discharges by examining the changes in various hydrogen emission lines with time [19]. The researchers found the intensity of hydrogen emission increased with time. This fact, related to the dissociation of SiH_4 and GeH_4, was interesting since the characteristic Si and Ge peaks did not increase at the same rate in these closed vessels. This information found from simply examining the natural emission led these researchers to other diagnostic techniques to determine where the hydrogen species originated. This paper also describes using LIF and CARS laser techniques to unravel the mystery.

OES can also be used to determine the effects of external parameters on the species in the discharge. External magnetic fields play an important role in a variety of plasma reactors. For example, reactive ion etching (RIE) utilizing external magnetic fields for electron confinement has been studied using OES and other optical techniques [20]. The intensity of the emission from a number of excited atoms such as argon and fluorine, was examined versus magnetic field strength in a CF_4 etching plasma. The intensity of the emission of the atoms increased with increasing magnetic field leading these researchers to conclude the rate of electronic excitation increases as a consequence of the increased electron confinement from the magnetic field.

A quantitative form of optical emission spectroscopy, commonly called actinometry, is used to follow trends in the concentration of the ground state of plasma species. Developed by Coburn and Chen [21, 22], described by Miller [23] and Dreyfus, et al. [14],

actinometry involves using emission intensity ratios to relate the known concentration of one species (the actinometer) to the concentration of the species under investigation. Sulfur hexafluoride discharges used in etching applications have been studied using actinometry. d'Agostino, et al. [24, 25] describe using actinometry to examine ground state fluorine densities and electron energy distributions. These studies also tested the applicability of actinometry by comparing the results with titration experiments in the reactor studied. Reference [24] discusses the use of actinometry as a probe of the electron energy distribution by using a range of actinometer gases. If the gases are purely excited by similar electron collisions, the actinometry intensity ratio depends on the excitation energy of each different actinometer. Using a range of gases, the ratio is then a probe of the electron energy. This paper also discusses the use of nitrogen as an actinometer to trace oxygen atoms.

Studying He-CH_4 discharges, de la Cal, et al. [26] used actinometry and mass spectrometry to correlate the carbon deposition rate of their discharge to the observed emission intensities of two spectral lines. They probed the hydrogen Balmer-β line at 486 nm and used the argon neutral line at 750 nm for the actinometer. These same lines are used for the actinometry measurements presented in Chapter 4.

R.A. Gottscho, et al. [15] and d'Agostino, et al. [27] describe the use of actinometry in CCl_4 discharges. Gottscho, et al. found that actinometry failed to track free radical concentrations in their discharges. They compared relative laser induced fluorescence measurements of CCl to their actinometric measurements and found the two did not agree. The possible explanation here is that the CCl radical can be formed in many ways. The energetic electron that excites the nitrogen is not necessarily the same one that forms the CCl radical. d'Agostino, et al., in a similar set of experiments, described the simultaneous use of several different actinometers to probe a wide range of electron energies to correlate to the CCl concentration.

Another use of plasma discharges is in growing polymer films. Durant, et. al. [28] describe incorporating actinometric measurements of hydrogen and fluorine atom concentration into their electron distribution diagnostics of C_2H_2/SF_6 rf discharges. They also correlate a change in CH concentration measured using actinometry to the quality of fluorinated organic films grown in these discharges.

Beyond concentration and species identification, the literature describes utilizing OES to obtain species temperature and energy measurements. T. A. Miller [23] describes obtaining hydrogen translational energies from measurements of the Doppler broadened width of the emission line. Miller points out that instruments with low resolution used to make the measurement may not be able to resolve true Doppler width in cool discharges. To increase resolution, Hopwood and Asmussen [29] utilize an interferometer. They are able to measure Doppler shifts with a resolution as low as 0.002 nm in multipolar electron cyclotron resonance microwave argon discharges. This technique is applied to the measurements in Chapter 6. McKillop, et al. [30] utilized a high resolution monochromator to measure argon neutral and argon ion translational energies with a resolution of 0.003 nm in a diverging field electron cyclotron resonance source.

Hydrogen temperature measurements from the hydrogen atom emissions in the Balmer series can be complicated by the fine structure splitting characteristic of these light atoms. Bruneteau, et al. [31] extended the earlier work of M. Pealat, et al. [32] in describing atomic temperature measurements in magnetic multicusp plasma generators. They assume the fine structure splitting of the Balmer lines is small enough that the line can still be considered to have a Gaussian shape. This assumption simplifies their measurements in that the fine structure splitting and the Gaussian shaped broadening from the instrumentation can easily be deconvulved from the measured spectra allowing a measure of the Doppler broadening and hence, the translational energy. This paper and Miller's paper [23] also note the existence of "wings" on their spectra which correspond to the light emitted

by higher energy hydrogen atoms. They are able to attribute the presence of these higher energy atoms to the dissociation of H_2 molecules in their discharges. Cappelli, et al. [33], in examining rf discharges, found high energy wings at certain positions in the discharge. They deduce that the only mechanism available to produce these fast hydrogen atoms is through neutralization of ions that have been accelerated through the sheath potential associated with one of their rf electrodes.

A single temperature is not sufficient to model most useful discharges. The distribution of energy among different species is open to many degrees of freedom. Davis and Gottscho [17] examined various temperatures in CCl_4 and CCl_4/N_2 discharges. By analyzing the emission spectrum arising from the molecular and vibrational energy transitions in CCl and N_2, they deduced vibrational and rotational temperatures. This is possible since the intensity of the characteristic branches in the spectra can be related through a Boltzmann-type equation to the temperature.

M. L. Passow, M. L. Brake, et al. [34] used OES to study nitrogen rotational and vibrational temperatures in air discharges produced in microwave cavity reactors. By measuring the characteristic second positive emission band system in the nitrogen spectra they determined the variation in rotational and vibrational temperatures versus changes in input parameters giving themselves valuable experimental data.

Molecular optical emission measurements can be equally important in discharges containing carbon species. The C_2 molecule has three well known emission bands arising from characteristic electronic, vibrational and rotational energy transitions. E. A. Rohlfing [35] describes examining the spectra from laser-vaporized carbon clusters to determine how these clusters are formed. He found, using OES, the spectra showed the characteristic Swan, Deslandres-d'Azambuja and Mulliken bands of C_2. Anselment, et al. [16] also found the C_2 Swan bands in their cluster source and they correlated the intensity of this band with the C_2 Swan band collisional excitation process in their source.

2.2 Laser techniques in the literature

The use of a coherent source of light to excite specific energy level transitions in particular plasma species has provided a number of diagnostics with high species selectivity and high spatially resolution. V. E. Bondybey and T. A. Miller [36] discuss one of the earliest published uses of lasers in plasma diagnostics. They describe using a laser to excite specific metastable energy states in the rare gas atoms. After excitation they collected the resulting fluoresced light when the atom relaxed. They used the technique, termed laser excited (induced) fluorescence, to determine the presence of the metastable species in dc discharges.

A more sophisticated form of laser induced fluorescence (LIF) has been utilized by a number of researchers to deduce species temperature and energy [37, 38, 39, 40], velocity [40, 41, 42, 43], and relative and absolute concentrations [44-56]. E.A. Den Hartog, et al. [38] have used the fluorescence spectra detected in a nitrogen plasma to deduce translational temperatures of N_2^+ ions assuming a Boltzmann distribution of energies. In multidipole gridded argon discharges, Goeckner, et al. [40] describe similar measurements of argon ion temperatures in pure argon discharges. Nakano, et al. [37] studied argon ion and neutral neon temperatures in divergent field ECR discharges. They examined discharges consisting of mixtures of gases and also noted the difficulty of artificial spectral broadening in the fluorescence posed by their diverging magnetic field.

When the energy distribution can not be assumed to be of the Boltzmann-type, the idea of temperature is not useful. Wright, et al. [43, 57] describe using LIF to determine velocity distributions by exploiting the Doppler effect in their measurements of atoms sputtered from a Zr target. Trevor, et al. [41] apply a similar technique to the study of a diverging field plasma source. Their experiments on metastable argon ions discovered the asymmetric fluorescence lineshapes characteristic of an ion under acceleration. They attribute this acceleration to the diverging magnetic and electrostatic fields in their source.

A very complete study of ion transport in the diverging field plasma source is presented by Sadeghi, et al. [58]. Their measurements of the velocity distribution of argon ions at various locations with respect to the diverging magnetic field were used to estimate the magnitude of electrostatic potentials. This same group of researchers also examined chlorine ion velocity distributions in these reactors [42]. Although Cl_2 is an electronegative gas, they found no significant difference in ion transport between the Cl_2 and argon discharges.

A number of papers in the literature discuss results of using LIF to measure hydrogen atom concentration with excellent spatial resolution [44, 45, 49, 50, 53]. The work of Preppernau, et al. [45] uses two-photon absorption laser induced fluorescence (TALIF) to measure relative ground state hydrogen concentration in RF discharges. They were able to temporally resolve their TALIF measurements to match the rf fluctuations of their discharge. The could then track H-atom concentrations as a function of the rf phase. They also report concentrations as a function of position, exploiting the superb spatial resolution of the laser technique.

Meier, et al. [49] utilize two-photon LIF in diagnosing a hot filament diamond deposition reactor. They report the ability to make absolute ground state density measurements of atomic hydrogen by calibrating the LIF signal to known atom concentrations in a separate discharge flow reactor which afforded them the use of titration for H-atom concentration measurements. They had to pay particular attention to the different rates of collisional quenching between the experimental and calibration reactors. They report H-atom concentrations versus CH_4 percent and distance from the filament.

Collart, et al. [54] report two photon LIF measurements of absolute oxygen atom concentration in an rf etching reactor. They calibrated their LIF signals to the LIF signals from a fixed amount of oxygen gas in a microwave cavity discharge. The amount of dissociation of O_2 was determined using a mass spectrometer attached to the microwave discharge. They determined from the LIF measurements that the O-atom natural emission

results from dissociated atoms and not excited ground state atoms which implies actinometry can not be applied in these reactors under these conditions.

Hansen, et al. [51] report a study of relative metastable and ground-state fluorine concentrations in pulsed CF_4 etching discharges. They studied the metastable fluorine concentrations using LIF and the ground-state concentrations were inferred from OES. They determined that the metastable state was rapidly quenched during the discharge pulse indicating few if any of these species are involved in etching in these reactors.

One of the first mentions of coherent anti-Stokes Raman spectroscopy (CARS) is made by Regnier and Taran in 1973 [59]. They point out that spontaneous Raman scattering has limitations: low scattered light levels, large sampling volumes, problems with background light. CARS does not encounter this problem since the stimulated scattered emission is brighter, the spatial resolution is on the order of the beam size (quite small), and the light is scattered from and collected at the focal point only.

Use of coherent anti-Stokes Raman spectroscopy to measure vibrational populations in hydrogen has been done by Pealat, et al. [60]. They motivate their work by noting that a high density of negative hydrogen ions have been found in their reactors which indicates the presence of highly vibrationally excited hydrogen molecules. They used the collected anti-Stokes radiation spectrum to deduce the populations of various vibrational energy levels and the rotational temperature. They estimate that about 2.5% of the hydrogen is vibrationally excited.

2.3 Miscellaneous diagnostic techniques in the literature

A few of the myriad of other diagnostic techniques include optical absorption spectroscopy (OAS) to detect the presence of neutral and ionic species, electron paramagnetic resonance (EPR) for measurement of absolute concentrations of atoms and free radical species, and titration for relative neutral species detection. These techniques appear in

the literature much less frequently with regard to plasma processing diagnostics then some of the previously mentioned diagnostics but they are worth mentioning for their unique natures.

Sakeek, et al. [61] discuss using OAS to detect species in laser produced plumes emanating from a $YBa_2Cu_3O_7$ target. Simply, OAS is the converse of optical emission spectroscopy. A laser beam is directed through the plasma and if a certain species is present in large enough quantities the laser can be tuned to match a characteristic absorption in that species. The laser light in this paper is monitored such that when the target is bombarded the amount of light absorbed at various spatial locations is recorded giving an indication of the species concentration at that point.

EPR spectroscopy utilizes magnetic fields to split the energy levels of paramagnetic species into their Zeeman components. The species must be in a microwave cavity field as well. When the Zeeman splitting matches the microwave frequency photons are absorbed and a drop in microwave power is detected. T. Miller [62] describes the use of EPR to determine the absolute concentration of excited O_2 molecules by calibrating the EPR spectra of a particular species with the EPR spectra of the ground state oxygen.

Another method of species concentration measurement is titration. Tserepi, et al. [63] use titration to calibrate their absolute ground state atomic hydrogen concentrations measured with two photon LIF. They measure the H-atom LIF signal intensity of a mixture of H_2/Ar in a microwave cavity discharge. At time zero NO_2 is added to the discharge. As more NO_2 is added the H- atom LIF intensity drops until the signal can no longer be resolved from the background emission. The amount of NO_2 at this point corresponds to the amount of H_2 in the discharge at time zero since the $NO_2 + H_2$ reaction is very fast and considered the dominant reaction in their experiment. They then use the LIF intensity at time zero and the corresponding H_2 concentration to calibrate their LIF concentration experiments.

2.4 Statistical modeling in the literature

There are a variety of types of discharge models in a number of papers in the literature. One type of model uses the tenets of plasma physics and a powerful computer to simulate the discharge properties. Research on these types of models can be broken down into those which [64, 65, 66] present general models based on specific reactor geometries or specific processes (etching, deposition) without specifying gases or gas mixtures. For example, a relatively complete model of DC and RF discharges is presented by Graves and Jensen [65]. They predict the electron and ion densities and electron energy in the entire discharge through a model that solves the electron and ion continuity equations and an equation for the electron energy. They did not consider any neutral species transport or reaction as a simplification.

Another general model is proposed by Zawaideh and Kim [66, 67]. Their model particularly examines the etching process. They begin by assuming four basic etching processes: physical sputtering by ions, chemical reaction at the surface by neutral particles, enhanced sputtering where neutral species react with the surface allowing ion sputtering, and enhanced chemical reaction where ion bombardment damages the surface to allow neutral species to react with the surface species. These assumptions drive the development of their model in that they must examine ion, as well as, neutral flux within the discharge and within the sheath regions above the surface. In terms of neutral flux within the plasma, all mechanisms which add or remove neutral species must be considered in addition to transport. Their model generalizes all the necessary particle balance equations for any chemistry and any geometry. They apply their model to CF_4 discharges etching SiO_2 and obtain a good agreement with actual etching work.

In diamond deposition reactors, much of the emphasis of modeling is placed on understanding the growth process and knowing which species in the plasma are necessary for growth. Bachman, et al. [68], in one the most referenced papers on this subject, present

a compilation of many of the gas compositions which have resulted in diamond growth in a variety of reactors. As a starting point for modeling studies, this paper points out a number of interesting experiments concerning the role of hydrocarbons, acetylene (C_2H_2), methane (CH_4) and plasma temperature in diamond growth. This paper also pointed out the need for further study.

Goodwin and Gavillet [69] modeled a hot filament diamond growth environment by solving the conservation equations for mass, momentum, energy and species concentration subject to somewhat idealized boundary conditions. They used a packaged chemical kinetics program (Chemkin-II) to evaluate the chemical properties. They found that only CH_3, C_2H_2, and CH_4 are present in significant quantities in their simulation to match the growth rate of an actual deposition. These results are consistent with the studies of Harris, et al. [70] who found that CH_3, C_2H_2, C_2H_4, and CH_4 are the most likely gaseous precursors to diamond growth.

Another approach to modeling has an experimental basis. Statistical modeling of the properties of discharges is a method of bringing the experiment to the computer--digitizing the response of the plasma. By running a controled and designed set of experiments on a specific reactor the response of the reactor to any number of input variables can be determined. Some papers in the literature use these models to predict processing results while another use is to verify the models based on the physical properties or to give input values or boundary conditions.

G.S. May, et. al. [71] have used statistical modeling and response surface methodology (RSM) techniques to model the etching characteristics of a discharge. They explain in great detail the process of setting up a fractional factorial design. They examined the effects of six factors on etch rate, uniformity, selectivity and anisotropy. A complete two level factorial design with six factors would require $2^6 = 64$ experimental runs but by neglecting the higher order interactions amongst the six factors they design a fractional

factorial experiment which requires $2^{6-1} = 32$ runs. They developed models (response surfaces) for each of the effects and presented the data, the models, and the errors in the fits.

Kibarian, et al. [72] used a different statistical technique (principal component analysis) to examine the factors behind yield loss during IC manufacturing. Principal componant analysis is a direct analysis technique. For example, certain factors will effect yield in this situation. By examining the data, the contribution to yield loss can be explained by a certain number of these factors. Principal component analysis essentially removes any correlation between factors and determines what percentage of yield loss is explained by each factor. Thus the yield loss is explained in a linear manner by the factors. Kibarian states this type of analysis is easier to learn than other statistical analysis techniques but there is are two underlying assumptions. Each factor must be independent and the factors must only effect the experiment in a linear fashion.

Chapter 3

Equipment, Experimental Method and Statistical Design of Experiments

3.0 Introduction to equipment and statistical design of experiments

This chapter describes the features of the resonant cavity microwave discharge apparatus relevant to the optical emission spectroscopy and laser spectroscopy experiments. The resonant cavity plasma equipment used for both the diamond deposition discharge and the hydrogen discharge and the multipolar ECR plasma system used for the argon/SF_6 discharge have been described in much detail elsewhere [80]. This chapter also includes a detailed description of the principles behind statistical experimental design and the interpretation of the results of a set of statistically designed experiments. The chapter concludes with a discussion of the statistically designed models used to describe the three discharges.

3.1 Multipolar ECR plasma reactor system

3.1.1 Introduction

The multipolar ECR source consists of a seven inch diameter microwave cavity, the baseplate and the quartz cavity (Figure 3.1 and Figures 3.2 and 3.3). The microwave cavity is a cylindrical resonant cavity which can be tuned with a sliding short and an adjustable input probe. The tuning process consists of matching the complex impedance of the cavity ($Z_{in} = R_{in} + jX_{in}$) to the transmission line impedance which carries the microwave energy from the microwave power source to the cavity. The cavity effectively directs intense microwave energy into the plasma source region. The baseplate contains the eight gas inlets and also a ring of eight rare earth magnets (Figure 3.2). Each magnet

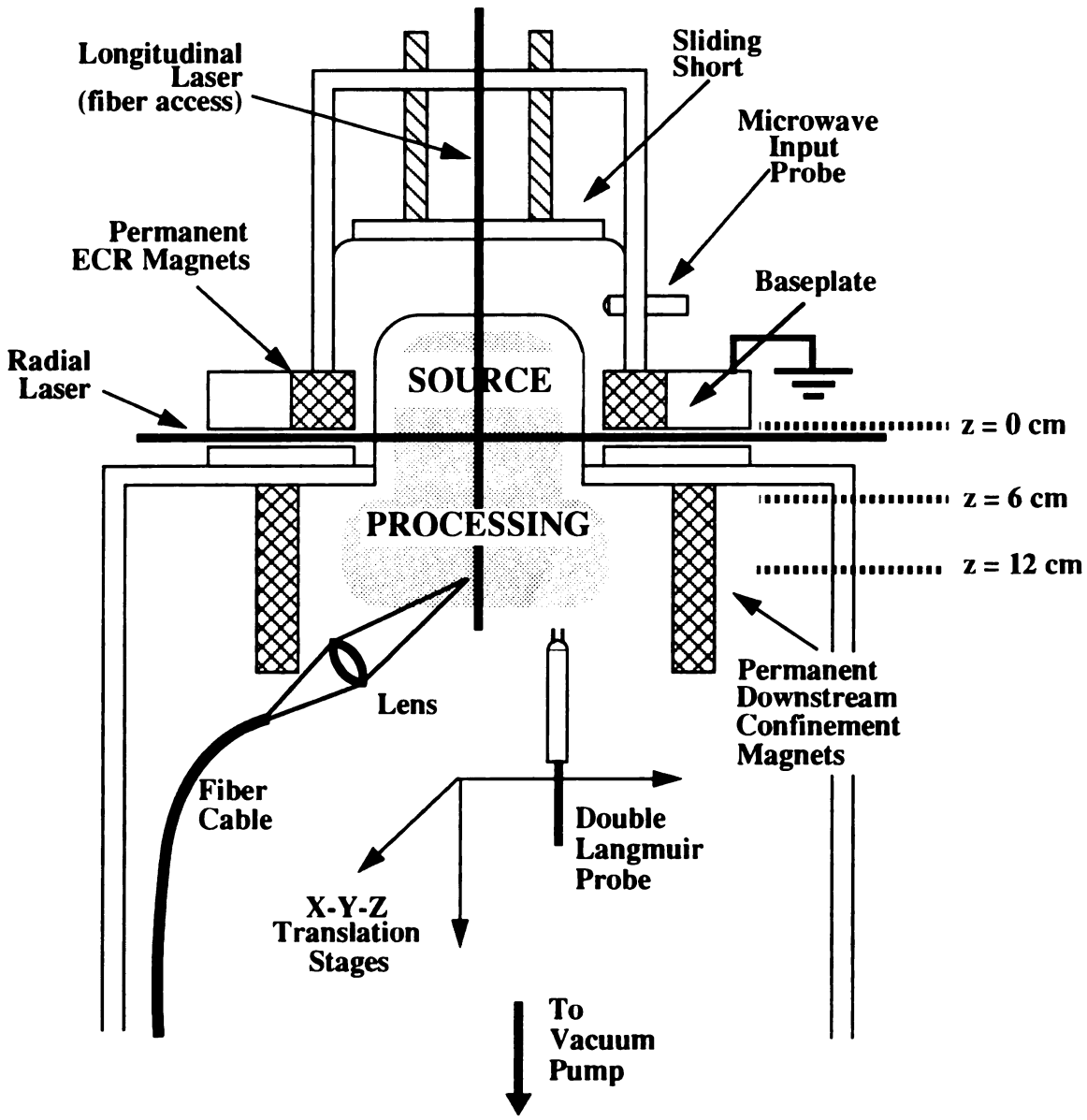

Figure 3.1: Multipolar ECR cavity and diagnostic equipment.

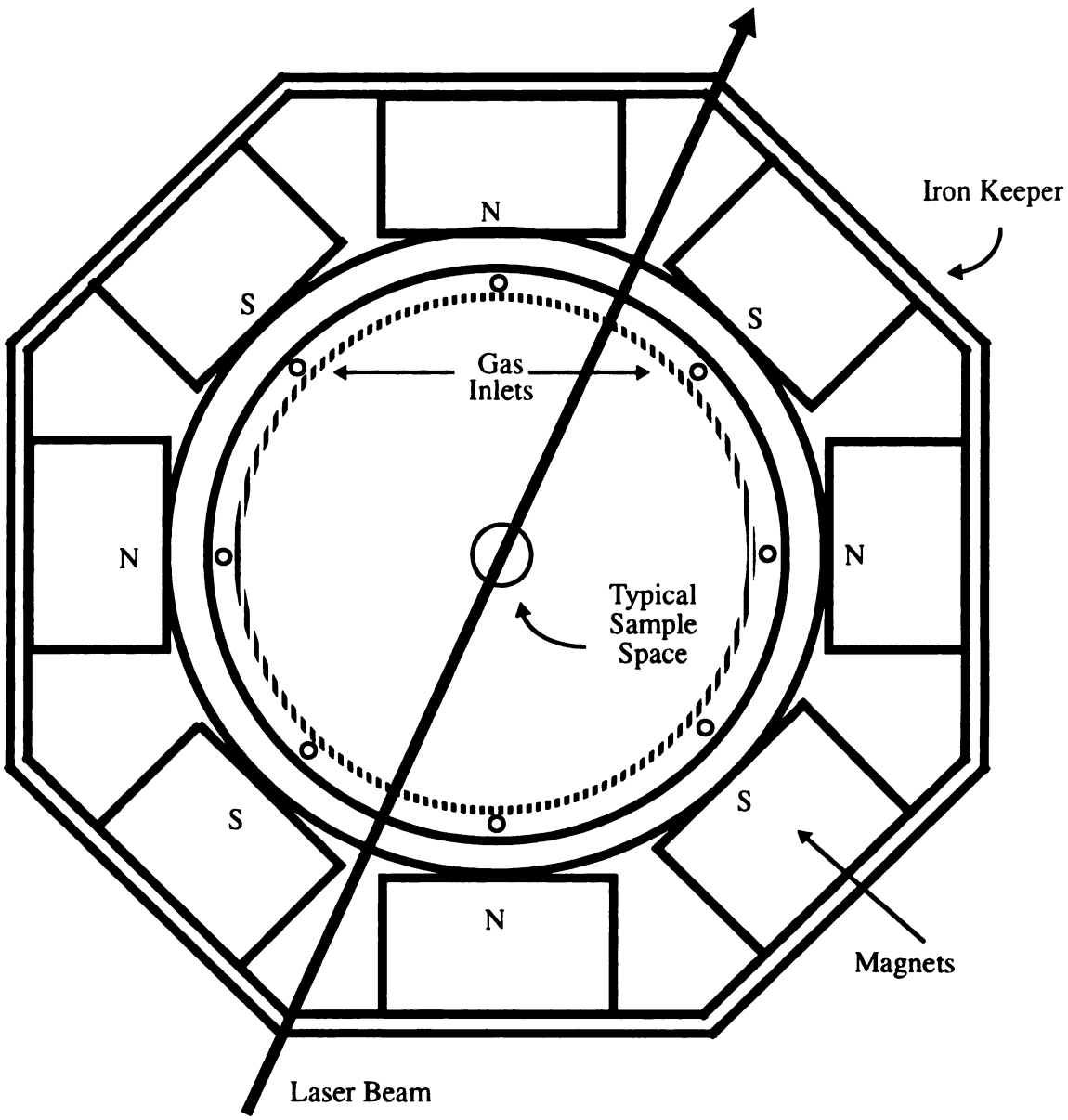

Figure 3.2: Multipolar ECR plasma reactor baseplate - top view.

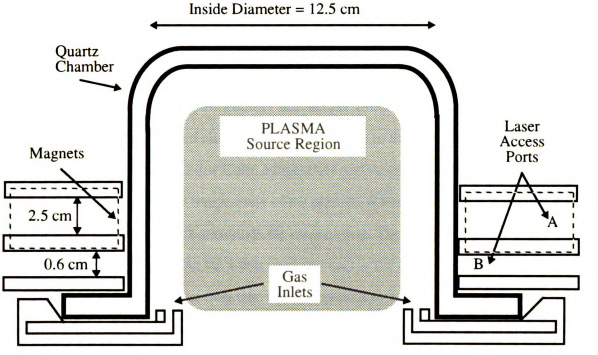

Figure 3.3: Multipolar ECR plasma reactor baseplate - side view. Laser port A is 2.5 cm high. Laser port B is 0.6 cm high. Dashed line indicates magnet locations.

measures two inches by one inch by one inch. These magnets create the ECR zones within the quartz cavity. A detailed description of the multipolar ECR plasma reactor is found in Reference [26].

3.1.2 The baseplate for the multipolar ECR plasma source

The baseplate, shown in Figures 3.2 and 3.3, was designed to allow laser access to the plasma source region [27]. The plasma is created within a fused quartz chamber (Figure 3.3) 12.5 cm in diameter and 7 cm tall attached to the baseplate. The eight rare earth magnets are housed in a high permeability iron keeper which focuses the magnetic fields within the quartz chamber and eliminates magnetic fields in the downstream processing region. These magnets have a low Curie temperature and therefore need cooling to protect them from the relatively high temperature of the plasma. Water cooling is provided by that section of the baseplate which surrounds the magnet ring. The baseplate design keeps the function of the iron keeper and the water cooling intact while allowing laser access to the discharge region in front of the magnets. The baseplate also serves as the mechanism for the distribution of the working gas into the chamber. Eight pinholes are arranged around and below the inner side of the quartz chamber for gas access. Also, air cooling is available for the exterior of the quartz chamber if necessary.

3.1.3 The microwave and gas/vacuum systems

Microwave energy is supplied by a 2.45 GHz microwave power supply (Micro-Now 420B1). The experiments described here were performed with microwave power ranging from 150 Watts to 300 Watts. This power range refers to the power absorbed by the cavity which is found by subtracting the microwave power reflected by the cavity from the power incident to the cavity. The microwave circuit includes a three port circulator and dummy load to protect the power supply and a dual directional coupler for sampling both the reflected and incident power.

The 99.999% pure Argon and sulfur hexafluoride gases are fed into the baseplate through a mass flow controller (Tylan FC-280) with a range of flow from 0 to 50 sccm. The vacuum system includes a 2500 l/sec oil diffusion pump and a 33 m^3/sec mechanical pump both filled with a hydrocarbon-free oil to allow the use of reactive gases. To reduce backstreaming of oil, a freon-cooled baffle separates the processing chamber from the diffusion pump. This minimized the contaminates in the chamber at the expense of pumping speed.

A manual high-vacuum gate valve and a throttle valve separate the diffusion pump from the processing chamber. The throttle valve is used for fine control of the chamber pressure. The pressure is measured in the chamber with a capacitive manometer (MKS-390HA) down to about 1 x 10^{-5} Torr. Also, an ionization pressure gauge is located at the opening to the diffusion pump but the variation of the sensitivity of this instrument to non-nitrogen environments brings its accuracy into question when the experimental gases are present.

3.2 Resonant cavity microwave reactor

The diamond deposition microwave cavity plasma reactor is a resonant cavity microwave discharge operating in the TM_{013} mode (Figure 3.4) [80]. The reactor includes a 7 inch inside diameter microwave cavity which includes optical access ports at the sides. The experiments described in this work were performed with either a 2 or a 3 inch silicon wafer already coated with a diamond film in place on the substrate holder. A Cober Model S6F/4503 2.45 GHz microwave power supply was used to provide 1.0 - 5.0 kilowatts of microwave power.

The hydrogen discharge experiments were performed in the same reactor as shown in Figure 3.1 except the ECR magnets were removed. These experiments were performed at pressures of 100 - 500 mTorr. A Gerling Model GL119 2.45 Ghz microwave power sup-

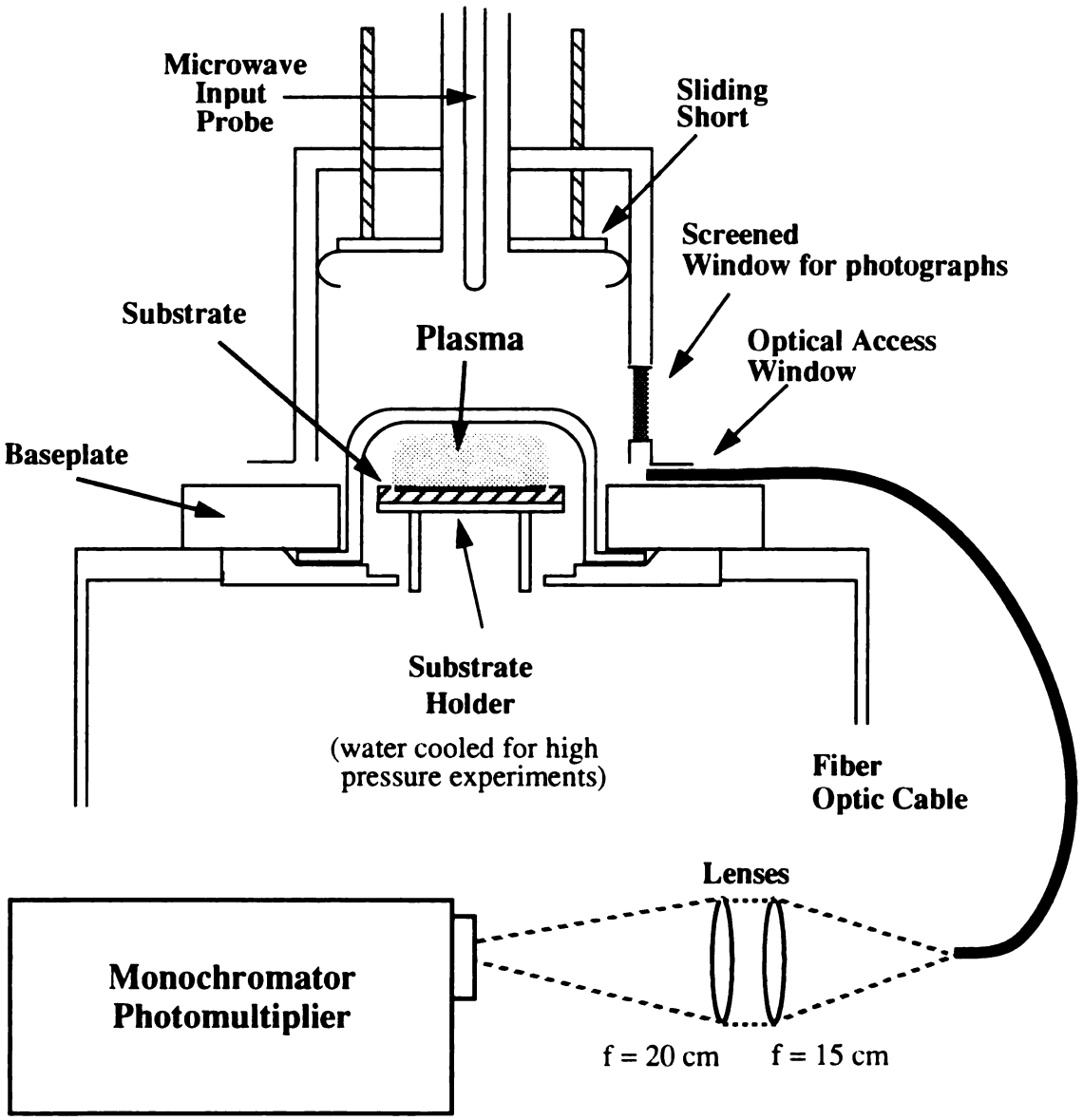

Figure 3.4: Diamond deposition microwave cavity plasma reactor [80].

ply was used to provide 150 - 300 Watts of microwave power to the cavity. The Tylan FC-280 mass flow controller regulates the 0 - 50 sccm hydrogen flow rate.

3.3 Statistical experimental design

Systematically quantifying and characterizing the reactors described above in terms of species temperature, energy, and concentration requires a well planned experimental design which maximizes the information gathered while minimizing the costs. In addition to using statistical experimental design principles a careful choice of the experimental parameter space is needed. This choice includes determining the specific values at which measurements are taken and the number of experimental factors (such as pressure) to be considered. For instance, based on information from deposition and etching experiments, pressure, microwave power and gas flow rate are the three factors chosen for study in the experiments described in Chapters 4, 5 and 6. The parameter space for each factor is described in the corresponding chapter. The specific values of each factor where measurements were made is based on the factorial design principles described below.

3.3.1 Introduction to statistical experimental design

Chapter 4 investigates the temperatures and plasma species concentration values found in the diamond deposition reactor through a series of experiments statistically designed. A full factorial experiment was performed consisting of two levels for each of three experimental variables. This constitutes a 2^3 factorial experiment, therefore eight experiments are used to span the chosen experimental parameter space. In addition, a center point and six star points were chosen to check for model linearity. Figure 5 shows the location of the data points for the parameter space described in Chapter 4. The experimental order was randomized and five repetitions of the center point were taken to provide a test of experimental repeatability, i.e. an estimate of experimental error [75].

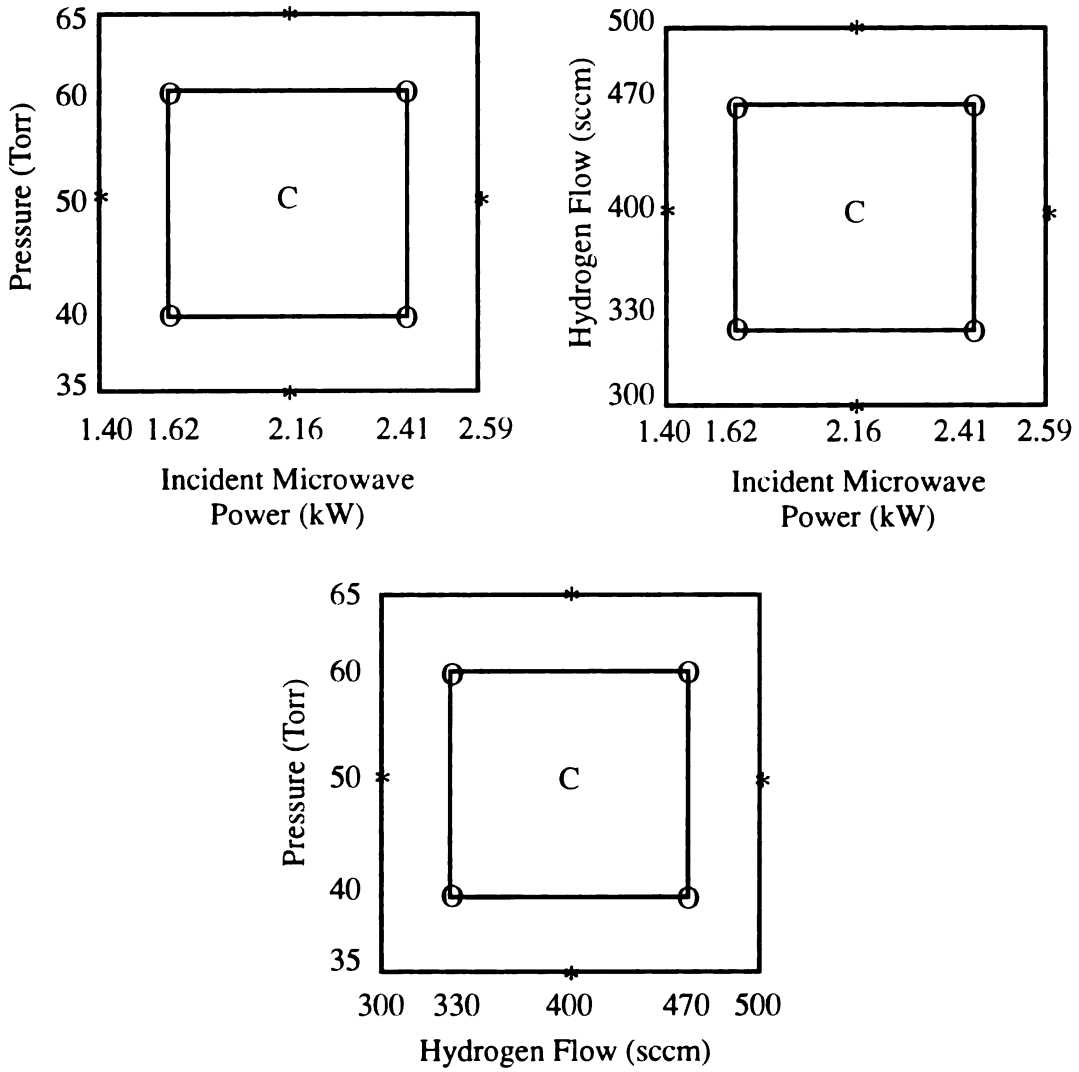

Figure 3.5: Schematic of a 2^3 factorial design with a center point and star points. The factor points are marked with open circles (O), the star points are marked with an asterisk (*) and C is the center point.

The three factors chosen in these experiments are pressure, gas flow rate, and microwave power. The parameters for each of the fifteen diamond deposition reactor experiments are shown in Table 3.1. To determine the functional relationship of the temperature and concentration data to each of the three factors a simple least squares fit was performed. For example, to test hydrogen translational temperature dependance on pressure, a fit was made to pressure of the temperature data at the center point of microwave power and hydrogen flow. Figure 3.6 shows the results of a linear fit of hydrogen translational temperature to incident microwave power. Quadratic least squares fits were also performed. The linear fit shown in Figure 3.6 is sufficient to describe the variation of hydrogen translational temperature to power, therefore hydrogen translational temperature is assumed to vary linearly with variations in power over this parameter space. As is explained in Chapter 4, if a better fit is obtained with the quadratic least squares algorithm, this fact is accounted for in the model building.

Table 3.1 Factorial design table.

Run #	Pressure (Torr)	Incident Power (kW)	Hydrogen Flow Rate (sccm)	Methane Flow (sccm) [1.5% H flow]	Run Type
1	50	2.16	400	6	Center
2	40	1.62	330	5	Factor
3	60	1.62	330	5	Factor
4	40	2.412	330	5	Factor
5	60	2.412	330	5	Factor
6	40	1.62	470	7	Factor
7	60	1.62	470	7	Factor
8	40	2.412	470	7	Factor
9	60	2.412	470	7	Factor
10	50	2.16	300	4.5	Star (Flow)
11	50	2.16	500	7.5	Star (Flow)
12	35	2.16	400	6	Star (Pressure)
13	65	2.16	400	6	Star (Pressure)
14	50	1.404	400	6	Star (Power)
15	50	2.592	400	6	Star (Power)

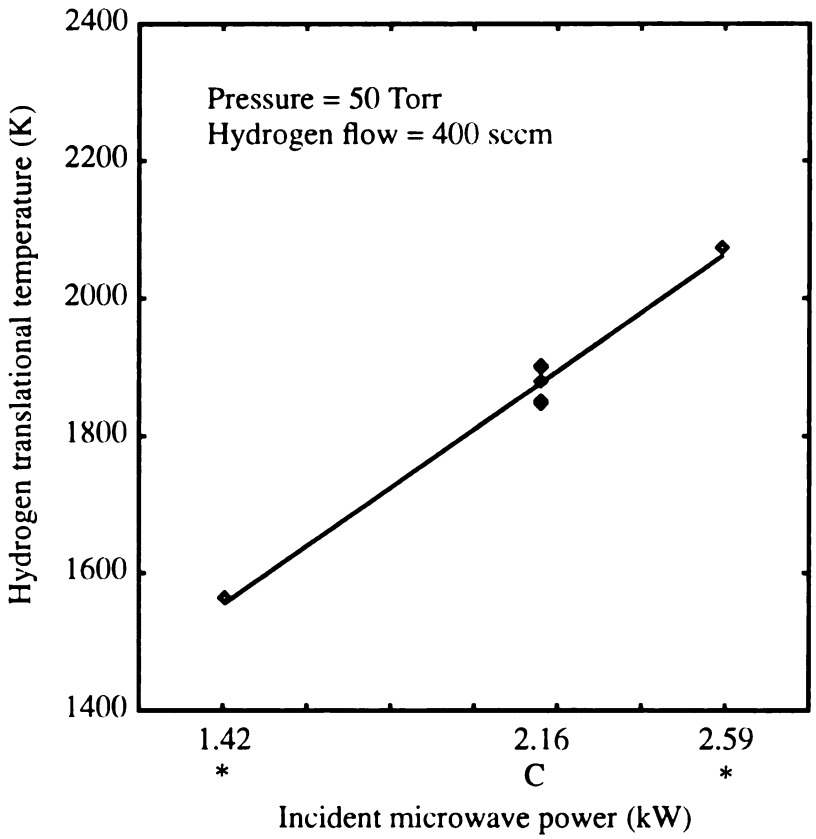

Figure 3.6: Linear least squares fit of hydrogen translational temperature to the center (C) and star (*) points of incident microwave power for the statistically designed diamond deposition reactor diagnostic experiments.

3.3.2 Analysis of variance

The data was analyzed using the commercially available statistics package SPSS for Windows 6.0 [74]. Analysis of variance (ANOVA) tables were generated using the two level factorial analysis data (runs numbered 2 through 9 in Table 3.1) to estimate the strength of the main effects and two-way interactions (also known as the first order interactions). Figure 3.7 is an example ANOVA table generated by SPSS examining the hydrogen translational temperature data from Chapter 4. The total (Total) sum of squares, appearing in the ANOVA tables, is the sum of the squares (SS) of the difference between the observed values and the mean value of all observations. The total mean square (MS) is the sum of squares divided by the corresponding degrees of freedom (DF). In other words, the variance is the mean value of the squared deviation between the observations and the sample mean.

To study the main (INCPOW, PRESSURE, HFLOW in Figure 3.7) and first order (INCPOW * PRESSURE, etc. in Figure 3.7) effects separately in factorial experiments, the analysis of variance is slightly more complicated. The sums of squares associated with each of the main effects (pressure, power, flow), each of the first order effects (pressure x power, pressure x flow, power x flow) and the second order effect (pressure x power x flow) are calculated in general as the sum of squares of the associated observed values corrected for the mean less any lower order sums of squares as described below. For example, let T_{ijk} be the temperature associated with the i^{th} power level, j^{th} pressure level and the k^{th} flow level. Let, SSPR, SSHF and SSIP equal the sums of squares of pressure, hydrogen flow and incident power respectively, then using the table in Figure 3.8a, which details the results of two-level experiments, the sums of squares are found as:

* * * * * * * * * * * * * * * * Analysis of Variance -- design 1 * * * * * * * * * *

Tests of Significance for TEMP using UNIQUE sums of squares

Source of Variation	SS	DF	MS	F	α
WITHIN+RESIDUAL	41760.50	1	41760.50		
INCPOW	156800.00	1	156800.00	3.75	.303
PRESSURE	229164.50	1	229164.50	5.49	.257
HFLOW	21218.00	1	21218.00	.51	.606
INCPOW * PRESSURE	14280.50	1	14280.50	.34	.663
HFLOW * INCPOW	10658.00	1	10658.00	.26	.702
HFLOW * PRESSURE	32512.50	1	32512.50	.78	.540
(Model)	464633.50	6	77438.92	1.85	.510
(Total)	506394.00	7	72342.00		

R-Squared = .918

Figure 3.7: ANOVA table generated using SPSS for Windows software for hydrogen translational temperature.

$$C = \frac{G^2}{abc} \tag{3.1}$$

$$SSIP = \frac{1}{ab}\left((IP_{1tot})^2 + (IP_{2tot})^2 \right) - C$$

$$SSPR = \frac{1}{bc}\left((PR_{1tot})^2 + (PR_{2tot})^2 \right) - C$$

$$SSHF = \frac{1}{ac}\left((HF_{1tot})^2 + (HF_{2tot})^2 \right) - C$$

$$IP_{1tot} = \sum_j \sum_k T_{1jk} \qquad IP_{2tot} = \sum_j \sum_k T_{2jk}$$

$$PR_{1tot} = \sum_i \sum_k T_{i1k} \qquad PR_{2tot} = \sum_i \sum_k T_{i2k}$$

$$HF_{1tot} = \sum_i \sum_j T_{ij1} \qquad HF_{2tot} = \sum_i \sum_j T_{ij2}$$

where C is the correction for the mean, a is the number of pressure levels, b is the number of flow levels and c is the number of power levels [76].

The sums of squares of the first order interactions are found by constructing tables of the interaction terms using the data in Figure 3.8b. The pressure by power first order interaction sum squares is calculated by the following equation:

$$SSIPPR = \frac{1}{c}\left(\left(\sum_k T_{11k} \right)^2 + \left(\sum_k T_{12k} \right)^2 + \left(\sum_k T_{21k} \right)^2 + \left(\sum_k T_{22k} \right)^2 \right) - SSIP - SSPR - C \tag{3.2}$$

A

Power	Pressure	Hydrogen Flow HF_1	HF_2	
IP_1	PR_1	T_{111}	T_{112}	$T_{111} + T_{112}$
	PR_2	T_{121}	T_{122}	$T_{121} + T_{122}$
		$T_{111} + T_{121}$	$T_{112} + T_{122}$	$IP_{1tot} =$ $T_{111} + T_{112} + T_{121} + T_{122}$
IP_2	PR_1	T_{211}	T_{212}	$T_{211} + T_{212}$
	PR_2	T_{221}	T_{222}	$T_{221} + T_{222}$
		$T_{211} + T_{221}$	$T_{212} + T_{222}$	$IP_{2tot} =$ $T_{211} + T_{212} + T_{221} + T_{222}$
		$HF_{1tot} =$ $T_{111} + T_{121} + T_{211} + T_{221}$	$HF_{2tot} =$ $T_{112} + T_{122} + T_{212} + T_{222}$	$G = IP_{1tot} + IP_{2tot}$ $= HF_{1tot} + HF_{2tot}$ $= PR_{1tot} + PR_{2tot}$
		$PR_{1tot} =$ $T_{111} + T_{112} + T_{211} + T_{212}$	$PR_{2tot} =$ $T_{121} + T_{122} + T_{221} + T_{222}$	

B

Power	Pressure PR_1	PR_2	
IP_1	$T_{111} + T_{112}$	$T_{121} + T_{122}$	IP_{1tot}
IP_2	$T_{211} + T_{212}$	$T_{221} + T_{222}$	IP_{2tot}
	PR_{1tot}	PR_{2tot}	G

C

Power	Hydrogen Flow HF_1	HF_2	
IP_1	$T_{111} + T_{121}$	$T_{112} + T_{122}$	IP_{1tot}
IP_2	$T_{211} + T_{221}$	$T_{212} + T_{222}$	IP_{2tot}
	HF_{1tot}	HF_{2tot}	G

D

Pressure	Hydrogen Flow HF_1	HF_2	
PR_1	$T_{111} + T_{211}$	$T_{112} + T_{212}$	PR_{1tot}
PR_2	$T_{121} + T_{221}$	$T_{122} + T_{222}$	PR_{2tot}
	HF_{1tot}	HF_{2tot}	G

Figure 3.8: Tables illustrating the construction of an analysis of variance. A: Totals for the main effects. B: Totals for the Pressure * Power interaction. C: Totals for the Flow * Power interaction. D: Totals for the Flow * Pressure interaction.

The pressure by flow and power by flow interactions would be calculated in a similar manner using the tables in Figures 3.8c and 3.8d. The pressure by power by flow second order interaction is found in a similar manner as:

$$SSIPPRHF = \left(\sum_i \sum_j \sum_k T_{ijk}^2 \right) - SSIP - SSPR - SSHF - SSIPPR - SSIPHF - SSPRHF - C \quad (3.3)$$

where SSIP, SSPR, SSHF are the main effects, SSIPPR, SSIPHF, SSPRHF are the two way interactions and C is the correction for the mean. A representative two level ANOVA table is shown in Figure 3.9 for hydrogen translational temperature [76]. As an example, the sums of squares for incident power and for pressure are found using Equation 3.1 as:

$$C = \frac{(14488)^2}{(2)(2)(2)} = 26{,}237{,}768.0$$

$$SSIP = \frac{1}{(2)(2)}((6684)^2 + (7804)^2) - 26{,}237{,}768.0 = 156{,}800.0$$

$$SSIP = \frac{1}{(2)(2)}((6567)^2 + (7921)^2) - 26{,}237{,}768.0 = 229{,}164.5$$

Then using Equation 3.2 and Figure 3.9B the pressure by power first order interaction can be calculated:

$$SSIPPR = \frac{1}{(2)}((2919)^2 + (3765)^2 + (3648)^2 + (4156)^2)$$
$$- 156{,}800.0 - 229{,}164.5 - 26{,}237{,}768.0 = 14{,}280.5$$

A

Power	Pressure	Hydrogen Flow 330	470	Sums
1.62	40	T_{111} = 1539	T_{112} = 1380	2919
	60	T_{121} = 1979	T_{122} = 1786	3765
Sums		3518	3166	IP_{1tot} = 6684
2.41	40	T_{211} = 1975	T_{212} = 1673	3648
	60	T_{221} = 1957	T_{222} = 2199	4156
Sums		3932	3872	IP_{2tot} = 7804
		HF_{1tot}=7450	HF_{2tot}=7038	G = 14488
		PR_{1tot} = 2919	+ 3648 =	6567
		PR_{2tot} = 3765	+ 4156 =	7921

B

Power	Pressure 40	60	Sums
1.62	2919	3765	6684
2.41	3648	4156	7804
Sums	6567	7921	14488

C

Power	Hydrogen Flow 330	470	Sums
1.62	3518	3166	6684
2.41	3932	3872	7804
Sums	7450	7038	14488

D

Pressure	Hydrogen Flow 330	470	Sums
40	3514	3053	6567
60	3936	3985	7921
Sums	7450	7038	14488

Figure 3.9: Hydrogen translational temperature example of tables illustrating the construction of an analysis of variance. A: Totals for the main effects. B: Totals for the Pressure * Power interaction. C: Totals for the Flow * Power interaction. D: Totals for the Flow * Pressure interaction.

Comparing to Figure 3.7, these are the values listed in the ANOVA for sums of squares INCPOW, PRESSURE and INCPOW * PRESSURE.

Each of the effects included in the ANOVA is assumed significant if the sum of squares is much larger than some error. The error term can be found from two separate effects. Error can be found from repeated experiments, known as WITHIN error; or the error can be the higher order, relatively insignificant terms, known as the RESIDUAL error; or error can be the sum of these two (WITHIN + RESIDUAL in Figure 3.7). Since the experiments in the factorial design portion (two level) of the data set were performed with only one repetition, i.e. a single block of data, there is no within error available for the two level full-factorial ANOVA (WITHIN = 0). For all of the analyses studied, the second order effects were small compared with the main effects; therefore, the three-way interaction serves as the initial error estimate in the analysis of variance.

If certain other effects were shown to be non-significant these were included with the error. For example, the first order effects may turn out to be insignificant when compared to the error (the error is the second order effect). The sum of squares of these effects are then added to the error term. Pooling of non-significant effects in this manner, increases the number of degrees of freedom associated with the error as well as increases the sum of squares. The mean square, therefore, will not increase appreciably unless the effect is actually significant, i.e. it has large sum of squares [77].

3.3.3 Significance test

The significance of each of the factors and interactions included in the ANOVA results is quantified using an F-test. The one particular assumption implicit in using an F-test to make inferences about the data is the residuals, the difference between observation and average, for the entire population are independent and normally distributed. Based on this assumption the sum of the squares of the residuals and the variance of this distribution

(σ_1^2) has a chi-square distribution (χ^2). A sample randomly drawn from this population has sample variance s_1^2 with ν_1 degrees of freedom. The ratio of the population variance to the sample variance (σ_1^2/s_1^2) is distributed as χ^2/ν_1. Another sample, s_2^2, with ν_2 degrees of freedom has a variance ratio distributed in an identical manner. The ratio of these two distributions is said to have an F distribution with ν_1 and ν_2 degrees of freedom. Thus the ratio of the sample variances is also distributed according to the same F distribution.

The F distribution can be used to check hypotheses concerning two variances as follows. The ratio of the mean square for a particular effect, say pressure, to the mean square error will be distributed according to the $F(\nu_p, \nu_e)$ distribution, where ν_p is the number of degrees of freedom associated with the pressure effect and ν_e is the number of degrees of freedom associated with the error. First, hypothesize the variances (mean squares) of these two distributions are equal, the null hypothesis, then check the calculated ratio with the $F(\nu_p, \nu_e)$ distribution. If the area under the $F(\nu_p, \nu_e)$ distribution above the calculated ratio is small then the null hypothesis is discredited and it is said a significant difference exists between the mean squares. As the value of the area approaches 1, the null hypothesis is strengthened. In this case, the pressure effect could not be separated from the effect of error. These calculations are handled easily with SPSS and other statistics packages. The area under the distribution mentioned above is known as the significance of F or α [75].

3.3.4 Model building

A model was determined from a general nonlinear least squares regression. The factors included in the model were chosen based on the ANOVA and the F-tests. The regression analysis was performed using both backward elimination and forward model building techniques. In the backward elimination regression, all suggested effects were included in the initial model. If the significance of the F-test (α) for a particular effect is

above a certain value (P_{out}) then the effect is removed and the regression is repeated on the remaining effects. In the forward model building technique an effect is included only if the α associated with the effect is below a certain value (P_{in}). Both methods resulted in the same final regression equation for all the models presented here. The results are given both in equation and graphical form.

As a measure of the goodness-of-fit of the regression model to the observed data, the coefficient of determination (R^2) is calculated. The coefficient of determination is defined as the proportion of the variability in the fit accounted for by the independent parameters included in the model. The coefficient is calculated as the ratio of the sum of squares of the observed values less the sum of squares of the residuals to the sum of squares of the observed values:

$$R^2 = \frac{S_y - SSR}{S_y} \tag{3.4}$$

where: $$S_y = \sum y_i^2 - \frac{(\sum y)^2}{n}$$

$$SSR = \sum (y_i - y_{ip})^2$$

S_y is the sum of squares of the observed values, as in the ANOVA; *SSR* is the sum of squares of the residuals; y_i are the observations, y_{ip} is the predicted value of y, and n is the number of observations. All sums are over the number of observations [77]. So an R^2 value of 0.90 would indicate the model accurately predicts 90% of the observations. Considering the difficulties in data analysis for the experiments discussed here, values of 70% or better are considered adequate fits.

Also given with each model is the standard deviation of the model from the observed data. The standard deviation is the square root of the error variance. The error variance is the sums of squares of the residuals divided by the degrees of freedom associ-

ated with the residuals. The residual degrees of freedom is the difference between the number of observations (n) and the number of parameters estimated in the least squares fit (p). Therefore, the standard deviation (s) is given by:

$$s = \sqrt{\frac{SSR}{n - p}} \tag{3.5}$$

The five repeated center point experiments are also used as a measure of error. This error is associated with experimental factors affecting the results but not accounted for in the randomization of the experimental order. Data analysis uncertainties are the largest contributor to this error. The error (SSE) was calculated as the sum of squares of the replicated runs as:

$$SSE = \sum y^2 - \frac{(\sum y)^2}{n} \tag{3.6}$$

where the sums are over the data (y) of the replicated runs only and n is the number of replications ($n = 5$ for all the statistically designed experiments).

The sum of squares of the residuals is a measure of the difference of the model to the observed data. This difference is due to experimental error and due to the lack of fit of the model to the observations. The portion due to experimental error is given by the error sum of squares (SSE). The difference between the residual sum of squares and the error sum of squares is the sum of squares due to lack of fit--the lack of fit sum squares (SSL). The significance of SSL can be found using an F-test on the mean square of lack of fit and the mean square of the error. Examples of these calculations are included with the models in Chapter 4.

Chapter 4

Diamond Deposition Discharge Diagnostics

4.0 Introduction to diamond deposition discharges

Chemical vapor deposition (CVD) of diamond films through the use of a microwave cavity plasma reactor such as the one studied here involves a number of chemical processes. Atomic hydrogen and methyl radicals of some form seem to be important species present in the CVD of diamond [78]. Understanding the kinetic properties of these or related species as well as the properties of the reactor as a whole is necessary to develop models of their behavior which is an important step toward designing improved reactors. Specifically, the various temperatures, energies and the concentration of atomic hydrogen, the temperature and energy of the carbon molecule and the temperature of the processing surface are important parameters which aid in modeling, predicting and understanding plasma behavior.

4.1 Temperature and energy

Energy imparted on a system of particles such as those found in plasma discharges can be distributed among the particles into either kinetic or internal energy. Kinetic energy is the energy of motion or translational energy while internal energy can reside in the particle's electronic energy for atoms and ions or split into electronic, vibrational and rotational components in the case of molecules. The interpretation of temperature as a measure of a particle's mean kinetic energy arises from an assumption the velocities of the particles follow a Maxwellian distribution. Additionally, if the assumption is made the distribution of energy in each of the internal degrees of freedom follow Maxwell-Boltzmann

statistics then a statistical temperature can be defined to describe this internal energy distribution [79].

The internal degrees of freedom are partially independent of each other and therefore a temperature can be defined for each of their energy distributions. So for molecules an electronic temperature, a vibrational temperature and a rotational temperature can be defined. Optical emission spectroscopy can be used to measure the internal temperature of a particular system of particles. When a system of particles is in complete thermodynamic equilibrium, the kinetic temperature and all the spectroscopic temperatures will be equal. An atom considered to be in thermodynamic equilibrium will, therefore, have an electronic temperature equal to its kinetic or translational temperature. Molecules in complete thermodynamic equilibrium will have equal electronic, vibrational and rotational temperatures.

Microwave discharges are not necessarily in complete thermodynamic equilibrium since the microwave energy continuously perturbs the equilibrium. This only precludes the use of the concept of temperature if the velocity distribution is radically different from Maxwellian. By studying the energy of various internal degrees of freedom, the extent to which a certain discharge is in equilibrium, either locally or as a whole, can be determined.

4.2 Experimental method

The measurements detailed above were performed in the diamond deposition microwave cavity plasma reactor (MCPR) operating in the TM_{013} mode (Figure 3.4) as described in Chapter 3 [80]. The optical emission from the discharge was collected using a fiber cable with a numerical aperture of 0.3. The cable was placed in the optical access port at the base of the microwave cavity as shown in Figure 3.4. The collection volume was approximately 50 cm^3 directly above the 3 inch wafer and substrate. Figure 4.1 shows

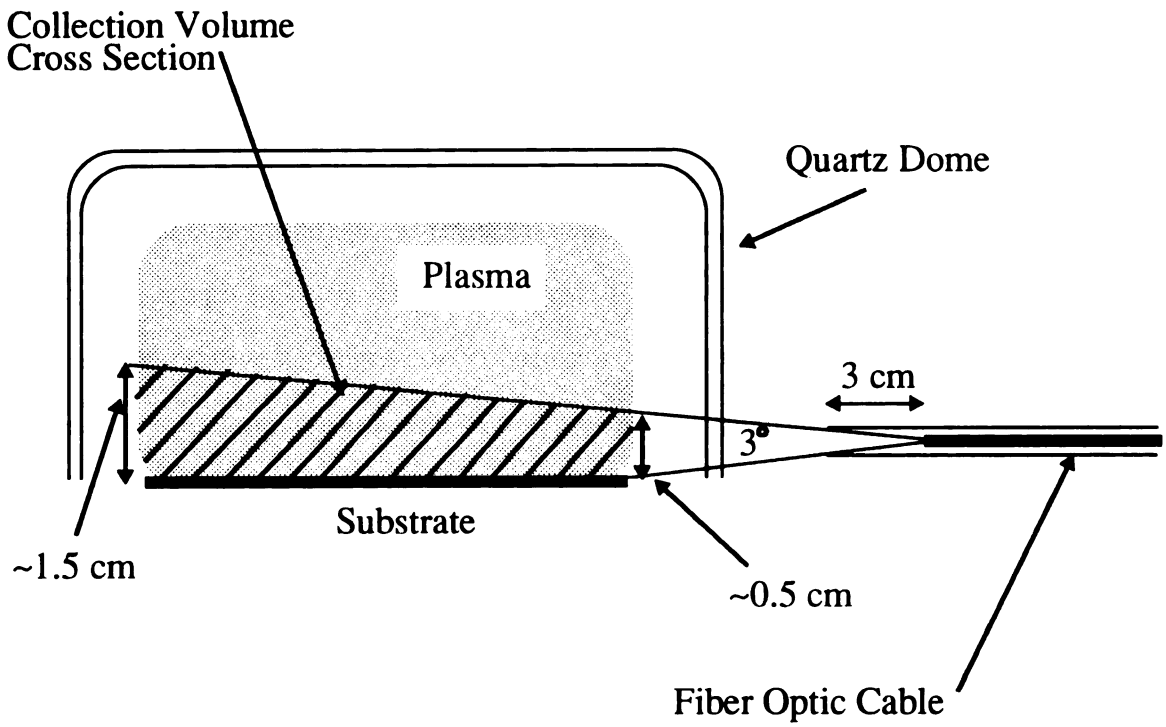

Figure 4.1: Light collection volume for the diamond deposition microwave plasma cavity reactor.

the detail of the collection volume. The fiber cable was used to bring the discharge emission to the monochromator and photomultiplier. Two lenses were used at the entrance to the monochromator to match the f-number of both the fiber cable and the monochromator (Figure 3.4). The slits on the monochromator were 20 μm wide by 1 cm high to allow in the most amount of light with the best spectral resolution. The optical emission spectroscopy experiments were carried out using a SPEX 1 m monochromator and a Thorn-EMI cooled photomultiplier tube.

The details of the optical emission experiments performed on the diamond deposition reactor are given below. Hydrogen translational temperature, hydrogen electronic temperature, relative hydrogen concentration (actinometry), C_2 rotational temperature, substrate temperature, plasma volume and plasma density measurement techniques are described in the next seven sections.

4.2.1 Hydrogen translational temperature

The translational temperature of hydrogen was determined by examining the Doppler-shifted optical emission from the hydrogen atomic Balmer-α transition at 6562.8 Å. The full width at half maximum (FWHM) of the atomic hydrogen emission in the diamond deposition reactor is broadened primarily by the kinetic (translational) motion of the atom (Doppler broadening), the interaction of the atom with neighboring charged particles (Stark broadening), the fine structure splitting, and the finite spectral response of the detection equipment (instrument broadening).

The motion of hydrogen atoms will cause the wavelength of light emitted through an electronic transition to be shifted by means of the Doppler effect. Assuming the velocity of the system of atoms can be described using Maxwellian statistics, the intensity of the emitted radiation at a particular wavelength is a function of translational energy (kT).

Thus, a purely Doppler broadened line has a Gaussian shape. The FWHM of this Gaussian distribution can be measured and the translational temperature determined from:

$$T = \frac{mc^2}{2k(ln2)}\left(\frac{\Delta\lambda_D}{\lambda_o}\right)^2 \quad eV \tag{4.1}$$

$\Delta\lambda_D$ is the FWHM of the Doppler broadened line, λ_0 is the wavelength of the unbroadened line, m is the mass of the emitting species, c is the speed of light, and k is Boltzmann's constant [81].

The hydrogen emission lines exhibit a fine structure which arises from a splitting due to the electron spins. This splitting cannot be resolved by the monochromator utilized here so must be accounted for as an additional 'broadening' mechanism.

Pressure broadening is a term used to describe a number of effects which arise from the interaction of the radiating system with surrounding particles. One particular type of pressure broadening, Stark broadening, may be important in these discharges. To determine the importance of Stark broadening on the H_α emission, the density of charged species within the plasma must be estimated.

Purely Stark broadened lines of the hydrogen Balmer series have been computed by Griem [82] and reported by Blau, et al. [83]. Griem has determined the width of the Stark broadened Balmer lines as a function of plasma electron density at various electron temperatures. For an electron temperature of 5000 K the plasma density is given by:

$$N = [(3.99 \times 10^8)(\Delta\lambda_s/\alpha)]^{3/2} \; cm^{-3} \tag{4.2}$$

where $\Delta\lambda_s$ is the FWHM of the purely Stark broadened line in Angstroms and α, a coefficient for the various Balmer lines, is given in Table 4.1, along with the useful density range.

The electron density in the diamond deposition plasma is deduced using an iterative approach by first assuming a plasma density, determining the Stark broadened linewidth of the hydrogen line and deducing the Doppler broadened width of an experimental H_α line. The temperature and plasma density values are then used to calculate the

TABLE 4.1. Coefficient α for electron density estimates, the minimum detectable density and the fine structure splitting for various hydrogen Balmer lines.

	α	Density	$\Delta\lambda_{FS}$
H_α 656.2 nm	0.00969	$\sim 10^{15}$ cm^{-3}	0.140 Å
H_β 486.1 nm	0.0762	$\sim 10^{14}$ cm^{-3}	0.077 Å
H_γ 434.0 nm	0.0442	$\sim 10^{14}$ cm^{-3}	0.064 Å
H_δ 410.1 nm	0.149	$\sim 10^{13}$ cm^{-3}	0.057 Å

expected H_β width. By comparing the H_β calculations with the H_β experimental width an improved plasma density estimate is made. The iterative calculations are continued until the density chosen gives consistent linewidths for both H_α and H_β [82].

From these measurements the plasma density was determined to be 1.8×10^{13} cm^{-3} at 60 Torr with1.85 kWatts and 400 sccm H_2 and 7 sccm CH_4. At this density the Stark broadening is negligible for the H_α emission.

The finite spectral resolution of the detection equipment has the effect of broadening the observed line. Instrument broadening effects are known to be Lorentzian in shape [82]. Thus, the emission line with both Gaussian (Doppler, Fine Structure) and Lorentzian (Instrument, Stark) components will have a shape matching neither of these but a combination of the two. This combination has been termed a Voigt profile.

To extract the Gaussian component of lines with a Voigt profile, a fit was performed on each observed emission line. Given three parameters, height, Gaussian width

and Lorentzian width, a Voigt profile can be constructed following the procedure of Armstrong [85]. The basic program used for the fit is included in the Appendix. A typical Voigt profile fit to the hydrogen Balmer-α emission line is shown in Figure 4.2. By varying the three parameters the constructed profile can be fit to the observed profile. The Lorentzian width is assumed to be purely the instrument broadening for the experimental conditions studied here using the H_α emission line.

The instrument broadening for these conditions has a FWHM of 0.15 Å. This parameter was estimated by measuring the linewidth of an argon neutral line at 750 nm in a low pressure discharge using Fabry-Perot interferometry. Since the only significant broadening at this low pressure was Doppler broadening, the additional observed width in the low pressure argon neutral emission was assumed to be purely instrumental in origin.

Using the Lorentzian width above, the height of the line fitted to the observed emission, its Gaussian width, and the peak wavelength were varied to minimize the error between the constructed profile and the observed profile. The error was determined by summing the square of the difference between the observed intensity and the calculated intensity at each wavelength of the emission line. The best fit therefore also provided the best estimate of that portion of the emission line broadened by the atoms' translational motion (Doppler broadening) and by fine structure splitting.

At this point the fine structure splitting must be taken into account. Freund, et al. [86] have shown fine structure splitting is a Gaussian shaped effect and therefore can be deconvolved from the Gaussian shaped observed line. A purely Gaussian shaped Doppler broadened line remains:

$$\Delta\lambda_D = \sqrt{(\Delta\lambda_G)^2 - (\Delta\lambda_{FS})^2} \tag{4.3}$$

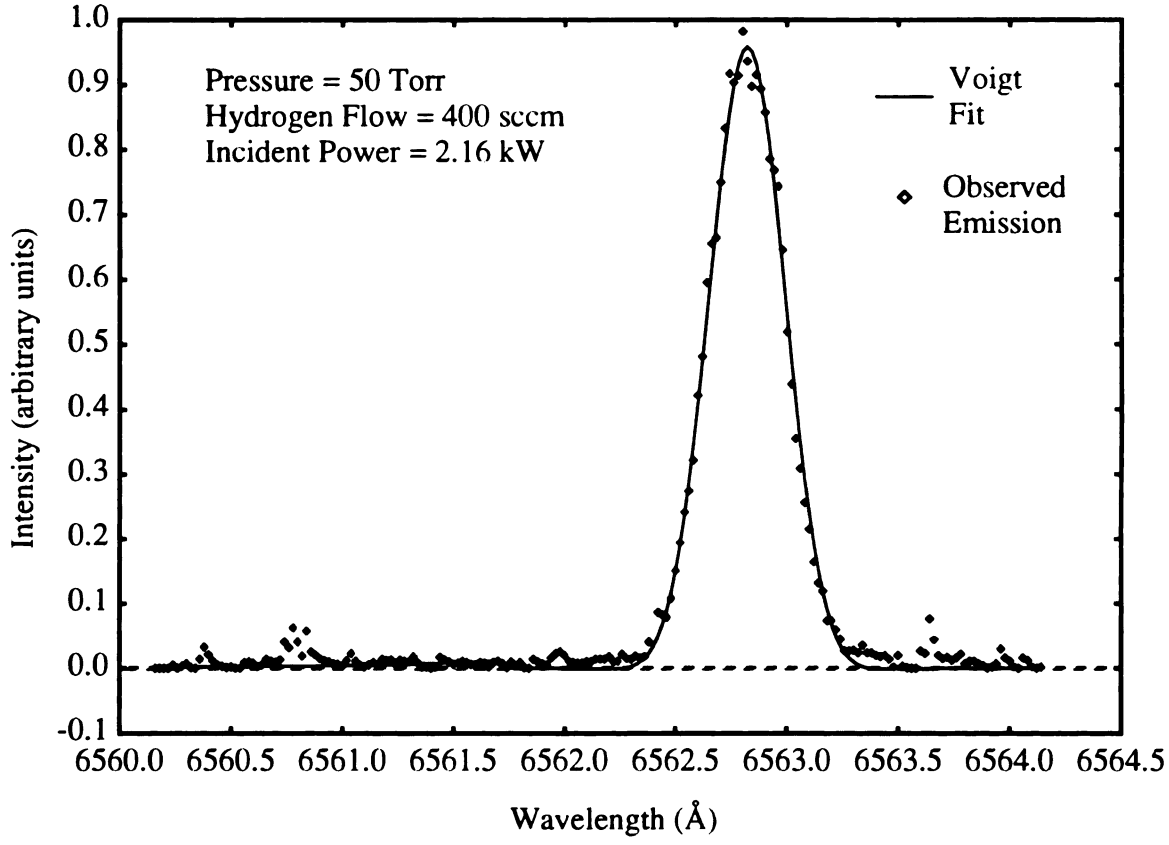

Figure 4.2: Typical Voigt profile.

where $\Delta\lambda_G$ is the FWHM of the Gaussian portion of the observed line, $\Delta\lambda_{FS}$ is the FWHM of the fine structure splitting (listed in Table 4.1) and $\Delta\lambda_D$ is the FWHM of the deconvolved Doppler broadened lineshape.

4.2.2 Hydrogen electronic temperature

The electronic temperature of the hydrogen atom was determined by using the two-line radiance ratio method [79]. To facilitate discussion of this method, a description of a single electronic transition in an atom is in order. At equilibrium, the two-line radiance ratio method assumes the populations of the different allowed energy levels in an atom are given by a Maxwell-Boltzmann distribution. Therefore the integrated intensity of an electronic transition from state n to state m is given by the following equation:

$$N_{nm} = \frac{hc}{4\pi} l\rho \frac{g_n}{Q} \frac{A_{nm}}{\lambda_{nm}} e^{-\frac{E_n}{kT}} \tag{4.4}$$

where E_n is the energy of the upper level, A_{nm} is Einstein's coefficient of spontaneous emission, λ_{nm} is the wavelength of the transition, g_n is the statistical weight of the upper level, Q is the partition function, ρ is the number density of atoms, l is the path length of light collection, T is the temperature associated with the transition, h is Plank's constant, c is the speed of light and k is Boltzmann's constant.

If all of the factors in equation 4.4 were known except the temperature, simply by integrating the intensity of a single transition the temperature could be found by solving for T. Unfortunately, not all of the factors are easily attained. This problem is taken into account by using two transitions in the same atom. The ratio of the integrated intensity for these two lines would eliminate the need to determine certain parameters such as l and ρ.

The ratio between two lines, one with upper level n, lower level m and the other with upper level o and lower level p, can then be solved for temperature as follows:

$$ln\frac{N_{nm}}{N_{op}} = ln\left(\frac{g_n A_{nm}\lambda_{op}}{g_o A_{op}\lambda_{nm}}\right) - \frac{\left(E_n - E_o\right)}{kT} \tag{4.5}$$

For the hydrogen atom the two transitions used to determine electronic temperature were the Balmer α and β transitions. The Balmer α transition (n=3, m=2) is characterized by λ_{32} = 6562.8 Å, g_3 = 18 and A_{32} = 4.41 x 10^8 sec^{-1}. For the Balmer β transition (o=4, p=2), λ_{42} is 4861.3 Å, g_4=32 and A_{42} = 8.42 x 10^8 sec^{-1} [87].

Since this method relies on an accurate measure of the integrated intensity of the two emission lines, proper calibration of the detection equipment is necessary. The response of the spectrometer and photomultiplier across the spectrum was calibrated using a quartz-halogen tungsten-filament standard of spectral irradiance (see Appendix B). The standard has a known intensity at both 486 nm and at 656 nm. The calibration was accomplished as follows. A correction factor (C) was calculated for each of the two lines by taking the ratio of the true spectral irradiance (I_{lamp}) of the standard to the measured spectral irradiance (I_{meas}) of the standard at a particular wavelength:

$$C_\lambda = \frac{I_{lamp}(\lambda)}{I_{meas}(\lambda)} \tag{4.6}$$

The corrected intensity, $I(\lambda)$, of the emission of both lines was then found by multiplying the measured intensity by the appropriate correction factor:

$$I(\lambda) = C_\lambda I^\circ(\lambda) \tag{4.7}$$

where I^0 (λ) is the uncorrected measured intensity at wavelength λ. The integrated intensity, N_{nm} is then found by integrating the corrected intensity across the emission line:

$$N_{nm} = \int I(\lambda)\, d\lambda \tag{4.8}$$

4.2.3 Relative atomic hydrogen concentration

As a measure of atomic hydrogen concentration actinometry is used. Actinometry is a technique which compares the concentration of the species under study to a known constant quantity of another species, the actinometer [21]. Since the concentration of the study species is known only in regard to the fixed concentration of the actinometer this is only a measure of relative concentration.

The intensity (I_x) of any particular emission line is proportional to the number of photons emitted per second at that particular wavelength. If there is only one deexcitation path then the photon emission rate will equal the frequency (ν_{ex}) at which the species is excited. The excitation frequency is proportional to the number density of the species (N_{ex}) multiplied by the rate of excitation. In turn, the rate of excitation is proportional to the cross section (σ_{ex}) of collisions between the exciting particle and the excited species and is also proportional to the velocity (v) of the exciting particle. Therefore the intensity of the species is

$$I_x \propto \nu_{ex} = N_{ex}\langle v\sigma_{ex}\rangle = N_x \int_{E_{ex}}^{\infty} v\sigma_{ex} f(E)\, dE \tag{4.9}$$

This relationship is true for both the species under study and the actinometer. Assuming the species are excited by electrons, then $f(E)$ is the distribution of electron energies. This distribution will be the same for all species. If the actinometer is chosen so it has an excitation threshold energy (E_{ea}) and a collision cross section (σ_{ea}) close to those

of the species under study (E_{ex},σ_{ex}) then the ratio of the two intensities (I_x/I_a) will be proportional to the density of species x:

$$\frac{I_x}{I_a} = \frac{N_x \int_{E_{ex}}^{\infty} v\sigma_{ex} f(E)\, dE}{N_a \int_{E_{ea}}^{\infty} v\sigma_{ea} f(E)\, dE} \cong \frac{N_x}{N_a} \propto N_x \qquad (4.10)$$

Successful, meaningful application of this technique requires the proper choice of the actinometer. Noble gases provide excellent choices for the actinometers since N_a will not be depleted by dissociation. To study the relative concentration of hydrogen in the diamond deposition reactor, a small amount of argon (10 sccm) was added to the hydrogen/methane discharge. The intensities of the hydrogen Balmer-β at 4861.2 Å and the argon neutral emission at 7503.9 Å were measured. Following the same technique as in Section 4.2.2 the intensities of the two lines were calibrated for the response of the monochromator/photomultiplier at the two wavelengths.

4.2.4 Rotational temperature of the C_2 molecule

At equilibrium the populations of the different energy levels in the various internal degrees of freedom in a molecule are given by a Maxwell-Boltzmann distribution. One of these degrees of freedom in diatomic molecules is the rotational energy. The rotational temperature of a system of these molecules can be determined by spectroscopically measuring the populations of a number of rotational states and fitting the data to a Maxwell-Boltzmann distribution to determine the temperature [79]. The intensity of an emission line in a electronic-vibrational-rotational transition in a diatomic molecule is given by:

$$I = C(J' + J'' + 1)\, exp(-B'J'(J''+1)(hc/kT)) \qquad (4.11)$$

where I is the intensity of a electronic-vibrational-rotational transition in a diatomic molecule, B' is the rotational constant for the upper state of the transition, J' and J'' are the rotational quantum numbers of the upper and lower states respectively, h is Planck's constant, k is Boltzmann's constant, c is the speed of light and C is a constant which incorporates the transition probability and the wavenumber of the transition [79].

Rotational constants for some of the vibrational states in the C_2 Swan band are given in Table 4.2 [88]. The temperature for the C_2 molecule is found by measuring the intensity of a number of rotational lines in a particular vibrational transition and then plotting:

$$ln\left(\frac{I}{J'+J''+1}\right) \qquad vs. \qquad -B'J'(J''+1)\frac{hc}{k} \tag{4.12}$$

The slope of the line will be the reciprocal of the rotational temperature. If the experimental points plotted according to Equation 4.12 lie on a straight line then the assumption of a Maxwell-Boltzmann distribution is a valid one. A typical C_2 spectra is shown in Figure 4.3 for the emission from a 60 Torr, 1.62 kW, 470 sccm H_2, 7 sccm CH_4 discharge. Figure 4.4 shows the plot of the straight line fit for these same conditions indicating the distribution is nearly Boltzmann.

TABLE 4.2. Rotational constants (B' and B") for various upper (v') and lower (v") vibrational states of the C_2 Swam system ($A^3\Pi_g$ - $X^3\Pi_u$) [88].

v'	B' (cm^{-1})	v"	B" (cm^{-1})
0	1.74557	0	1.6237
1	1.72535	1	1.60715
2	1.70430	2	1.59043
3	1.68145	3	1.57362

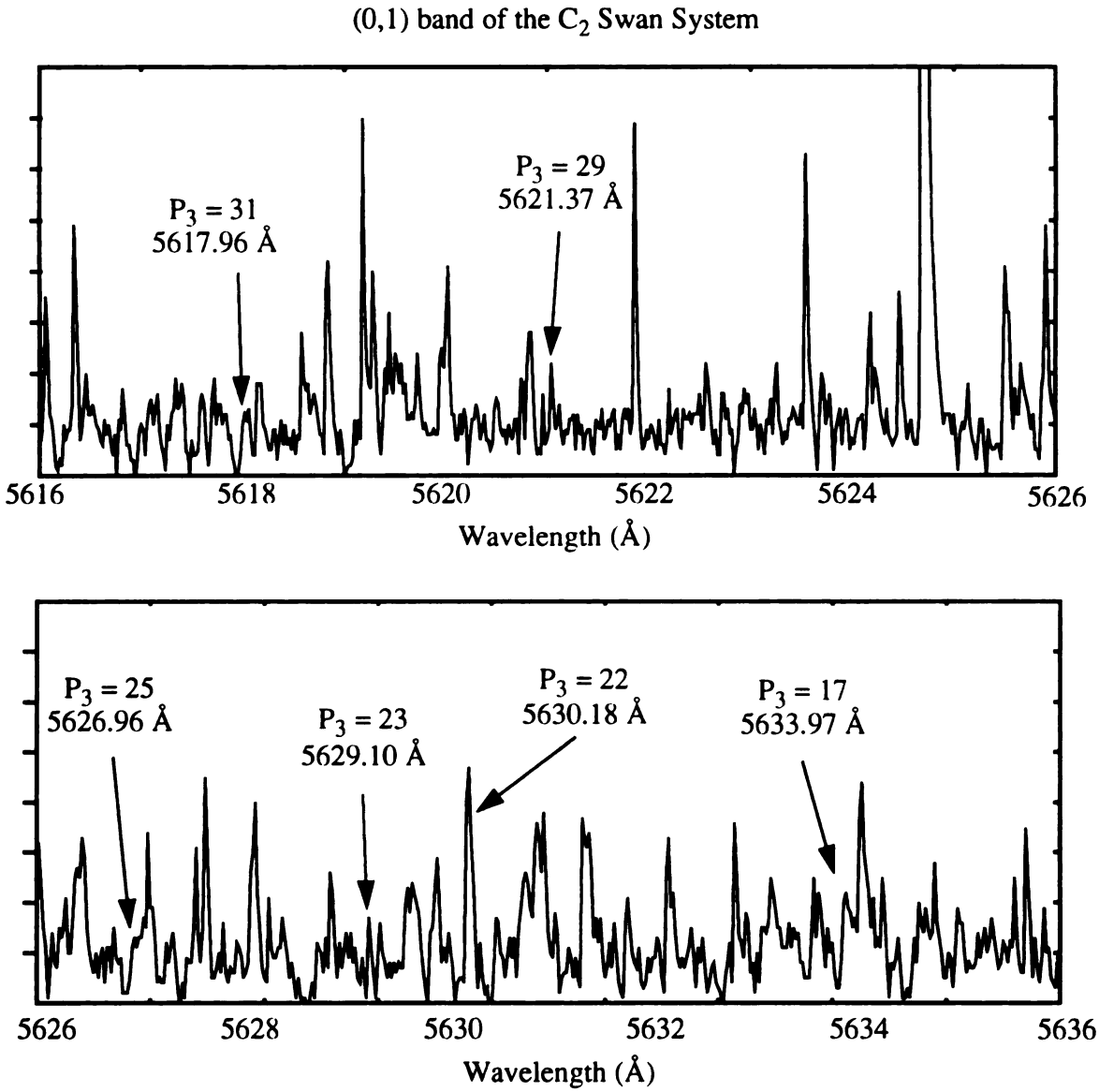

Figure 4.3: Typical C_2 spectra: Incident microwave power = 1.62 kW; Pressure = 60 Torr; Hydrogen flow = 470 sccm.

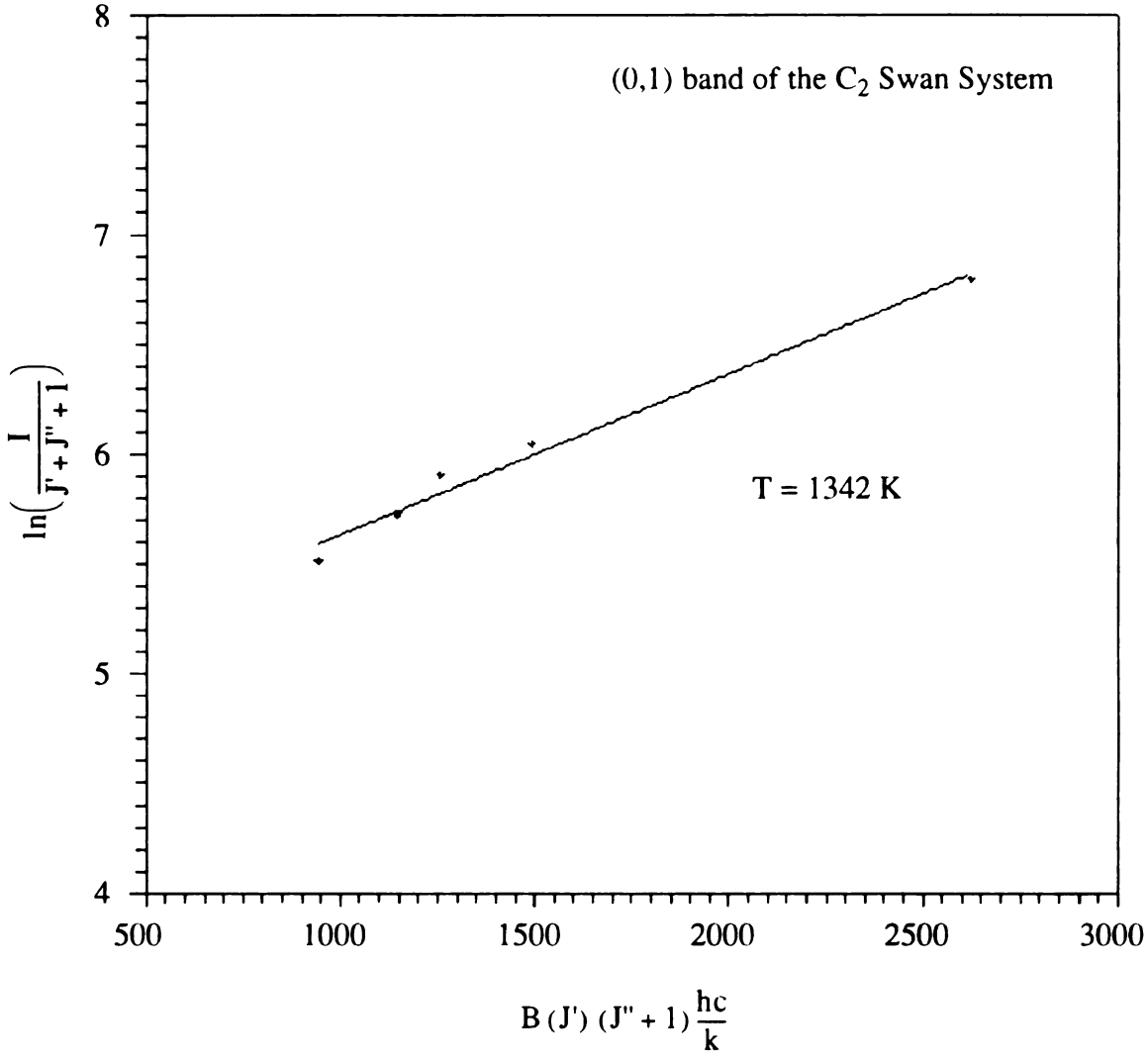

Figure 4.4: Least squares fit to the J" = 20, 22, 23, 25, 33 lines of the P-branch of the 0,1 band of the C_2 Swan system. Incident power = 1.62 kW, pressure = 60 Torr, and hydrogen flow = 470 sccm.

4.2.5 Substrate temperature

The substrate temperature was measured using an Ircon Ultimax model infrared emission pyrometer. The pyrometer was focused on the center of the wafer initially then, for each experiment, the maximum temperature near the center region of the wafer was found. This is the value reported as substrate temperature for the diamond deposition experiments.

4.2.6 Plasma volume

The plasma volume was determined by photographing the plasma discharge. The photographs were taken through a blue-green transmitting optical filter. Each photograph was taken so both the plasma and the substrate appeared in the pictures. The plasma volume was determined by measuring the plasma region size on the photograph. The substrate in each photograph served as the calibration size. The assumed shape of the plasma is shown in Figure 4.5. The power density of the plasma was then determined by taking the ratio of the absorbed microwave power and the plasma volume.

4.2.7 Power density

The power density in Watts per cubic centimeter (W/cm^3) was estimated using the plasma volume estimates described in Section 4.2.6 and a measurement of absorbed microwave power. All of the power absorbed by the cavity was assumed to go into creating the plasma.

4.3 Statistical Experimental Design

The experimental results for translational temperature, electronic temperature, relative hydrogen concentration, substrate temperature, rotational temperature, plasma volume and plasma density are presented using the statistical procedures described above. The results include determination of significant effects and model building. Table 4.3 and

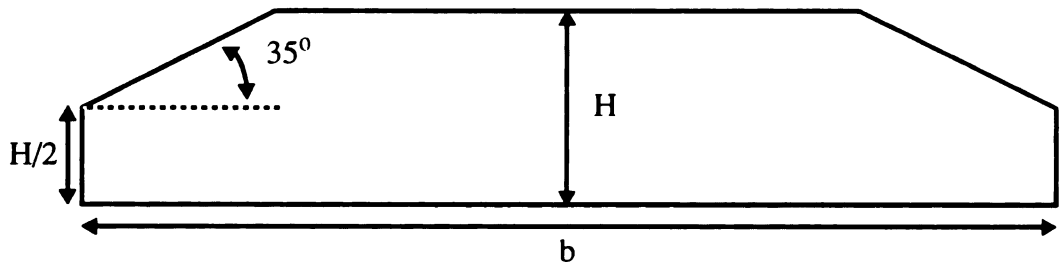

Figure 4.5: Assumed plasma shape used for plasma volume measurements.

Table 4.6 list all nineteen experiments included in the 2^3 factorial design over a pressure range of 35 - 65 Torr, a power range of 1.4 - 2.6 kW and a hydrogen flow range from 300 - 500 sccm. As detailed in Chapter 3 and in addition to the eight factorial experiments, a center point was included as well as six star points. The experiment at the center point (pressure = 50 Torr, incident microwave power = 2.16 kW and hydrogen flow = 400 sccm) was repeated five times.

4.3.1 Translational temperature results

Using Equation 1 and the FWHM of the Doppler broadened line, the translational temperature of atomic hydrogen was found for each of the experiments. An analysis of variance of the translational temperature data revealed the statistically relevant experimental parameters. The observed F-test values for the first order interactions between all three experimental factors were non-significant at a significance level (α) of 0.25 and thus were pooled with the second order interaction as an experimental error term. Similarly, the hydrogen flow effect was non-significant at an α of 0.25 even when compared to the new pooled error term. Consequently, this factor was pooled with the error to create an error term with five degrees of freedom against which the microwave power and pressure effects were compared. The mean square, F-test value and significance level for these two factors are listed in Table 4.4. Each of these main effects was significant at or below an α of 0.051.

The analysis of variance was performed using incident microwave power because the incident power, pressure and hydrogen flow are independent of one another. Another useful parameter to consider is absorbed microwave power. Absorbed power is defined as the difference between the microwave power incident on the resonant cavity and the power reflected from the cavity. For a given amount of incident power the amount of reflected power varies as a function of the short height and input probe depth into the cavity and as a function of plasma parameters. For all of these experiments the cavity short

Table 4.3 Statistically designed experiments for the diamond deposition reactor (Part I).

Run # and Type	Incident Microwave Power (kW)	Pressure (Torr)	Hydrogen Flow (sccm)	Hydrogen Translational Temperature (K)	Hydrogen Electronic Temperature (K)	Substrate Temperature (C)
1 Center	2.16	50	400	1847	2932	800
2 Center	2.16	50	400	1851	2998	800
3 Center	2.16	50	400	1900	3004	809
4 Center	2.16	50	400	1903	2963	810
5 Center	2.16	50	400	1880	3178	806
6 Factor	1.62	40	330	1539	3210	734
7 Factor	1.62	40	470	1380	2824	740
8 Factor	1.62	60	330	1979	2621	821
9 Factor	1.62	60	470	1786	2533	810
10 Factor	2.412	40	330	1975	3161	751
11 Factor	2.412	40	470	1673	3045	752
12 Factor	2.412	60	330	1957	2968	847
13 Factor	2.412	60	470	2199	2522	861
14 Star	1.404	50	400	1564	2694	758
15 Star	2.592	50	400	2074	3418	825
16 Star	2.16	35	400	1554	3024	724
17 Star	2.16	65	400	2022	2445	840
18 Star	2.16	50	300	1811	3115	803
19 Star	2.16	50	500	1885	2781	801
			SSE =	2787	36572	92

height and probe depth were adjusted to minimize reflected power. The effect of pressure, incident power and hydrogen flow on percent of incident power absorbed was examined using the ANOVA techniques. Table 4.4 shows the resulting ANOVA. Pressure and incident power were the only significant factors.

In terms of the models, absorbed power and pressure show a correlation of -0.355 which indicates as the pressure goes up the absorbed power tends to decrease. Additionally, though, absorbed power and incident power showed a high correlation (0.907) which indicates incident power and absorbed power vary in an almost identical manner. This would indicate either absorbed power or incident power can be used in the following analyses since the effect of absorbed power is included in the pressure and incident power terms. This is born out in a regression model which includes both incident and absorbed power. The significance of absorbed power, for instance is very low compared with incident power and pressure.

Since the analysis of variance showed only main effects were significant and the linearity checks were satisfied, linear regression models were considered. Both backward elimination and forward model-building procedures using all three main effects revealed incident power and pressure effects were significant at a level of 0.10. Hydrogen

Table 4.4 ANOVA results for translational temperature and percent absorbed power.

	Translational Temperature			**Percent Absorbed Power**		
	Mean Square	**DF**	**α**	**Mean Square**	**DF**	**α**
Pressure	229,164	1	0.027	0.016	1	0.000
Inc Power	156,800	1	0.051	0.013	1	0.001
H Flow						
Error	24,086	4		< 0.01	5	

flow effects were shown to be non-significant. The final regression model is:

Predicted Translational Temperature (K) = 228.6 + 374.3 * Incident Power (kW) + 16.5 * Pressure (Torr) ± 94.2

The coefficient of determination (R^2) for this model is 0.815. The error term included in the regression models is one standard deviation of the predicted values from the mean observed values. A plot of the predicted translational temperature is shown as Figure 4.6. Nonlinear regression using absorbed power, pressure, and the interaction between these two effects showed the interaction to be nonsignificant. The scatterplot of predicted translational temperature versus the actual translational temperature is shown as Figure 4.7, where in a perfect fit all of the predicted temperatures would fall on a straight line through the origin (x = y).

The sum of squares for the residuals (*SSR*) is 142,062 for this model. With *SSE* = 2787, the lack-of-fit is significant at a level of $\alpha = 0.02$. This is determined by calculating the mean sum of squares due to experimental error (*MSSE*) and the mean square due to lack-of-fit (*MSSL*). Recall *SSL* = *SSR* - *SSE*, that is, *SSL* is the portion of the residual error NOT due to experimental error [75]. For example:

$$SSE = 2787$$

$$SSL = 142{,}062 - 2787 = 139{,}275$$

$$MSSE = \frac{SSE}{5 - 1} = \frac{2787}{4} = 697$$

$$MSSL = \frac{SSL}{16 - 4} = \frac{139{,}275}{12} = 11{,}606$$

$$F = \frac{MSSL}{MSSE} = 16.7$$

α is determined from tables of a F(12,4) distribution.

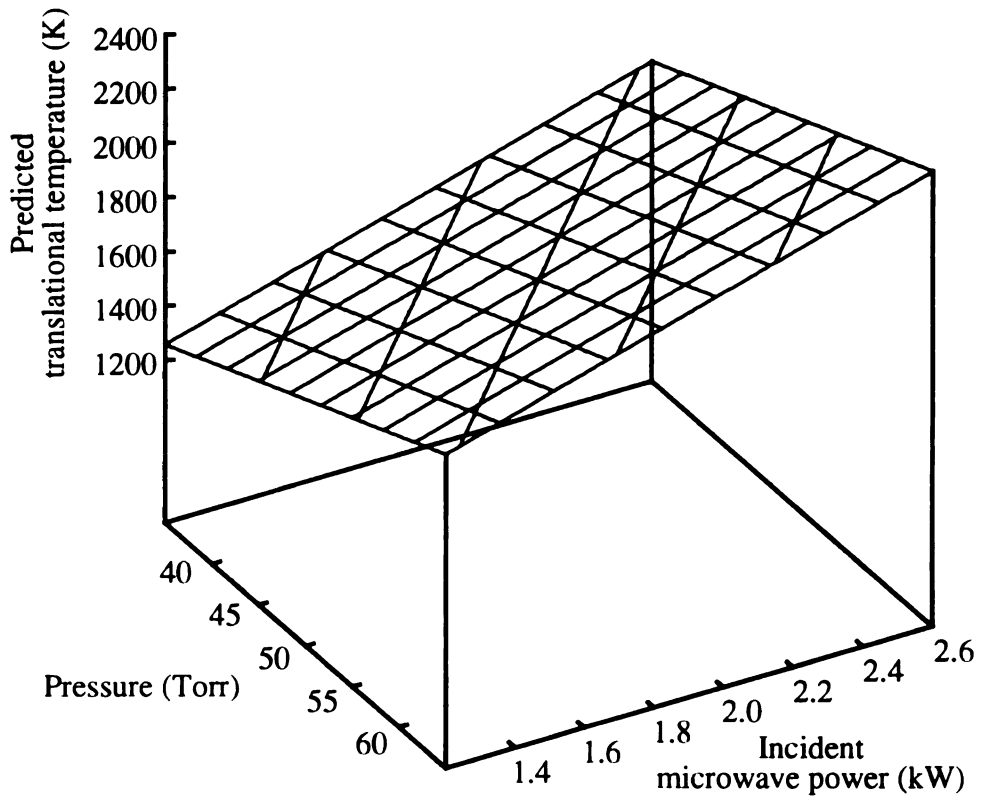

Figure 4.6: Predicted hydrogen translational temperature.
Contours at 1400, 1600, 1800, 2000, 2200 K.

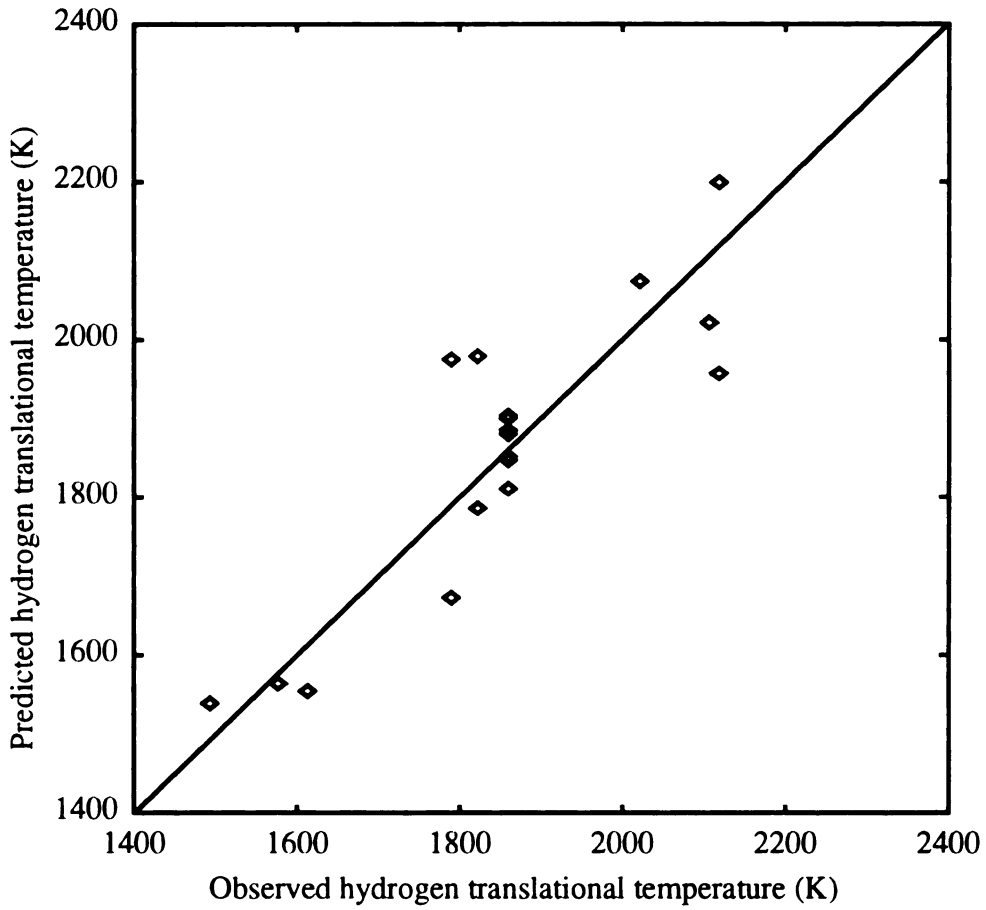

Figure 4.7: Scatterplot of predicted hydrogen translational temperature versus observed translational temperature. The straight line represents perfect agreement between observed and predicted values.

4.3.2 Electronic temperature results

The electronic temperature results were analyzed using the same procedures as the previous temperature. The ANOVA of electronic temperature initially showed the first order effects were non-significant at an α of 0.8. Pooling these factors with error showed incident power is not a major effect with an α of 0.2. The major effects for our parameter range on electronic temperature are pressure and hydrogen flow at a significance level of $\alpha = 0.034$. The final ANOVA results for electronic temperature are shown in Table 4.5.

The regression analysis of electronic temperature produced some results which may seem surprising. The regression techniques, both forward and backward, allowed all three main effects, pressure, power and flow to remain indicating they are significant at $\alpha = 0.05$ which is the P_{in} value for the forward regression model building technique (see Section 3.3.4). In the regression analysis all fifteen experimental points are used in the least squares fit. This includes the star points and the center point. The two-way ANOVA used only the eight experimental data points associated with the 2^3 factorial design. Use of all of the data in the least squares regression analysis produced the following model:

Predicted Electronic Temperature (K) = 3961.1 + 316.0 * Incident Power (kW) - 17.7 * Pressure (Torr) - 1.79 * Hydrogen Flow (sccm) ± 154.8

with $R^2 = 0.710$. The first order interactions did not add a significant amount of new information so they were not included in the analysis. The predicted electronic temperature is shown in Figures 4.8 and 4.9. The scatterplot of the predicted electronic temperature against the observed electronic temperature is shown as Figure 4.10. From the coefficient of determination, 71% of the observed variation is accounted for in the model. The amount of error due to lack of fit over experimental error is significant at a level of $\alpha = 0.1$ from the analysis of $SSE = 36572$ and $SSR = 359800$.

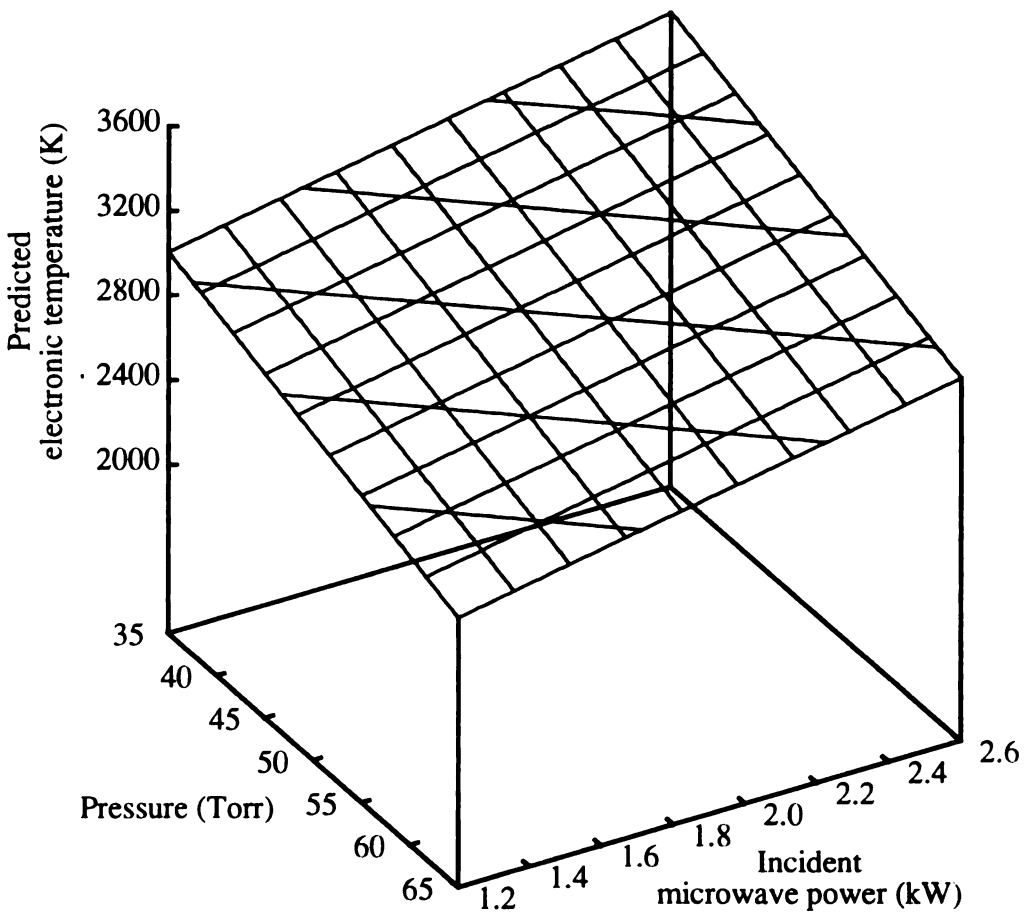

Figure 4.8: Predicted hydrogen electronic temperature versus pressure and power. Contours are at 2640, 2800, 2960, 3120, and 3280 K.

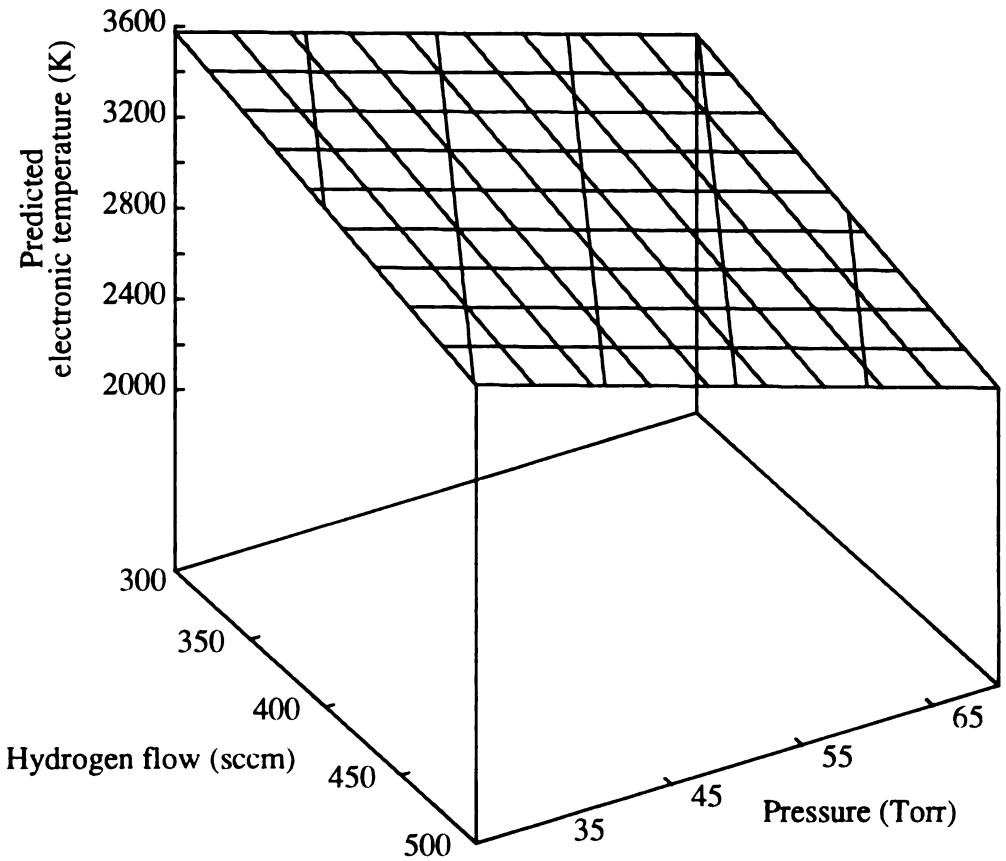

Figure 4.9: Predicted hydrogen electronic temperature (K) versus pressure and flow. Contours at 2640, 2800, 2960, 3120, and 3280 K.

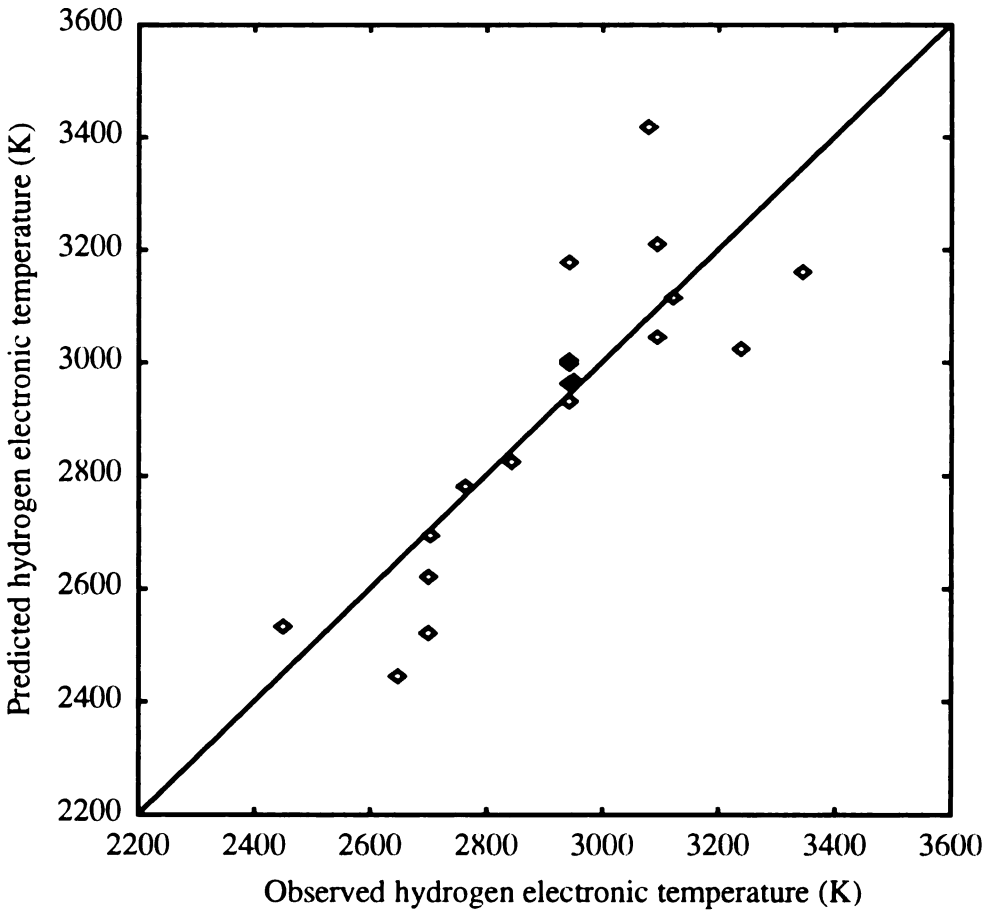

Figure 4.10: Scatterplot of predicted hydrogen electronic temperature versus observed electronic temperature.

4.3.3 Substrate temperature results

The substrate temperature was measured at the center of the wafer for each of the nineteen experiments. The observed F-test values found in the analysis of variance indicate the first order interactions are non-significant at an α of 0.35. Also, hydrogen flow is non-significant at an α of 0.70. Pooling these factors in with error reveals pressure and incident power are significant at an α of 0.01. The final mean square and α values are listed in Table 4.5.

Table 4.5 ANOVA results for electronic temperature and substrate temperature.

	Electronic Temperature			**Substrate Temperature**		
	Mean Square	**DF**	α	**Mean Square**	**DF**	α
Pressure	318.402	1	0.008	16380.5	1	0.000
Inc Power	32.258	1	0.196	1404.5	1	0.012
H Flow	134.162	1	0.034			
Error	13.439	4		93.00	5	

Since the first order interactions were found to be non-significant in the two-way ANOVA, linear regression was used to determine the model of substrate temperature over our parameter space. The regression analysis was performed using both the backward and forward model building techniques and both techniques yielded identical results. Although included initially, hydrogen flow does not appear in the final model as expected from the two-way ANOVA:

$$\text{Predicted Substrate Temperature (°C)} = 490.89 + 4.29 * \text{Pressure (Torr)} + 42.75 * \text{Incident Power (kW)} \pm 10.5$$

The R^2 for this model is 0.938 which indicates the model will predict greater than 90% of the variation in substrate temperature over our parameter range. The predicted substrate temperature is plotted in Figure 4.11. The scatterplot of predicted substrate temperature

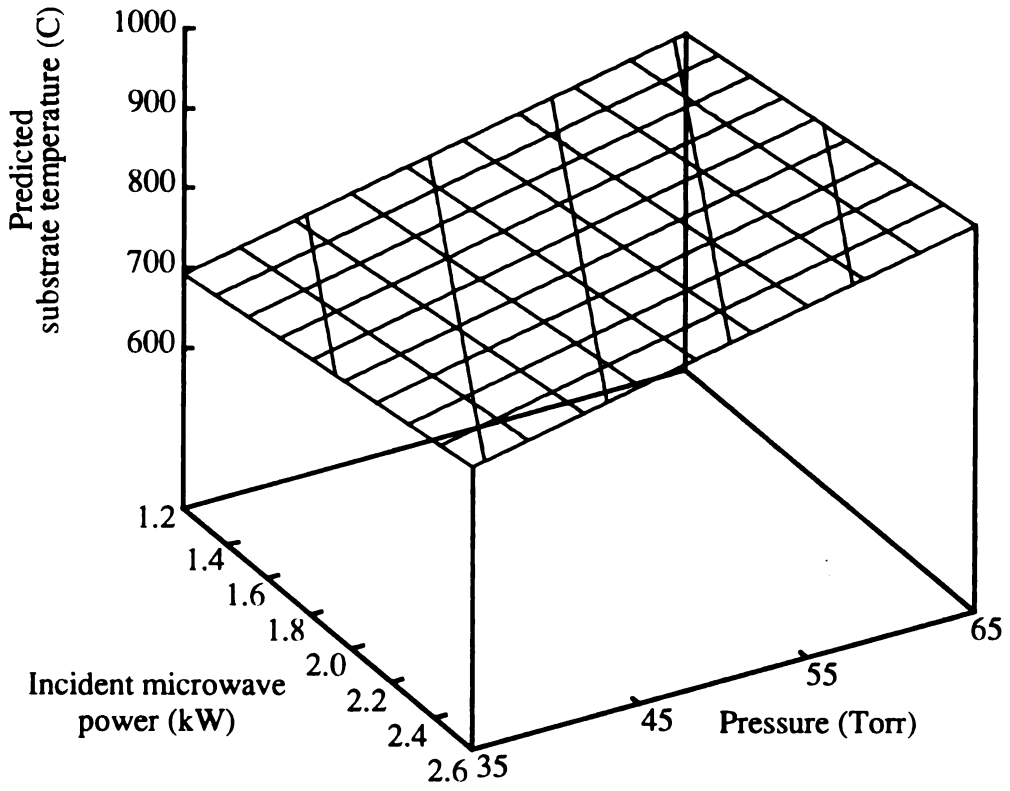

Figure 4.11: Predicted substrate temperature.
Contours at 700, 750, 800, 850, 900 C.

Table 4.6 Statistically designed experiments for the diamond deposition reactor (Part II)

Run # and Type	Incident Microwave Power (kW)	Pressure (Torr)	Hydrogen Flow (sccm)	Actinometry Ratio	C_2 Rotational Temp (K)	Plasma Volume (cm^3)	Power Density (W/cm^3)
1 Center	2.16	50	400	1.362	1266	109	15.9
2 Center	2.16	50	400	1.370	1129	96	17.5
3 Center	2.16	50	400	1.270	1181	103	16.0
4 Center	2.16	50	400	1.320	1118	108	15.4
5 Center	2.16	50	400	1.280	1045	N/A	N/A
6 Factor	1.62	40	330	2.200	1369	108	11.9
7 Factor	1.62	40	470	2.390	1190	99	12.9
8 Factor	1.62	60	330	1.150	1066	79	16.9
9 Factor	1.62	60	470	1.180	1342	77	17.5
10 Factor	2.412	40	330	2.460	1362	214	8.0
11 Factor	2.412	40	470	2.340	1927	185	9.3
12 Factor	2.412	60	330	1.200	1497	108	18.6
13 Factor	2.412	60	470	1.180	2257	93	20.1
14 Star	1.404	50	400	1.450	1153	76	16.1
15 Star	2.592	50	400	1.240	2000	160	11.7
16 Star	2.16	35	400	2.810	1253	262	5.9
17 Star	2.16	65	400	1.030	1405	75	23.6
18 Star	2.16	50	300	1.350	1011	101	16.7
19 Star	2.16	50	500	1.380	1675	109	15.2
			SSE =	0.0084	22883	106	2.46

versus actual substrate temperature is shown in Figure 4.12. The lack of fit is significantly greater than the experimental error at a level of $\alpha = 0.05$ with $SSE = 92$ and $SSR = 1754$ for this model.

4.3.4 Relative atomic hydrogen concentration results

Following the analysis of variance procedures of the previous sections, the actinometry ratio was analyzed. The data is presented in Table 4.6. Only one effect was found to be significant. After pooling first order effects and the effects of hydrogen flow and incident power in with error, the effect of pressure on the relative atomic hydrogen concentration is clearly the most significant (Table 4.7) at an α of less than 0.001. The regression analysis on the entire data set revealed the same results. The model with an R^2 of 0.796 is:

$$\text{Actinometry Ratio } (I_H/I_{Ar}) = 4.517 - 0.059 * \text{Pressure} \pm 0.25$$

Figure 4.13 is a plot of the regression model for the parameter range studied here. Figure 4.14 shows the scatterplot of the predicted ratio versus the observed ratio. This simple model predicts nearly 80% of the variation in the ratio of the two emission lines with most of the residual error in the model due to lack-of-fit. $SSE = 0.0084$ and $SSR = 1.10$ and the significance level for the lack-of-fit is $\alpha = 0.001$.

Table 4.7 ANOVA results for relative hydrogen concentration and C_2 rotational temperature.

	Relative Hydrogen Concentration			**C_2 Rotational Temperature**		
	Mean Square	**DF**	**α**	**Mean Square**	**DF**	**α**
Pressure	273.78	1	0.000			
Inc Power				538.722	1	0.013
H Flow				252.760	1	0.045
H Flow X Inc Pow				188.498	1	0.067
Error	0.63	6		30.254	4	

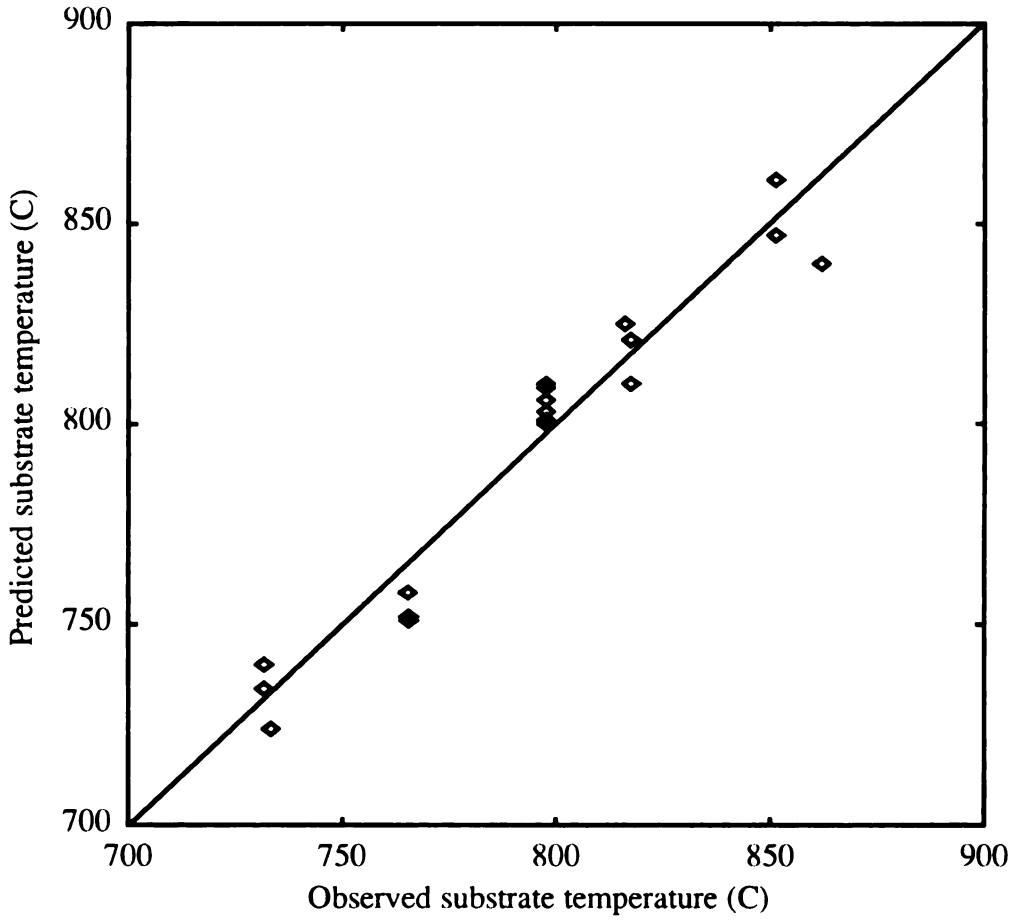

Figure 4.12: Scatterplot of predicted substrate temperature versus observed substrate temperature. Straight line represents perfect agreement between observation and prediction.

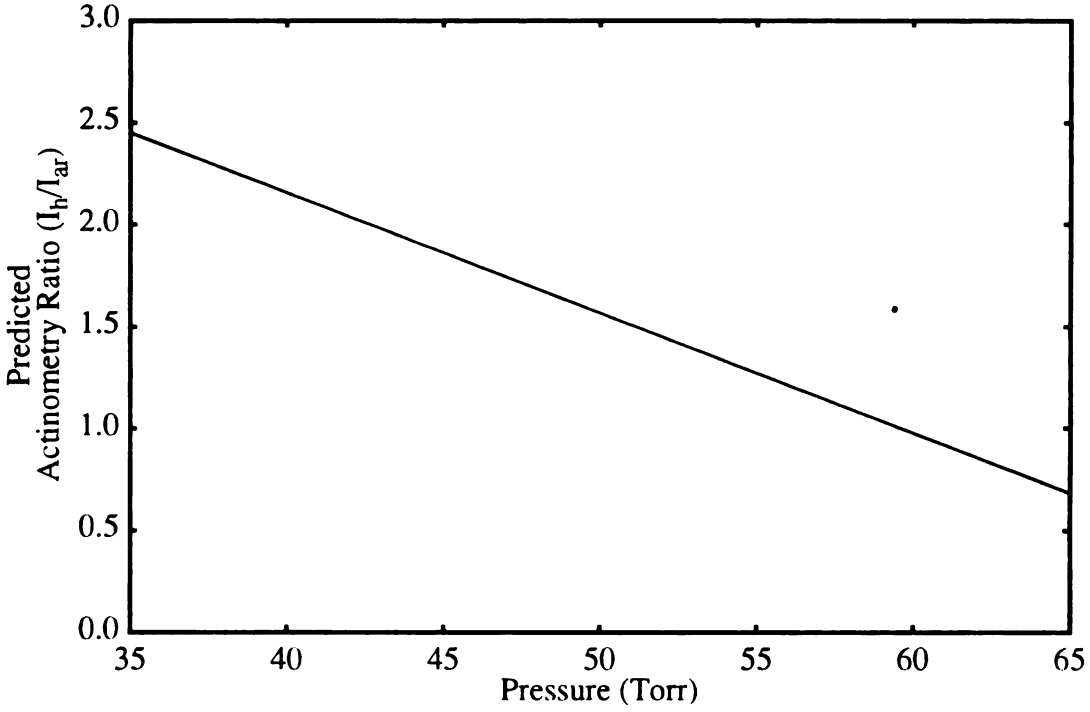

Figure 4.13: Predicted actinometry ratio (relative hydrogen concentration).

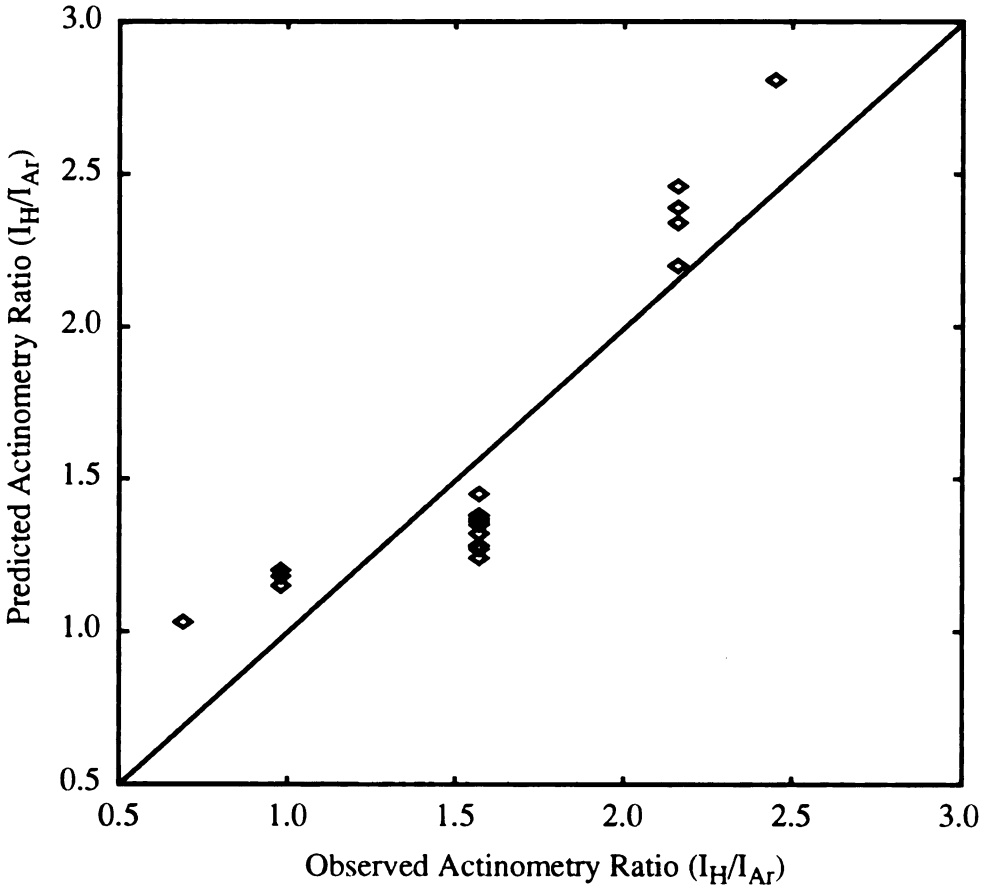

Figure 4.14: Scatterplot of predicted actinometry ratio versus observed actinometry ratio. Straight line represents perfect agreement between observation and prediction.

4.3.5 C_2 rotational temperature results

The analysis of variance of the rotational temperature indicates incident power is the most significant factor at a significance of less than 0.055 as listed in Table 4.7. The curve fit data, though, show rotational temperature is not a linear function of incident power. Figure 4.15 shows a quadratic fit to incident power fits with an R^2 of 0.959. The regression model used is, therefore, a function of both incident power and the square of incident power:

> Predicted C_2 Rotational Temperature (K) = 6531.99 - 6591.59 * Incident Power (kW) + 1655.48 * Incident Power (kW) * Incident Power (kW) + 1.46 * Hydrogen Flow (sccm) * Incident Power (kW) ± 180.2

The coefficient of determination (R^2) for the entire model is 0.777. Figure 4.16 shows the scatterplot of predicted rotational temperature versus observed rotational temperature. The predicted rotational temperature is plotted in Figure 4.17. For this model, SSE = 22883 and SSR = 487001, the lack-of-fit portion of the residual error variance was significant at a level of $\alpha = 0.03$.

This model of rotational temperature fits adequately to the data but is missing any pressure dependence. All of the other models include a pressure dependent term. Perhaps the experimental error is too large for this effect to be accounted for in the regression. The regression analysis was repeated and the P_{out} constraint was loosened to a value of 0.2 (see Section 3.3.4). The pressure dependence remained in the backward elimination regression. The model with a slightly improved R^2 of 0.788 is:

> Predicted C_2 Rotational Temperature (K) = 6315 - 6591.6 * Incident Power (kW) + 1655.48 * Incident Power (kW) * Incident Power (kW) + 4.34 * Pressure (Torr) + 1.46 * Hydrogen Flow (sccm) * Incident Power (kW) ± 182.0

The model is plotted in Figure 4.18 to show the pressure dependence. The residual sum of squares is SSR = 463,503.

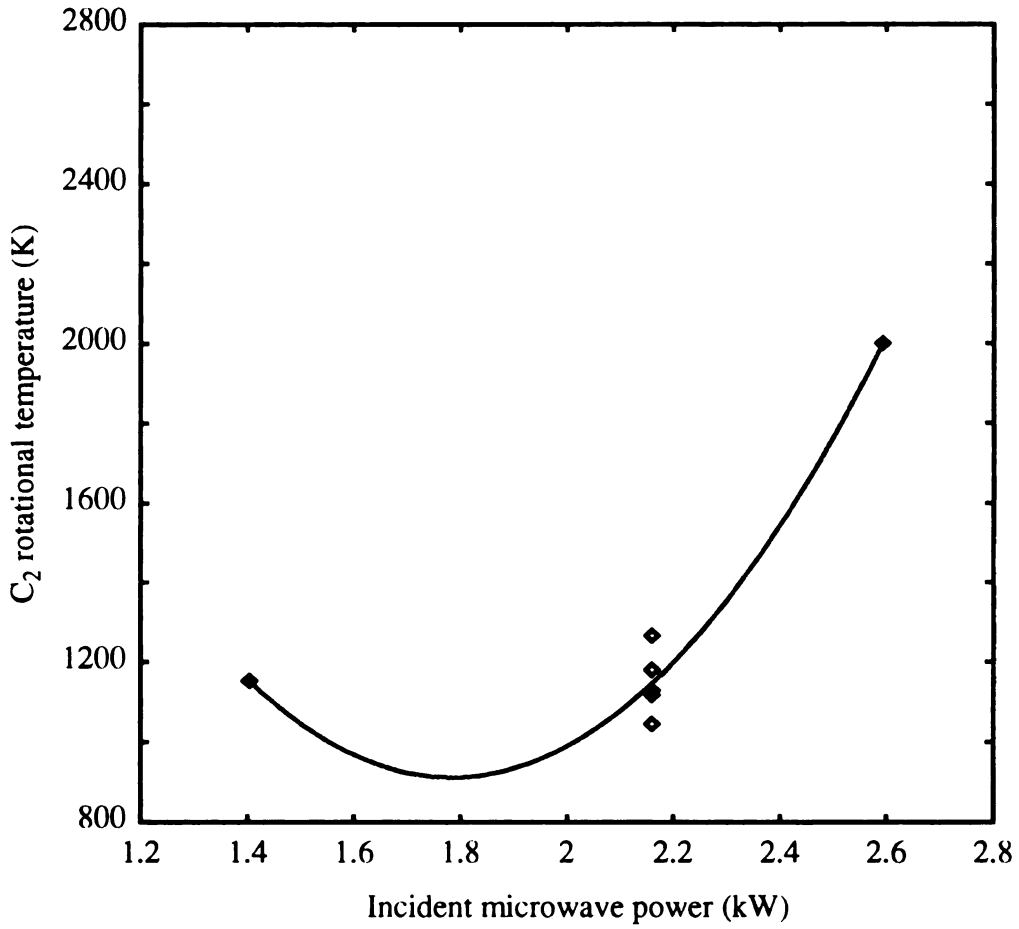

Figure 4.15: Quadratic least squares fit of C_2 rotational temperature to incident microwave power. Pressure = 50 Torr and hydrogen flow = 400 sccm.

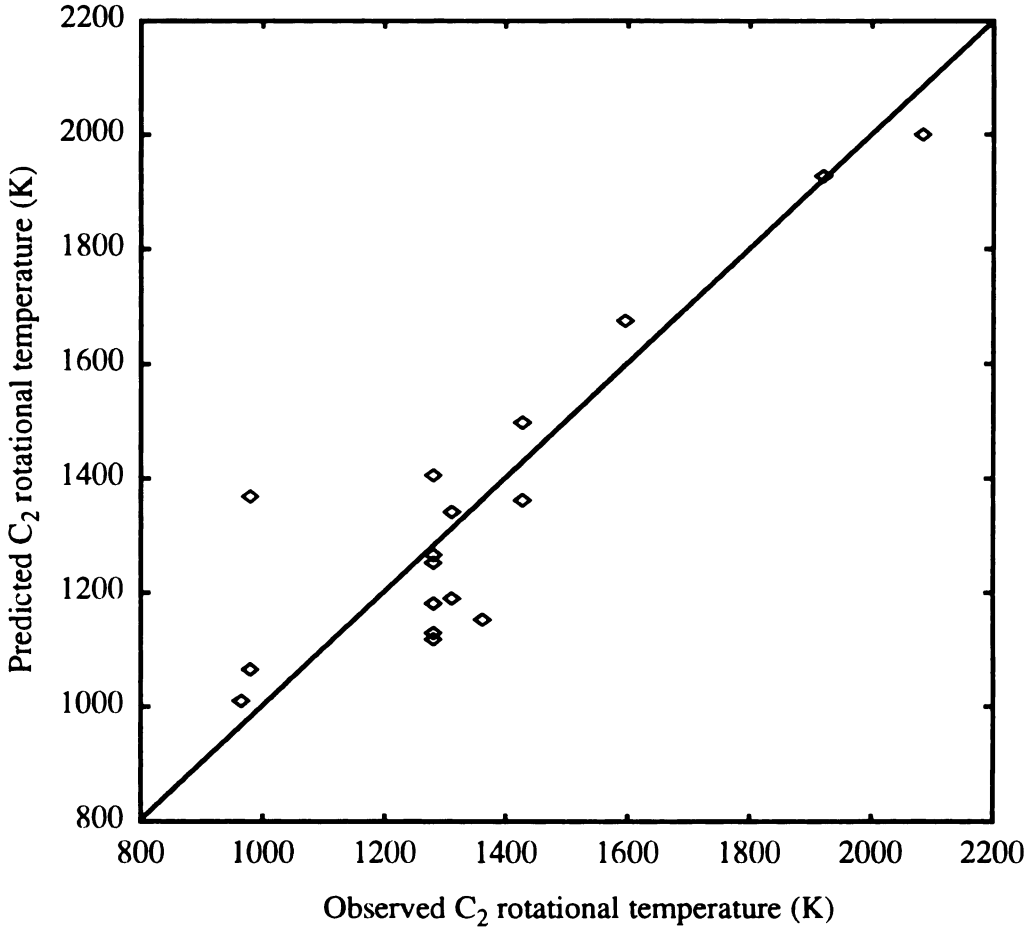

Figure 4.16: Scatterplot of predicted C_2 rotational temperature versus the observed C_2 rotational temperature. Straight line represents perfect agreement between prediction and observation.

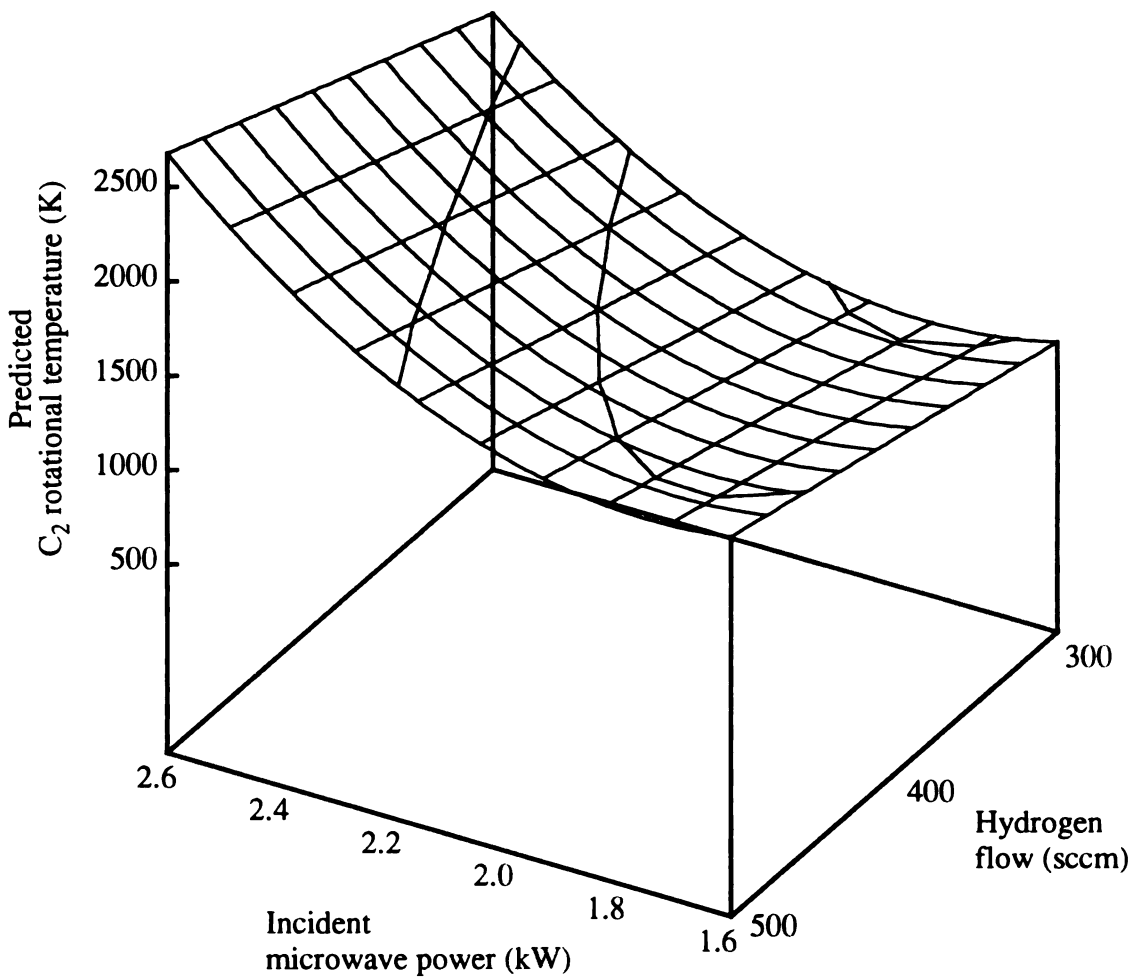

Figure 4.17: Predicted C_2 rotational temperature.
Contours at 1000, 1400, 1800 K.

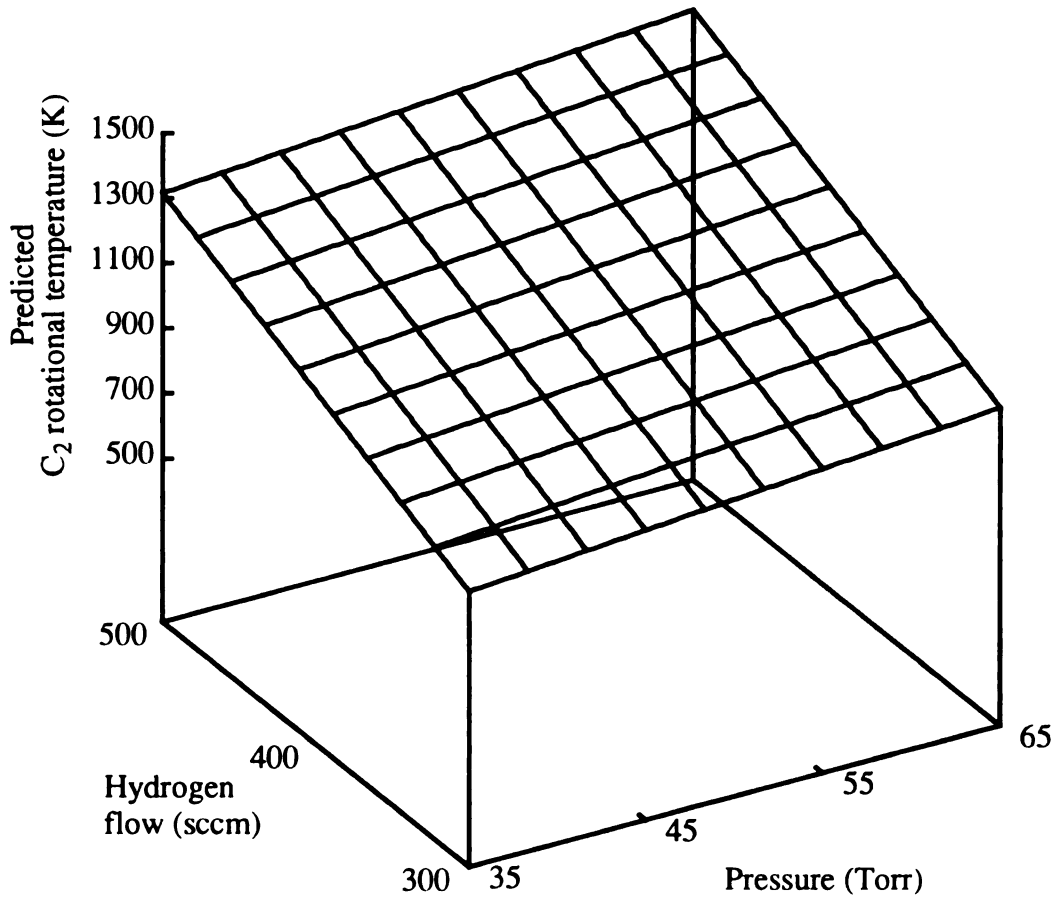

Figure 4.18: Predicted C_2 rotational temperature including the pressure dependence.

4.3.6 Plasma volume results

The analysis of the plasma volume variation over the range of pressure, incident microwave power and hydrogen flow show volume varies quadratically with pressure and incident power. The ANOVA corroborates the dependence on these two factors. Table 4.8 shows the ANOVA of plasma volume. The pressure and incident power main effects and the first order interaction of pressure and incident power are significant at a level of 0.012.

The regression analysis of plasma volume took into account the apparent quadratic

Table 4.8 ANOVA of plasma volume and plasma density

	Plasma Volume (cm^3)			**Power Density (W/cm^3)**		
	Mean Square	**DF**	α	**Mean Square**	**DF**	α
Incident Power	7021.12	1	0.002	1.28	1	0.026
Pressure	7750.13	1	0.002	120.13	1	0.000
Hydrogen Flow				2.42	1	0.011
Inc Power X Press	2701.13	1	0.0012	17.41	1	0.001
Error	143.87	4		0.08	3	

dependence on pressure and incident power. The final model with an R^2 of 0.937 is:

Predicted Plasma Volume (cm^3) = 449.7 + 116.2 * Incident Power (kW) - 18.1 * Pressure (Torr) + 57.1 * [Incident Power (kW)]^2 + 0.25 * [Pressure (Torr)]^2 - 5.4 *Pressure (Torr) * Incident Power (kW) ± 15.4

The predicted plasma volume is plotted in Figure 4.19.

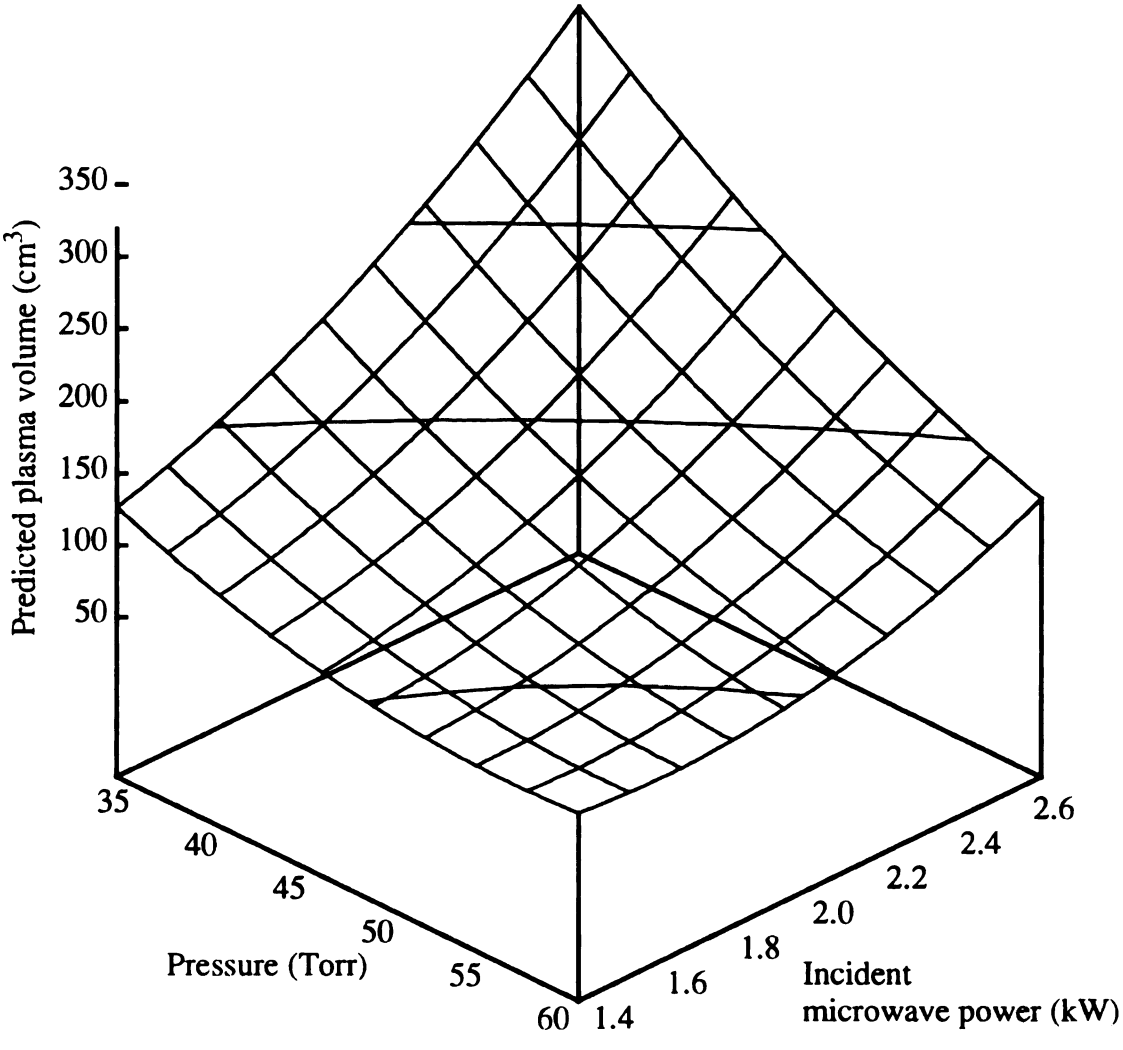

Figure 4.19: Predicted plasma volume. Contours at 75, 150 and 225 cm^3.

4.3.7 Power density results

The analysis of variance of the power density calculations are listed in Table 4.8. The main effects were all significant at a level of 0.026 or better. Also, the pressure by incident power first order effect was highly significant at $\alpha = 0.001$.

Using the results of the ANOVA, pressure, incident power, hydrogen flow and the interaction of pressure and power were included in the model:

Predicted Power Density (W/cm^3) = 38.23 - 0.41 * Pressure (Torr) - 22.4 * Incident Power (kW) + 0.003 * Hydrogen Flow + 0.42 * Pressure (Torr) * Incident Power (kW) ± 1.5

The R^2 of the final model is 0.902. Figure 4.20 is a plot of the predicted power density versus pressure and incident power.

4.4 Conclusions

This series of experiments has allowed us to examine the temperature and concentration of the various atomic and molecular species present in the microwave diamond deposition discharge. The experiments were statistically designed to maximize the amount of information gathered while minimizing the experimental cost. Also, models of species temperature and concentration were developed based on the data collected for the range of pressure, power and hydrogen/methane flow described.

The hydrogen translational temperature increases with microwave power and pressure increases. The translational temperature did not change significantly with hydrogen flow changes. The hydrogen electronic temperature increases as microwave power increases. Furthermore, the electronic temperature decreases as pressure and hydrogen flow increase. A contour plot comparing these two temperature degrees of freedom in the diamond deposition reactor is shown in Figure 4.21.

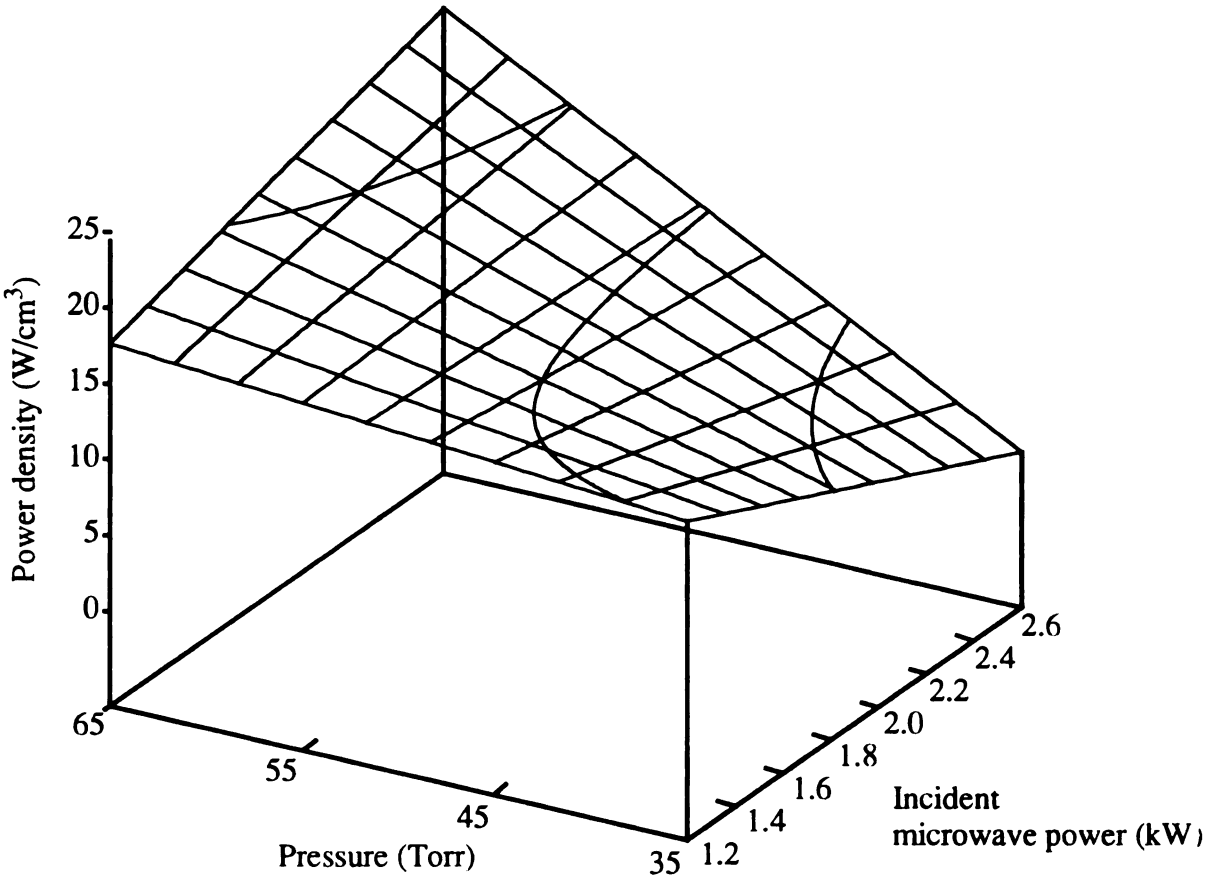

Figure 4.20: Predicted power density. Contours at 10, 15, 20 W/cm^3.

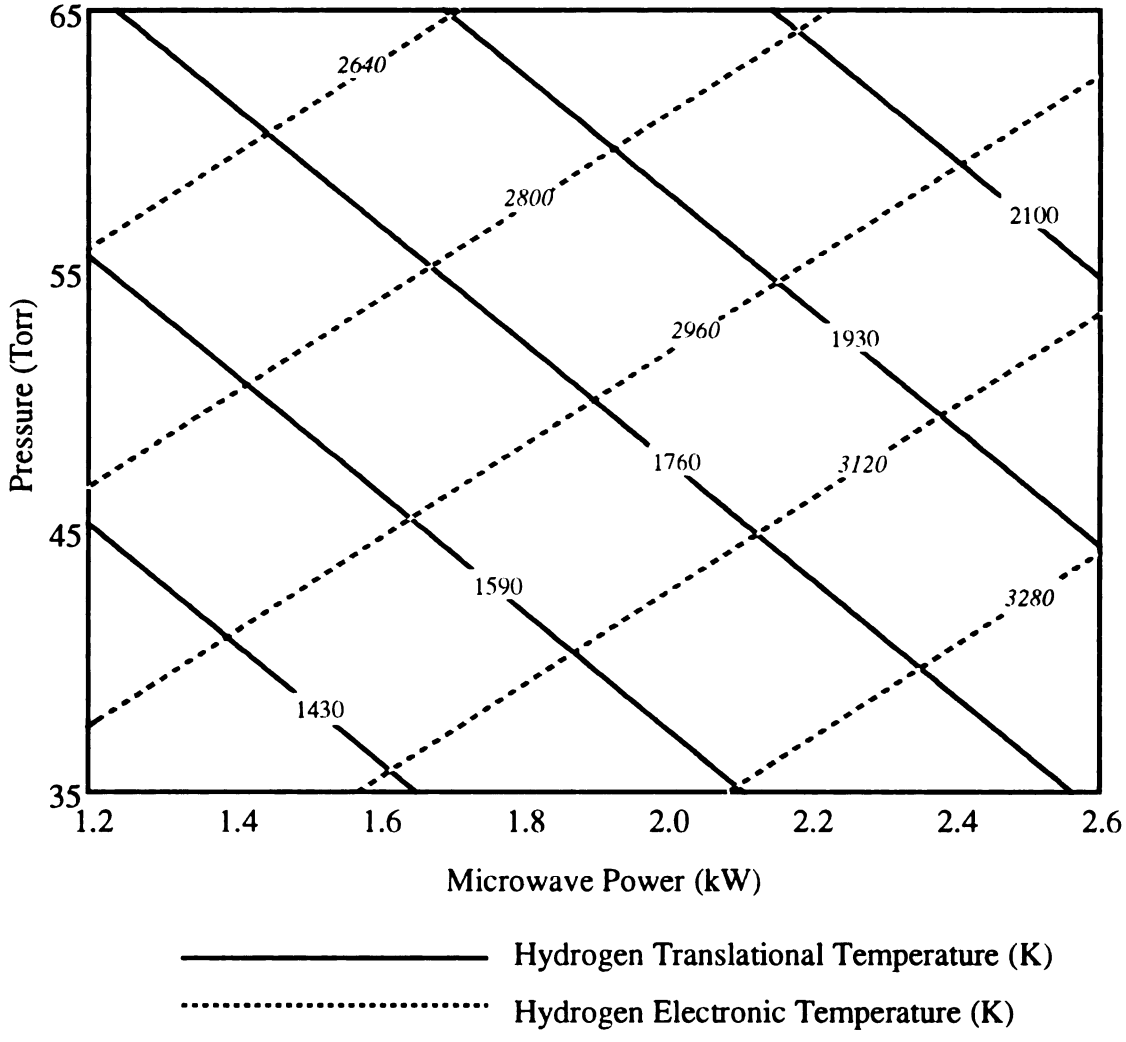

Figure 4.21: Contour plot of hydrogen translational and electronic temperatures. Hydrogen flow = 400 sccm.

The molecular C_2 rotational temperature model is slightly more complicated. The rotational temperature is assumed to follow the gas temperature very closely [95]. Since the energy separation between rotational levels in the C_2 molecules is very small, interaction with the translational degrees of freedom is very efficient. The rotational temperature should track the translational temperature fairly well. The rotational temperature though, is a strong function of microwave power. The temperature increases with increased microwave power but shows little significant change with pressure variation. The rotational temperature also increased as a function of a hydrogen flow and microwave power interaction.

The ratio of the hydrogen atomic emission line to the argon neutral emission line drops as pressure is increased but the model predicts no significant changes as microwave power and hydrogen flow are varied. Although, the actinometry ratio decreases with pressure, the hydrogen atomic concentration does not necessarily decrease. Further investigation of the effects of temperature changes, the dissociation of hydrogen and the choice of actinometer are necessary to quantify the actinometry results.

The substrate temperature model is similar to the hydrogen translational temperature model. Substrate temperature increases when both microwave power and pressure increase. There was no significant change in substrate temperature with hydrogen flow variation. This model will be useful in the operation of the diamond deposition reactor since the importance of a repeatable processing surface temperature to diamond growth has been demonstrated [80].

Chapter 5

Hydrogen-based Discharge Diagnostics at Extended Pressures

5.0 Introduction to the extended pressure hydrogen-based discharges

Diamond films have been grown at pressures ranging from less than 1 Torr to greater than 100 Torr. To extend the experimental investigation of the diamond deposition reactor, a series of experiments were conducted at pressures of 115 - 135 Torr and 0.1 - 0.4 Torr in similar discharges. The low pressure experiments, 0.1-0.4 Torr, were conducted using the same cavity, baseplate and vacuum system as the multipolar ECR reactor except the magnets were removed. The high pressure experiments, 115-135 Torr, were conducted using the same reactor as was used in the diamond deposition diagnostics of Chapter 4 except a water cooled substrate was used.

5.1 High pressure diamond deposition discharge diagnostics

The hydrogen translational and electronic temperatures and the C_2 rotational temperature of the high pressure diamond deposition discharge were measured using the same techniques and experimental set-up described in Chapter 4. The experiments were statistically designed using the principles of Chapter 3. A 2^3 full factorial design was used to determine the effect of pressure, microwave power and hydrogen flow rate on the plasma species' temperatures. The experimental parameters are detailed in Table 5.1 for the pressure range 115 Torr - 135 Torr, incident power ranging from 3.6 kWatts - 4.5 kWatts and hydrogen flow from 450 sccm - 750 sccm.

Table 5.1 High pressure diamond deposition reactor statistically designed experiments.

Run # & Type	Incident Microwave Power (kW)	Pressure (Torr)	Hydrogen Flow (sccm)	Hydrogen Translational Temperature (K)	Hydrogen Electronic Temp (K)	C_2 Rotational Temp (K)
1 Center	3.96	125	600	2072	1904	2022
2 Center	3.96	125	600	1733	1769	1838
3 Center	3.96	125	600	2147	2009	2114
4 Center	3.96	125	600	1868	2027	1965
5 Center	3.96	125	600	1839	2029	2150
6 Factor	4.32	132	500	1834	1960	1949
7 Factor	4.32	132	700	1906	2033	2088
8 Factor	4.32	118	500	2081	2005	1782
9 Factor	4.32	118	700	1982	1773	2293
10 Factor	3.60	132	500	2026	1960	2016
11 Factor	3.60	132	700	2007	1918	1706
12Factor	3.60	118	500	1846	1966	2053
13 Factor	3.60	118	700	1870	2009	2100
14 Star	3.42	125	600	1898	1746	1930
15 Star	4.50	125	600	1797	1853	1890
16 Star	3.96	115	600	1952	2094	1876
17 Star	3.96	135	600	1909	2015	2037
18 Star	3.96	125	450	1800	1932	1988
19 Star	3.96	125	750	2086	1866	1927
			SSE =	118,171	50,499	61,865

5.1.1 Hydrogen translational temperature (high pressure discharge)

The hydrogen translational temperature in the high pressure diamond deposition discharge was determined for each of the nineteen experiments using the techniques described in Section 4.2.1. The analysis of variance for the translational temperature, shown in Table 5.2, indicates the main effects and the first order effects are significant only at a level of $\alpha = 0.2$ or greater. The incident power by pressure first order effect is the

most significant of the six effects examined but its significance level of $\alpha = 0.205$ does not meet the significance criteria set forth in Chapter 4. In other words, at a significance level of $\alpha = 0.2$ the variation in hydrogen translational temperature would be incorrectly explained by this particular interaction about 1 time out of every 5 observations. The "odds" of correctly explaining the variation in translational temperature by the remaining first order and main effects are even worse.

Table 5.2 ANOVA for high pressure hydrogen translational and electronic temperatures.

	Hydrogen Translational Temperature			**Hydrogen Electronic Temperature**		
	Mean Square	**DF**	α	**Mean Square**	**DF**	α
Pressure	4.5	1	0.982	1740.5	1	0.813
Incident Power	364.5	1	0.843	840.5	1	0.868
Hydrogen Flow	60.5	1	0.935	3120.5	1	0.755
Power X Pressure	51200.0	1	0.205	12168.0	1	0.570
Power X Flow	128.0	1	0.906	3200.0	1	0.752
Flow X Pressure	2048.0	1	0.657	6050.0	1	0.673
Error	5724.5	1		19012.5	1	

The ANOVA in this case is not very informative because the variation in hydrogen translational temperature with changes in pressure, microwave power and hydrogen flow rate are very small when compared to the experimental error. Figure 5.1 shows the least squares fit of hydrogen translational temperature to the center points (Runs #1-5 in Table 5.1) and the two star points (Run #14 and Run #15) for incident power. Note that the variation between the temperature at the highest power star point and the temperature at the lowest power star point is actually less than the difference between the highest and lowest temperatures at the center power point. The mean temperature for the five center points is 1932 K. The standard deviation about the mean is 172 K. The mean temperature for all

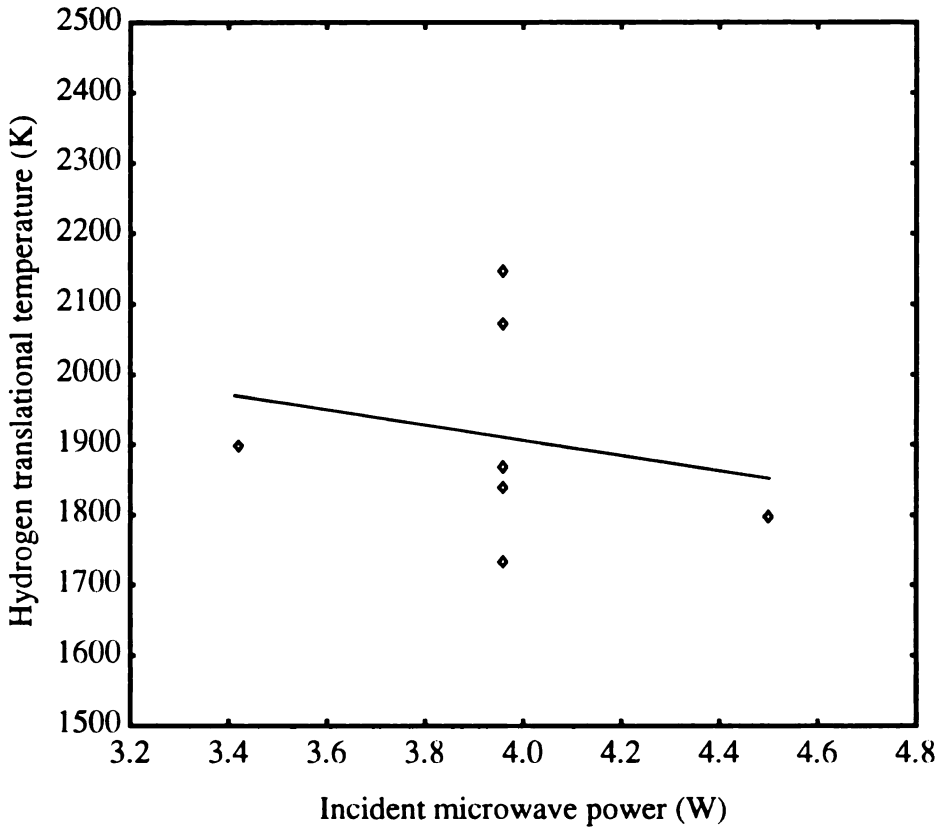

Figure 5.1: Least squares fit of hydrogen translational temperature to incident microwave power for the high pressure hydrogen/methane discharge. Pressure = 125 Torr and hydrogen flow = 600 sccm.

nineteen experimental runs is 1944 K with a standard deviation of 92 K. Statistically, there is no significant variation at an $\alpha = 0.205$ of hydrogen translational temperature with changes to microwave power, pressure nor hydrogen flow in the parameter space studied here.

5.1.2 Hydrogen electronic temperature (high pressure discharge)

The hydrogen electronic temperature was determined for the high pressure diamond deposition reactor using the two-line radiance ratio method described in Section 4.2.2. The data from the nineteen experiments is shown in Table 5.1. The analysis of variance was performed using the statistics described in Chapter 4. The ANOVA is shown in Table 5.2. In a manner similar to the translational temperature results, the electronic temperature showed no significant variation at an $\alpha = 0.570$ with any of the six effects studied.

The mean electronic temperature from the five center points in Table 5.1 is 1948 K with a standard deviation of 112 K. The mean electronic temperature for all nineteen data points is 1953 K with a standard deviation of 81 K. The deviation in experimental error is greater than that for the entire set of data and they have similar mean values. This indicates that there is little significant variation in electronic temperature for the range of pressure, power and flow studied here.

5.1.3 C_2 rotational temperature (high pressure discharge)

The rotational temperature for the high pressure diamond deposition reactor was determined from the spectra of the C_2 Swan band in the same manner as described in Section 4.2.4. The analysis of variance of the rotational temperature is shown in Table 5.3. All six factors in this case are significant at a level of $\alpha = 0.04$ or less.

Although the significance level for all of the six effects in this ANOVA seem to indicate a strong connection to the rotational temperature variation, the regression analysis

leads to another conclusion. The nonlinear least squares regression was performed on the rotational temperature data using all six effects. Using the backward elimination regression method, some of the effects were removed as insignificant when compared to the entire nineteen data points. The final model is given by:

Predicted C_2 Rotational Temperature (K) = 10023.2 - 4046.8 * Incident Power (kW) + 3.51 * Hydrogen Flow (sccm) * Incident Power (kW) - 0.11 * Hydrogen Flow (sccm) * Pressure (Torr) + 15.86 * Pressure (Torr) * Incident Power (kW) ± 100.5

The coefficient of determination (R^2) is 0.587. The predicted value of rotational temperature is plotted against the observed rotational temperature in Figure 5.2. Figure 5.3 shows the plot of predicted rotational temperature plotted versus hydrogen flow and microwave power at a pressure of 125 Torr. The figures and the low value of R^2 indicate a poor fit to the observed temperatures. The high standard error (100.5 K) of the model is also an indication of a poor fit.

Table 5.3 ANOVA of the high pressure C_2 rotational temperature and substrate temperature.

	C_2 Rotational Temperature			**Substrate Temperature**		
	Mean Square	**DF**	**α**	**Mean Square**	**DF**	**α**
Pressure	977.6	1	0.020	2415.1	1	0.081
Incident power	249.6	1	0.040	8256.1	1	0.010
Hydrogen flow	665.6	1	0.025			
Power X Pressure	686.44	1	0.024			
Power X Flow	3704.7	1	0.010			
Flow X Pressure	2362.0	1	0.013			
Error	28.12	1		506.3	5	

The variance of the rotational temperature is determined using the two-level portion of the data without the star points. The regression analysis takes into account all nineteen data points. The conclusion is, again, that the variation in rotational temperature

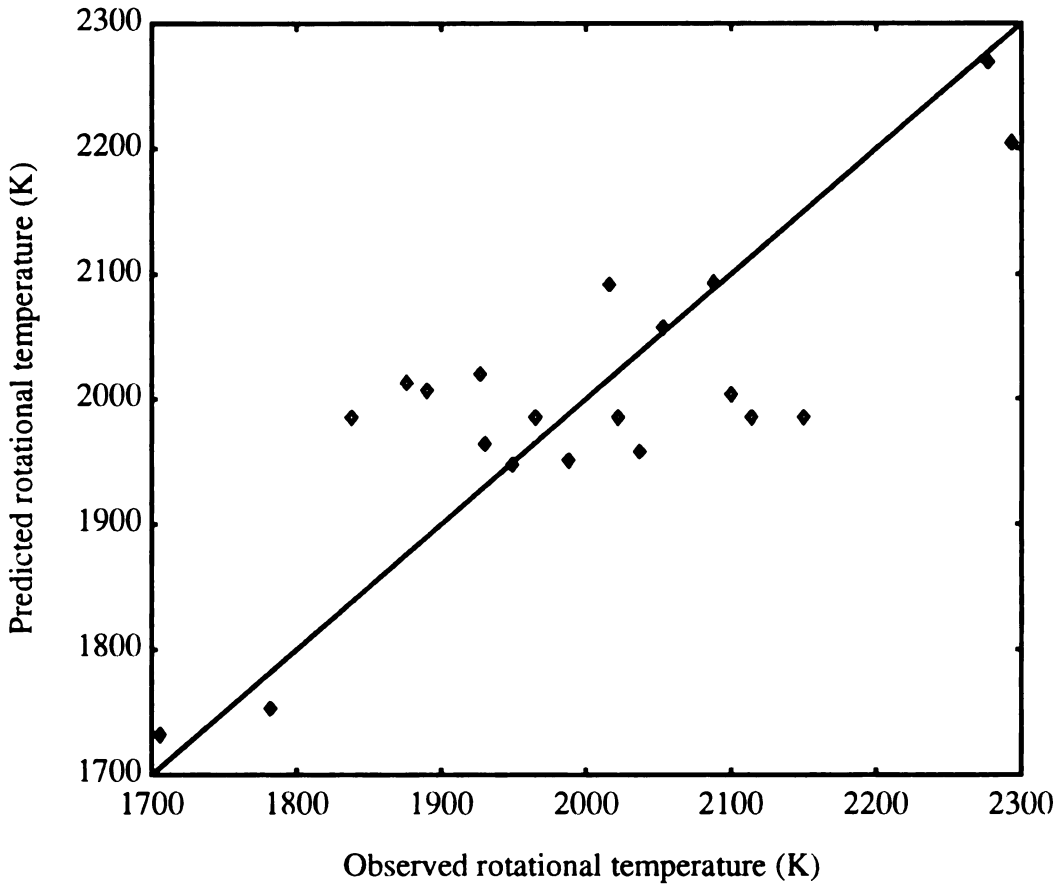

Figure 5.2: Scatterplot of observed C_2 rotational temperature plotted versus predicted C_2 rotational temperature. Straight line represents perfect agreement between observed and predicted values.

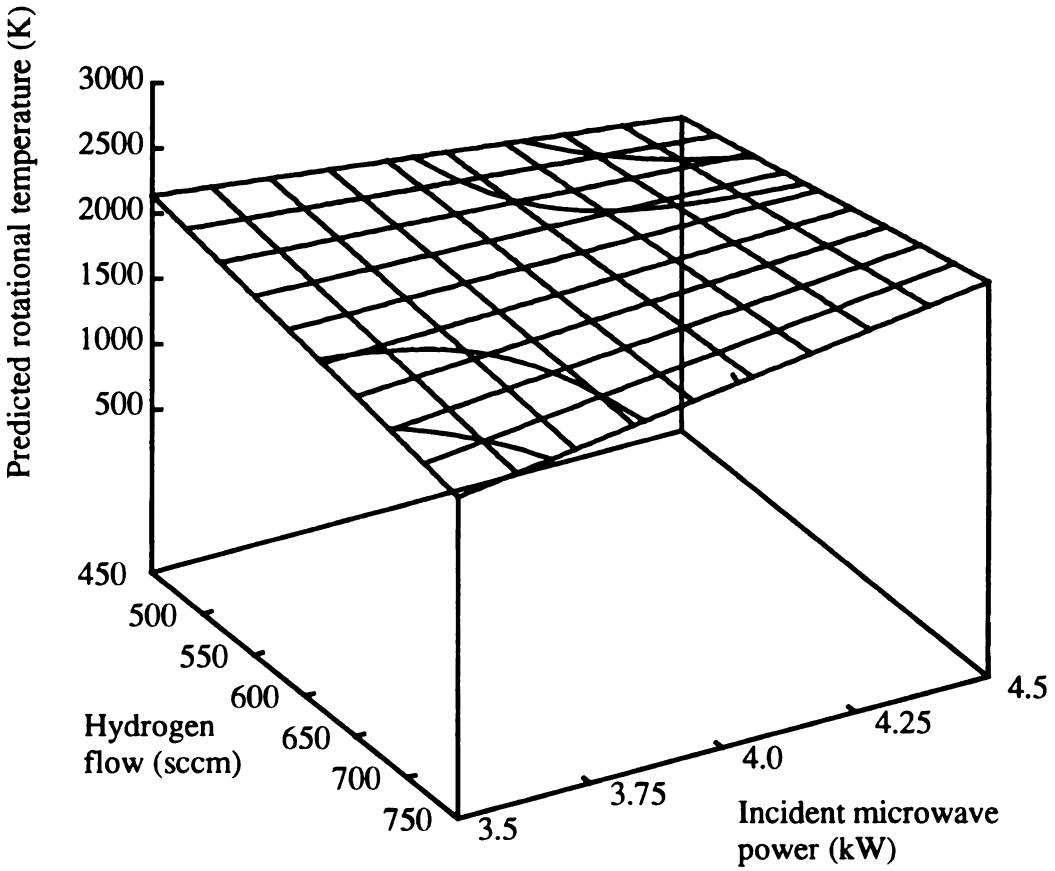

Figure 5.3: Predicted C_2 rotational temperature for the high pressure diamond deposition reactor versus hydrogen flow and incident microwave power. Pressure = 125 Torr, contours at 1800 and 1900 K.

cannot be adequately explained by changes in power, pressure or hydrogen flow over this parameter space and with the current experimental error. The mean value of the rotational temperature is 1999 K with a standard deviation of 186 K for all nineteen data points and the mean of the five center points is 2017 K with a standard deviation of 124 K.

5.1.4 Substrate temperature (high pressure discharge)

The substrate temperature was measured at the center of the 2" wafer for each of the nineteen experimental runs. The substrate holder was kept water cooled for the high pressure experiments to prevent damage to the holder or the wafer and to keep the substrate temperature at a level known to be important for diamond growth [80]. The analysis of variance for the substrate temperature is shown in Table 5.3. The incident power and pressure effects are both significant at a level of $\alpha = 0.08$ or less.

The least square fits of substrate temperature to the incident power, pressure and hydrogen flow star and center points showed no significant non-linear dependence. A linear regression was therefore performed on substrate temperature which initially included all three of the main effects (pressure, power and flow). Using the backward elimination regression method described in Chapter 4, the only effects significant at a level less than the $P_{out} = 0.05$ level are incident power and pressure consistent with the analysis of variance. The predicted substrate temperature is given by:

$$\text{Predicted Substrate Temperature (C)} = 295.2 + 90.8 * \text{Incident Power (kW)} + 2.07 * \text{Pressure (Torr)} \pm 17.2.$$

The coefficient of determination for this model is 0.771. Figure 5.4 shows the predicted substrate temperature versus observed substrate temperature and Figure 5.5 shows the predicted substrate temperature versus incident microwave power. In Figure 5.4 the straight line represents perfect agreement between predicted substrate temperature and observed substrate temperature.

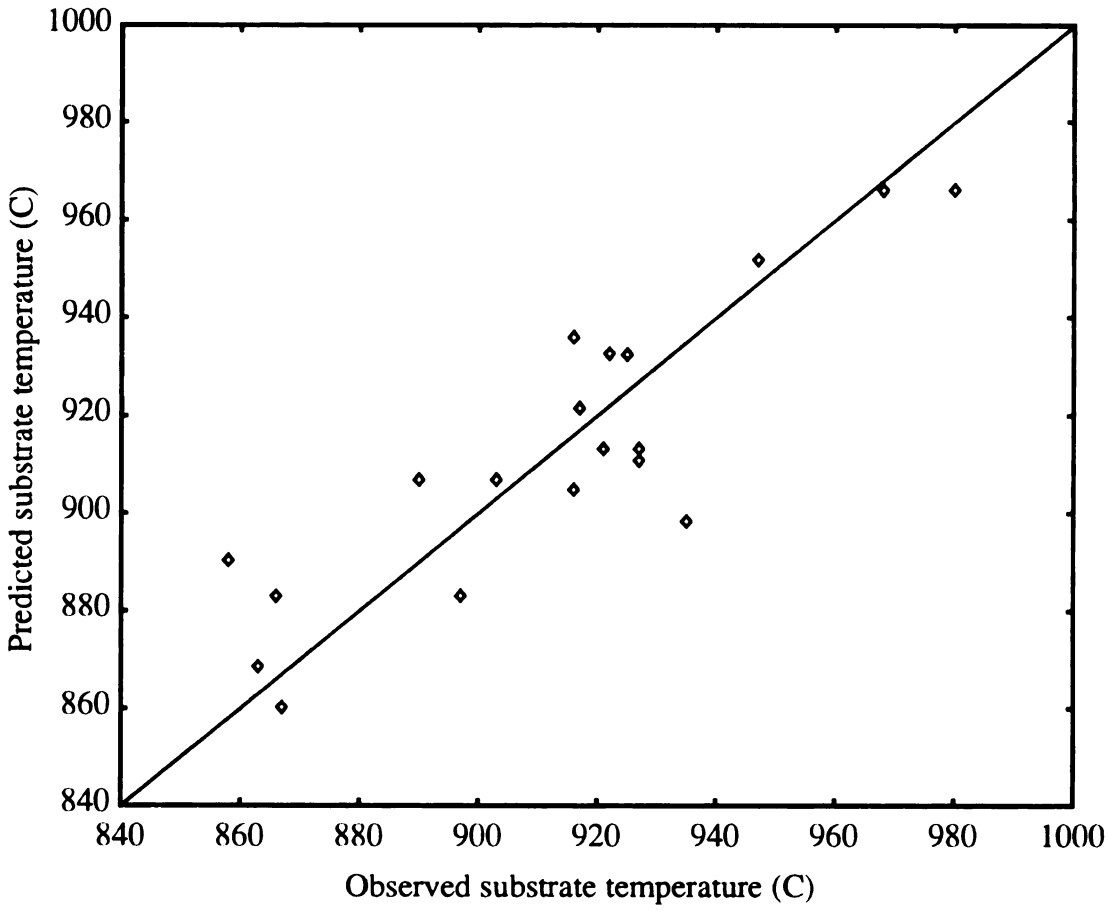

Figure 5.4: Scatterplot of predicted substrate temperature versus observed substrate temperature for the high pressure diamond deposition reactor. Straight line represents perfect agreement between predicted values and observed values.

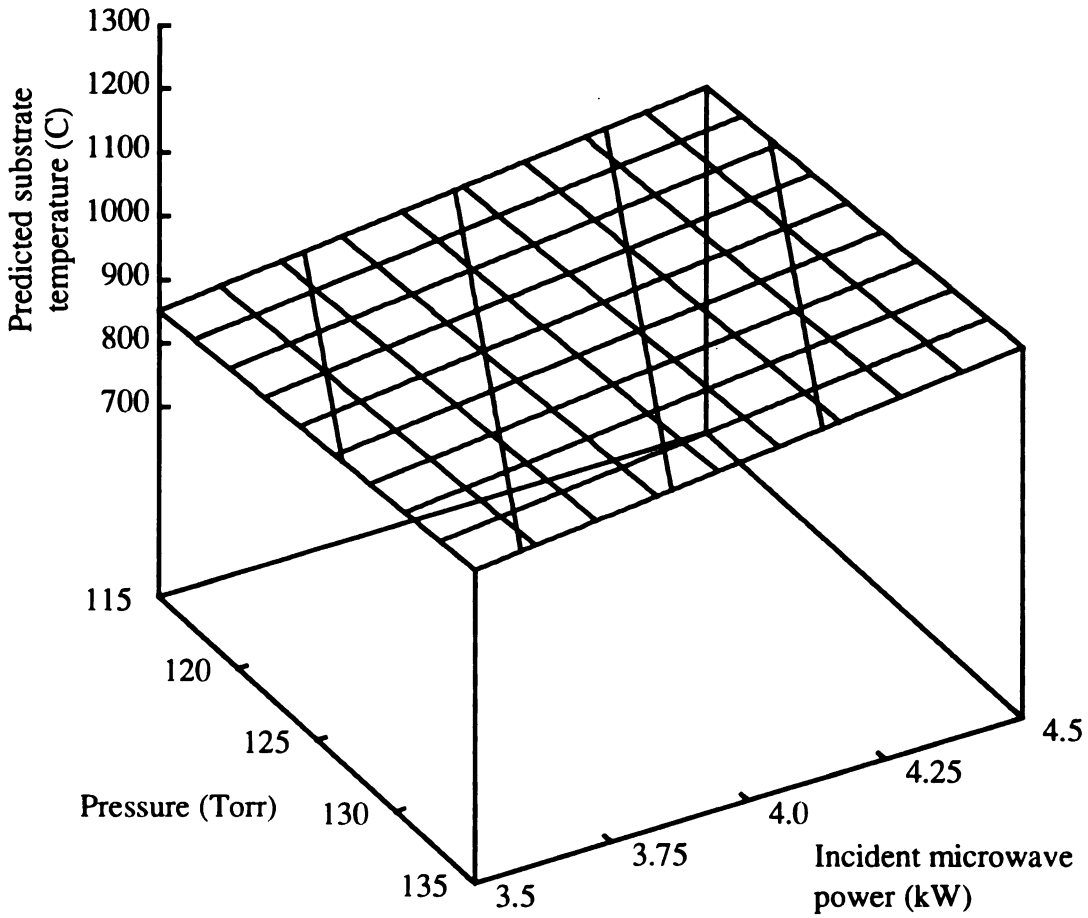

Figure 5.5: Predicted substrate temperature for the high pressure diamond deposition reactor versus pressure and incident microwave power. Contours at 875, 900, 925, and 950 C.

5.2 Low pressure hydrogen discharge diagnostics

Species temperature measurements were performed using optical emission spectroscopy on a hydrogen discharge at a range of pressures between 0.1 and 0.4 Torr. Again, the experiments were statistically designed in order to gain the most information about the discharge while minimizing the experimental costs. The 2^3 factorial design included the pressure, microwave power and hydrogen flow factors at two levels. Two star points for each factor and a center point were chosen consistent with the previous diagnostic experiments. The details of the experimental parameters and the results of the hydrogen temperature measurements are included in Table for the pressure range 0.1 - 0.4 Torr, the microwave power range of 150 - 300 Watts and the hydrogen flow range of 19.2 - 50 sccm.

5.2.1 Hydrogen translational temperature (low pressure discharge)

The hydrogen translational temperature for the low pressure pure hydrogen discharge was determined for each of the nineteen experiments in Table 5.4 using the same techniques described in Section 4.2.1. The analysis of variance for the hydrogen translational temperature is presented in Table 5.5. The ANOVA indicates incident power and pressure are significant effects at a significance level of $\alpha = 0.17$ or less. The least square fits showed the hydrogen translational temperature varies linearly with incident power and pressure. Figure 5.6 shows a sample least square fit of hydrogen translational temperature versus incident microwave power at the star and center points.

The least squares regression yielded a model for the variation of hydrogen translational temperature shown in Figure 5.7. The model with an R^2 of 0.659 and $SSR = 45973$ is:

Table 5.4 Statistically designed experiments for the low pressure hydrogen discharge.

Run #	Incident Microwave Power (W)	Pressure (Torr)	Hydrogen Flow (sccm)	Hydrogen Translational Temperature (K)	Hydrogen Electronic Temperature (K)	
1	225	0.25	34.6	1398	2484	Center
2	225	0.25	34.6	1426	2446	Center
3	225	0.25	34.6	1410	2504	Center
4	225	0.25	34.6	1414	2426	Center
5	225	0.25	34.6	1402	2432	Center
6	175	0.15	23.1	1447	2498	Factor
7	175	0.15	46.2	1462	2408	Factor
8	175	0.35	23.1	1477	2486	Factor
9	175	0.35	46.2	1492	2273	Factor
10	275	0.15	23.1	1493	2910	Factor
11	275	0.15	46.2	1501	2805	Factor
12	275	0.35	23.1	1515	2525	Factor
13	275	0.35	46.2	1508	2390	Factor
14	150	0.25	34.6	1298	2072	Star
15	300	0.25	34.6	1612	2862	Star
16	225	0.10	34.6	1380	3041	Star
17	225	0.40	34.6	1497	2345	Star
18	225	0.25	19.2	1419	2429	Star
19	225	0.25	50.0	1423	2465	Star
			SSE =	480	4635	

Predicted Hydrogen Translational Temperature (K) = 1179.2 + 0.974 * Incident Power (W) + 211.2 * Pressure (Torr) ± 53.6.

The scatterplot of predicted hydrogen translational temperature against the observed temperature is shown in Figure 5.8. The standard deviation for the model is 53.6 K and the residual error is due to lack of fit with a significance level of $\alpha = 0.01$ over experimental error.

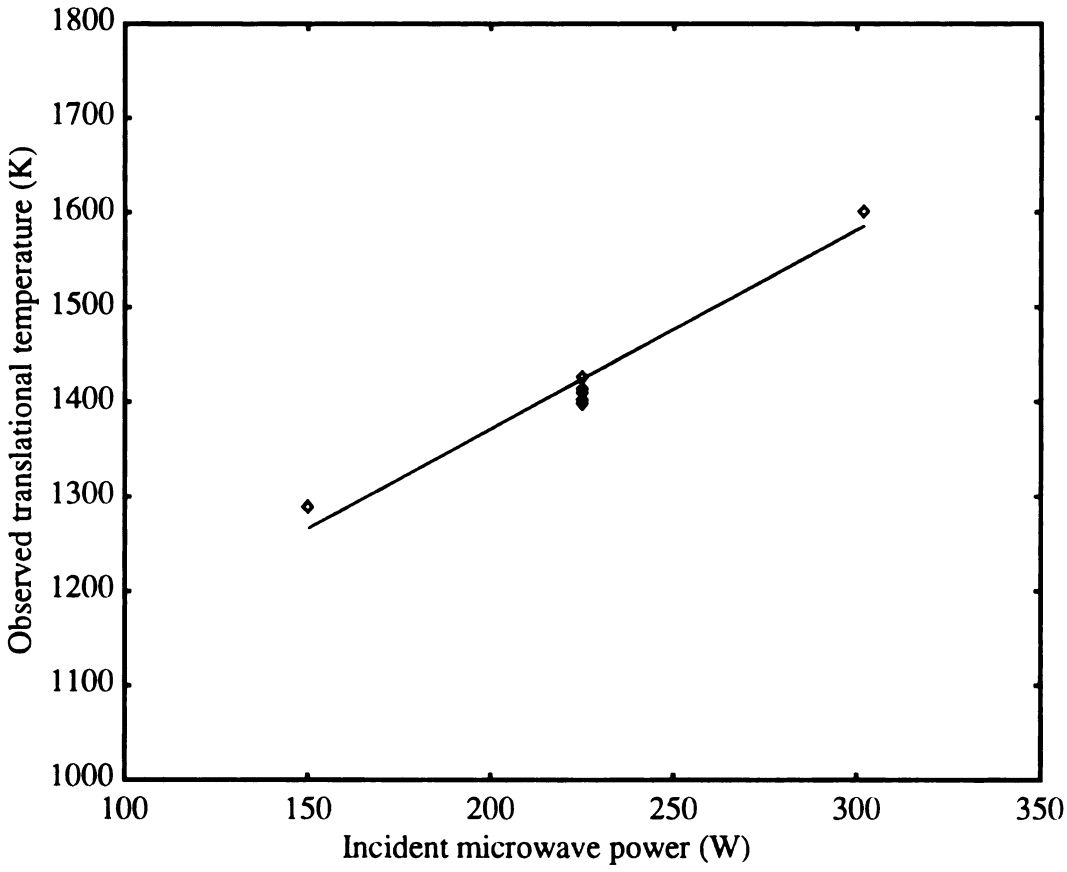

Figure 5.6: Least squares fit of hydrogen translational temperature to incident microwave power for a low pressure hydrogen discharge. Pressure = 0.25 Torr and hydrogen flow = 34.6 sccm.

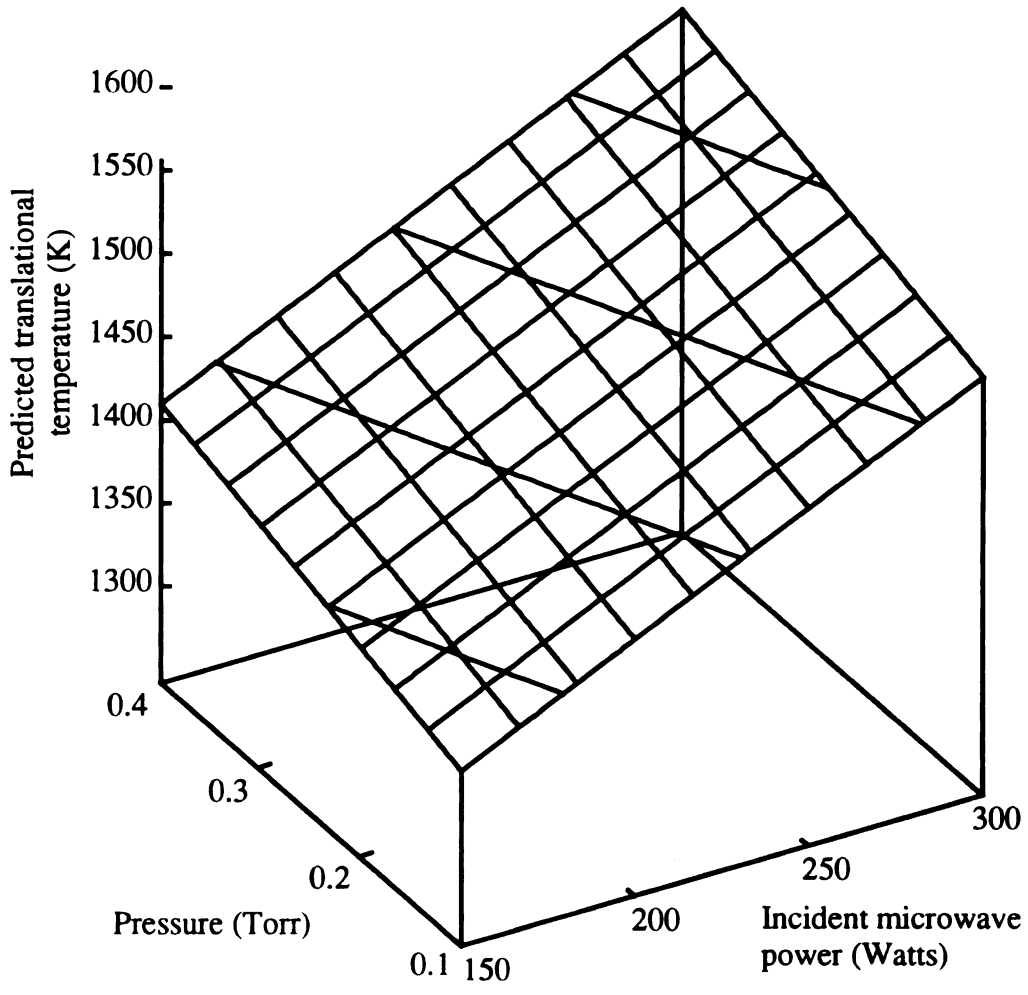

Figure 5.7: Predicted hydrogen translational temperature for a low pressure hydrogen discharge. Contours at 1375, 1425, 1475, 1525 K.

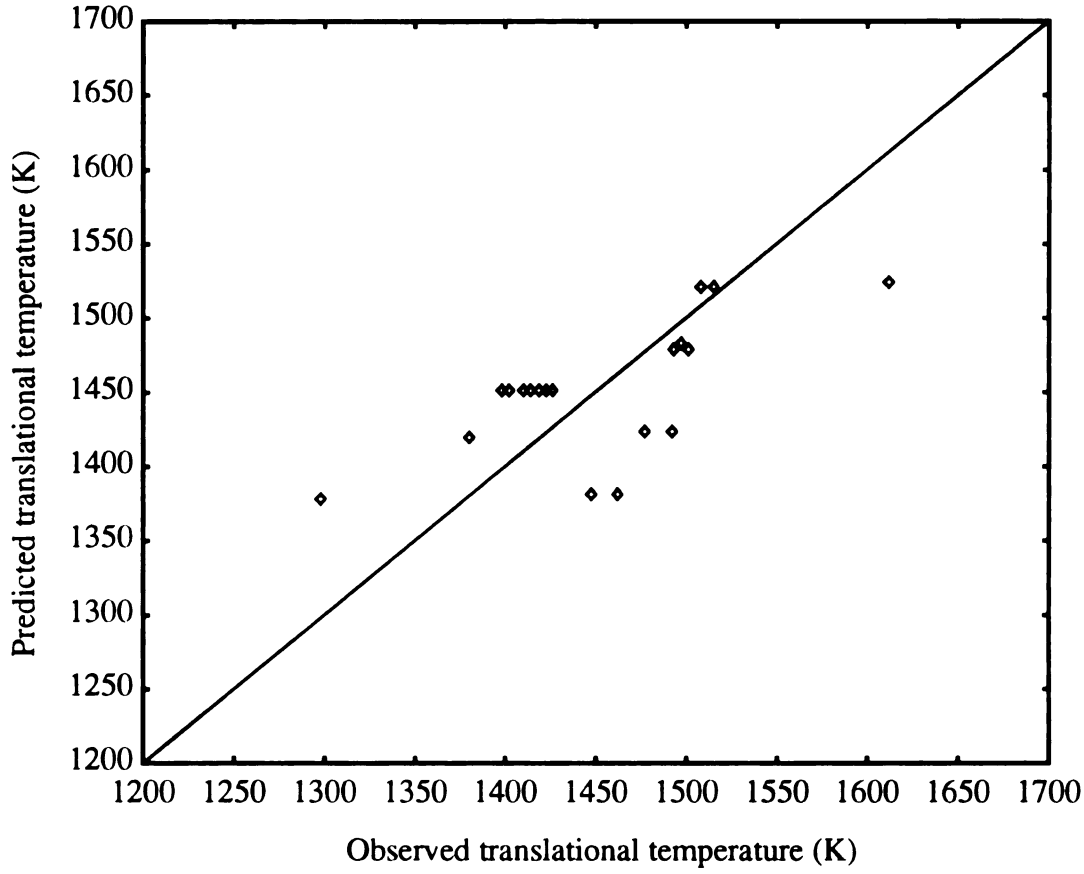

Figure 5.8: Scatterplot of predicted hydrogen translational temperature versus observed translational temperature for a low pressure hydrogen discharge. The straight line represents perfect agreement between observed and predicted values.

Table 5.5 ANOVA of translational and electronic temperatures for the low pressure discharge.

	Hydrogen Translational Temperature			Hydrogen Electronic Temperature		
	Mean Square	**DF**	**α**	**Mean Square**	**DF**	**α**
Pressure	979.0	1	0.017	112101.1	1	0.062
Incident Power	2397.8	1	0.003	16403.1	1	0.061
Power X Pressure				53301.1	1	0.090
Error	78.1	5		1081.12	4	

5.2.2 Hydrogen electronic temperature (low pressure discharge)

The hydrogen electronic temperature was determined for the low pressure hydrogen discharge using the same technique described in Section 4.2.2. The data is presented in Table 5.4 for the nineteen statistically designed experiments. The final analysis of variance, shown in Table 5.5, indicates that pressure, incident power as well as their interaction have a significant effect on hydrogen electronic temperature at a significance level of $\alpha = 0.09$ or less.

The least squares regression of hydrogen electronic temperature to incident power for the star and center points of Table 5.4 show a linear fit. The same fit to pressure though, shows some nonlinearity. Figure 5.9 shows the fit of temperature to pressure for the star and center points. The regression of the entire nineteen data points therefore included the two significant main effects, pressure and power, as well as a pressure by pressure term and the pressure by power interaction. The model, with $R^2 = 0.851$, is:

Predicted Electronic Temperature (K) = 1767.0 + 7.52 * Incident Power (W) - 2795.2 * Pressure (Torr) + 9751.0 * [Pressure (Torr)]^2 - 16.32 * Pressure (Torr) * Incident Power (W) ± 101.9.

The scatterplot of predicted hydrogen electronic temperature versus observed temperature is shown in Figure 5.10 and the model is plotted in Figure 5.11.

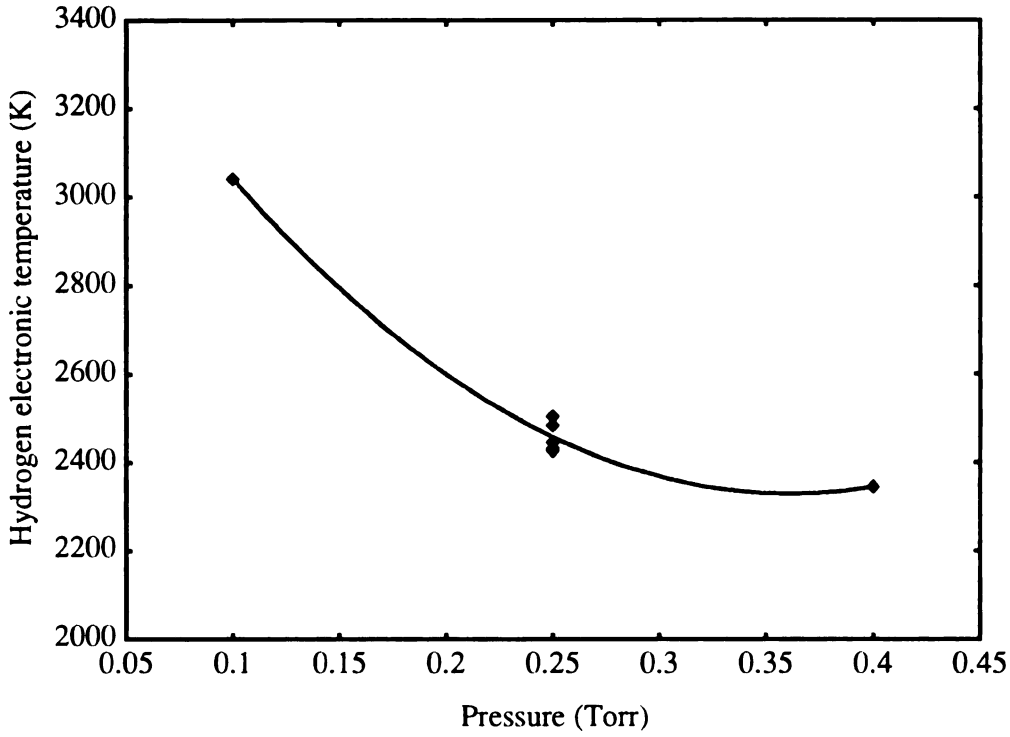

Figure 5.9: Least squares fit of hydrogen electronic temperature to pressure for a low pressure hydrogen discharge. Incident microwave power = 225 Watts and hydrogen flow = 34.6 sccm.

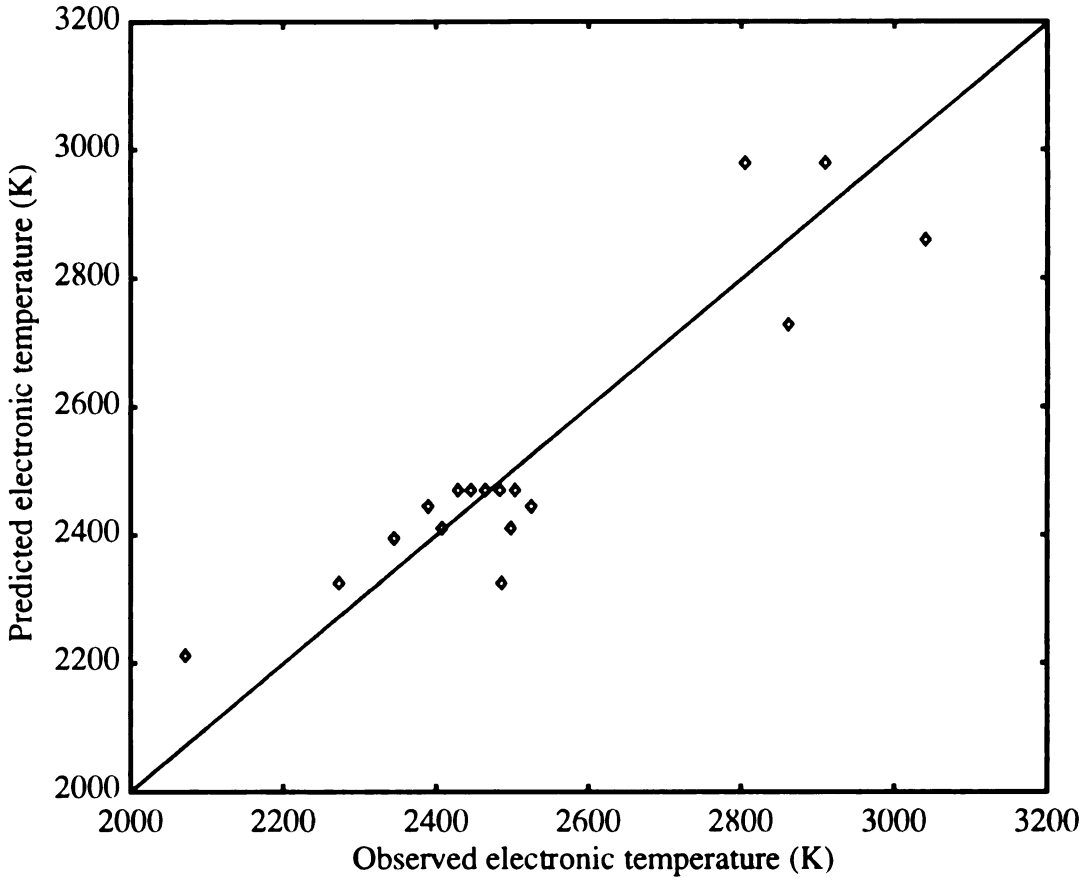

Figure 5.10: Scatterplot of predicted hydrogen electronic temperature versus observed electronic temperature for a low pressure hydrogen discharge. The straight line represents perfect agreement between observed and predicted values.

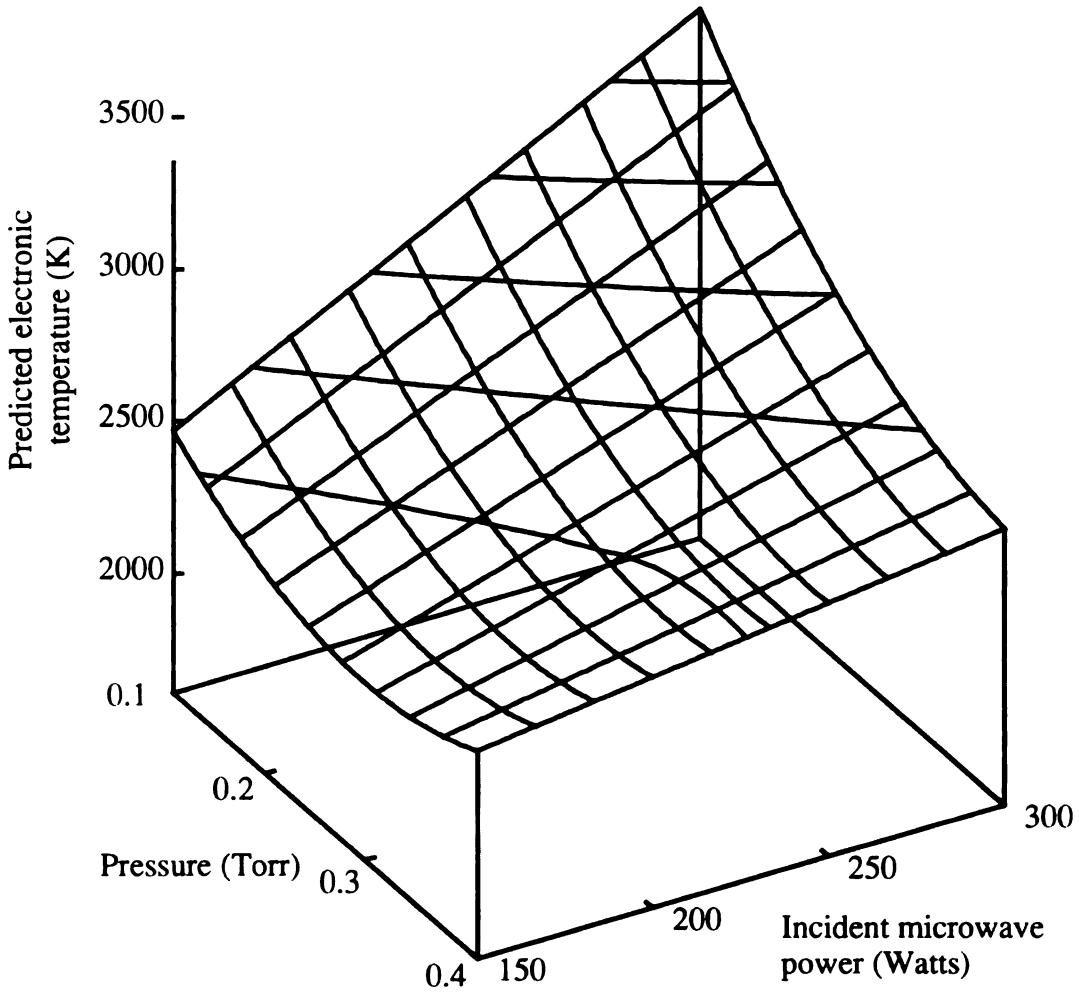

Figure 5.11: Predicted hydrogen electronic temperature for a low pressure hydrogen discharge. Contours at 2400, 2600, 2800, 3000, 3200 K.

5.3 Comparison of diamond deposition reactor temperatures

The hydrogen translational and electronic temperatures for the diamond deposition reactor studied in Chapter 4 and the hydrogen translational temperatures for the high pressure diamond deposition reactor are plotted versus pressure in Figure 5.12. In the lower pressure region the electronic temperature is decreasing with increasing pressure while the translational temperature is increasing with increasing pressure. As mentioned above, the high pressure temperatures are statistically invariant to pressure changes. Furthermore, the mean temperatures, translational, electronic and rotational, converge to values close to 2000 K. At the higher pressures, the discharge is coming to an equilibrium in temperature.

As discussed in Section 4.1, the input microwave energy is constantly perturbing the system. In the lower pressure regime the microwave energy perturbs the equilibrium between the various species temperature degrees of freedom. Microwave energy is coupled to the electron subgas in the discharge which in turn is coupled to the atomic hydrogen through excitation collisions. The electronic temperature of the hydrogen atom is, therefore, relatively high. The translational temperature, the kinetic energy of the atom, is relatively low. The relative atomic hydrogen concentration is increasing as pressure increases (Section 4.3.4); therefore, some of the energy is being coupled through dissociative collisions as well.

At the high pressure regime, the microwave energy is still being coupled to the electron gas but the plasma is more collisional and therefore the atomic hydrogen and the rotational temperatures are close to equilibrium. This suggests the energy is then being coupled to some other process in the discharge rather than perturbing this equilibrium. One possibility is more energy is being utilized by thermal dissociation or reaction rather than electron collisional processes.

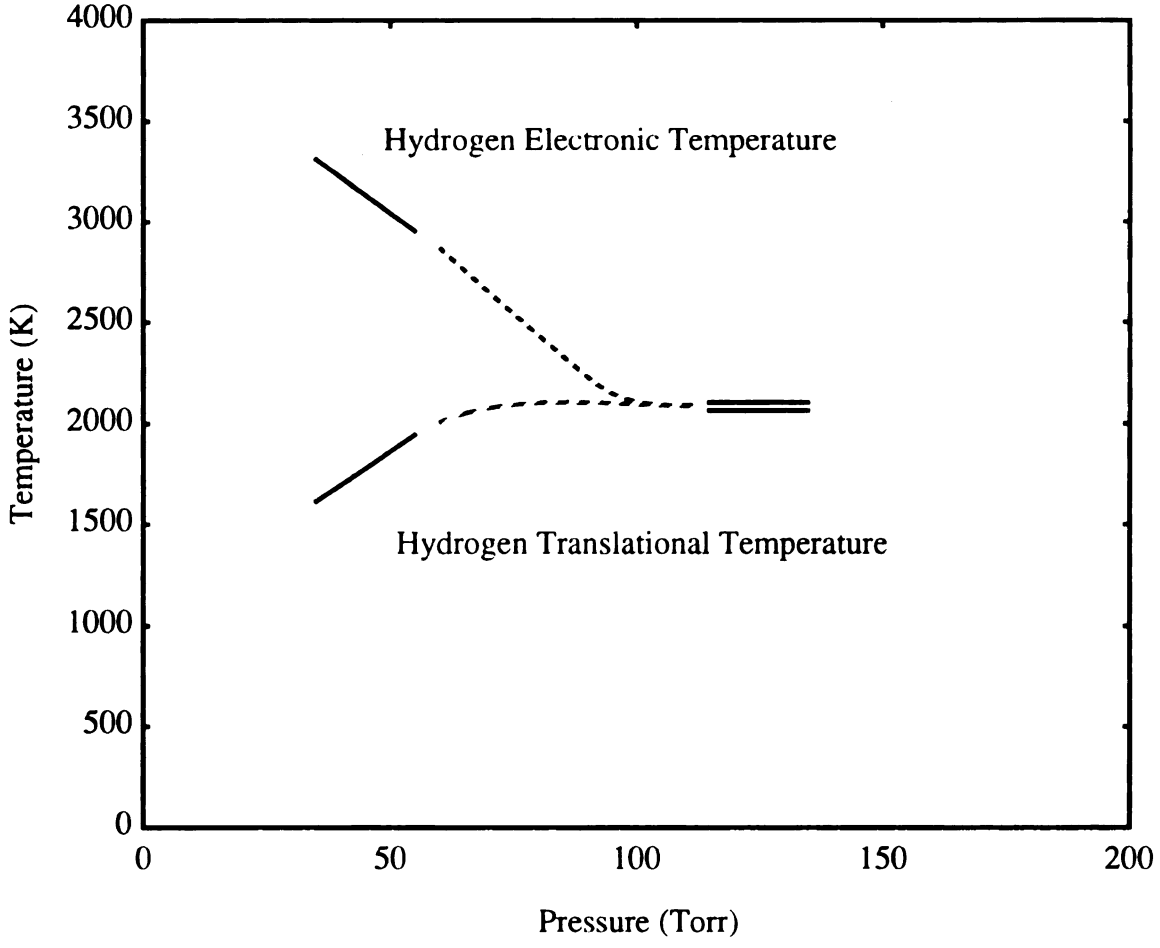

Figure 5.12: Comparison of hydrogen atomic temperatures for the diamond deposition reactor and the high pressure diamond deposition reactor. Incident microwave power = 2.16 kW and hydrogen flow = 400 sccm for the diamond deposition reactor results. The high pressure results are valid for the power and flow ranges studied.

Chapter 6

Argon/Sulfur Hexafluoride Discharge Diagnostics

6.0 Introduction to silicon etching ECR discharges

This chapter introduces the specific equipment used to carry out the diagnostic experiments on the argon/SF_6 silicon etching discharge and then describes the experiments themselves. The first sections detail the theory, the lasers, optics and signal collection equipment used for the laser induced fluorescence (LIF) work. Next, the neutral species temperature measurements are described. Finally, the statistically designed experiments performed on the ECR discharge are detailed and the statistical models describing its behavior are presented.

6.1 Laser induced fluorescence theory

LIF involves exciting an atom, ion, or molecule to a higher electronic, rotational or vibrational energy level through absorption of laser radiation. The excited species can spontaneously decay to a lower energy level through the emission of a photon [89]. The intensity of this emission (fluorescence) is proportional to the density of the species in the excited state and indirectly proportional to the density of species in the original energy level [90].

The Doppler effect, where the relative motion of a particle shifts the observed frequency of light emitted or the light absorbed by that particle, serves as the basis for the ion velocity distribution measurements using LIF. By tuning the laser's wavelength through the Doppler shifted absorption wavelengths, the resulting lineshape of the fluorescence

intensity is proportional to the ion velocity distribution along the laser beam. If $I(\lambda)$ is the intensity of the fluorescence at a wavelength, λ, then

$$I(\lambda)\,d\lambda = Kf(v)\,dv \tag{6.1}$$

where $f(v)$ is the distribution of the species at velocity, v, and K is a proportionality constant. The relationship of λ to v is dictated by the Doppler effect as:

$$\frac{1}{\lambda} = \frac{1}{\lambda_o}\left(1 + \frac{v}{c}\right) \tag{6.2}$$

where λ_o is the wavelength of transition when the species is at rest, c is the speed of light in vacuum. Using Equations 6.1 and 6.2, the intensity of the fluorescence of a particular transition can be related to the velocity distribution of the species.

6.2 Species energy measurements using LIF

If the ion velocity distribution is assumed to be Maxwellian at a temperature T, as discussed in Section 6.1, the intensity distribution (lineshape) due to Doppler broadening has a Gaussian shape [82]:

$$g_{dop}(\lambda - \lambda_o) = \sqrt{\frac{m_i c^2}{2\pi k T \lambda_o^2}}\, exp\left(-\frac{m_i c^2}{2kT\lambda_o^2}(\lambda - \lambda_o)\right) \tag{6.3}$$

where m_i is the mass of the fluorescing species, k is Boltzmann constant. The full width at high maximum (FWHM) of this distribution is:

$$\Delta\lambda = \frac{2\lambda_o}{c}\sqrt{\frac{2kT(ln2)}{m_i}} \tag{6.4}$$

Therefore the energy of the of the species found by measuring the FWHM ($\Delta\lambda$) of a purely Doppler broadened intensity distribution and solving for T is:

$$T = \frac{mc^2}{8k\,(ln2)}\left(\frac{\Delta\lambda}{\lambda_o}\right)^2 \qquad \text{K} \tag{6.5}$$

6.3 The lasers

A number of different lasers could be chosen for LIF work each having distinct advantages. The laser chosen, though, must have high peak power, a narrow spectral width and be frequency tunable. The work presented in this thesis uses a tunable dye laser pumped by a Nd:YAG pulsed laser. The complete LIF apparatus is shown schematically in Figure 6.1.

6.3.1 Nd:YAG pulsed laser

In order to adequately pump the dye laser and increase the signal to noise ratio by minimizing the loss of excited species due to quenching, saturation of the laser induced absorption transition should be assured. One way to saturate this transition is through the use of a high power laser. The necessary high power is achieved with a Q-switched neodymium doped yttrium aluminum garnet (Nd:YAG) pulsed laser (Spectra-Physics DCR-11). The peak power of 40 MWatts with a pulse duration of 6 nsec assures adequate pumping of the lossy tunable dye laser after frequency doubling to facilitate saturation of the absorption transition.

The laser output of the pump laser is frequency doubled using an harmonic generator (Spectra-Physics HG-2). The harmonic generator consists of a KD*P crystal (potassium dideuterium phosphate) which interacts with the fundamental 1064 nm light from the Nd:YAG laser to produce a secondary wave with half the wavelength. Since the conver-

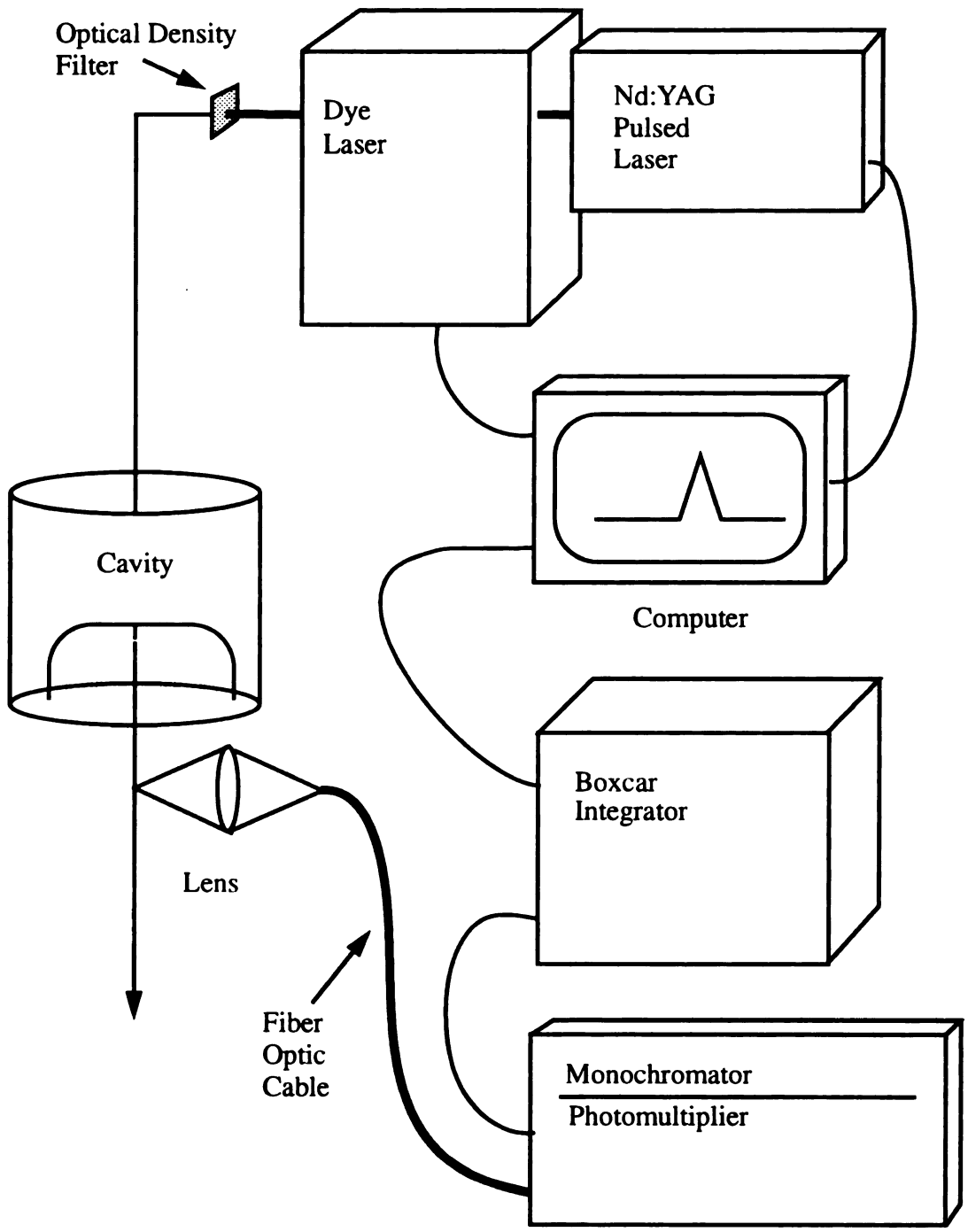

Figure 6.1: The laser system and light collection equipment.

sion efficiency of the crystal is highly dependent on its temperature, a temperature controller is necessary for optimum frequency conversion.

6.3.2 Dye laser

Since many suitable transitions exist and many different gases can be used, a tunable laser is necessary to fully analyze any plasma system. The dye laser as used in this work (Spectra-Physics PDL-3) provides tunable laser radiation from 190 nm to 960 nm. The particular range of laser radiation available depends on the dye used. In order to scan the entire velocity distribution of the particular argon species studied here (624.3 nm), Exciton DCM dye was chosen. The dye was prepared to maximize the laser power output near 624.3 nm. Following the recommendations of the dye manufacturer and the laser manufacturer, the DCM dye powder was diluted in HPLC grade methanol.

In addition to the dye, the angle of the wavelength tuning grating is adjustable to permit spectral tuning of the output radiation. Control of the grating angle is achieved through the use of a stepper motor and stepper motor controller. A personal computer is used to coordinate the motor, the light collection stages and the gated integrator.

6.4 Fluoresced light collection

Laser access to the plasma is achieved as described in Chapter 3. This section will describe the collection of the fluoresced light and the apparatus necessary for spatial characterization of the ion species.

6.4.1 Optics

Emitted light is collected by a lens of diameter 6.3 cm and focal length 5 cm. The light is focused onto a 1 mm diameter fiber cable which carries the light out of the vacuum system to the monochromator. The imaging system just described is shown in Figure 6.2 along with the translation stages necessary to move the focal point within the vacuum.

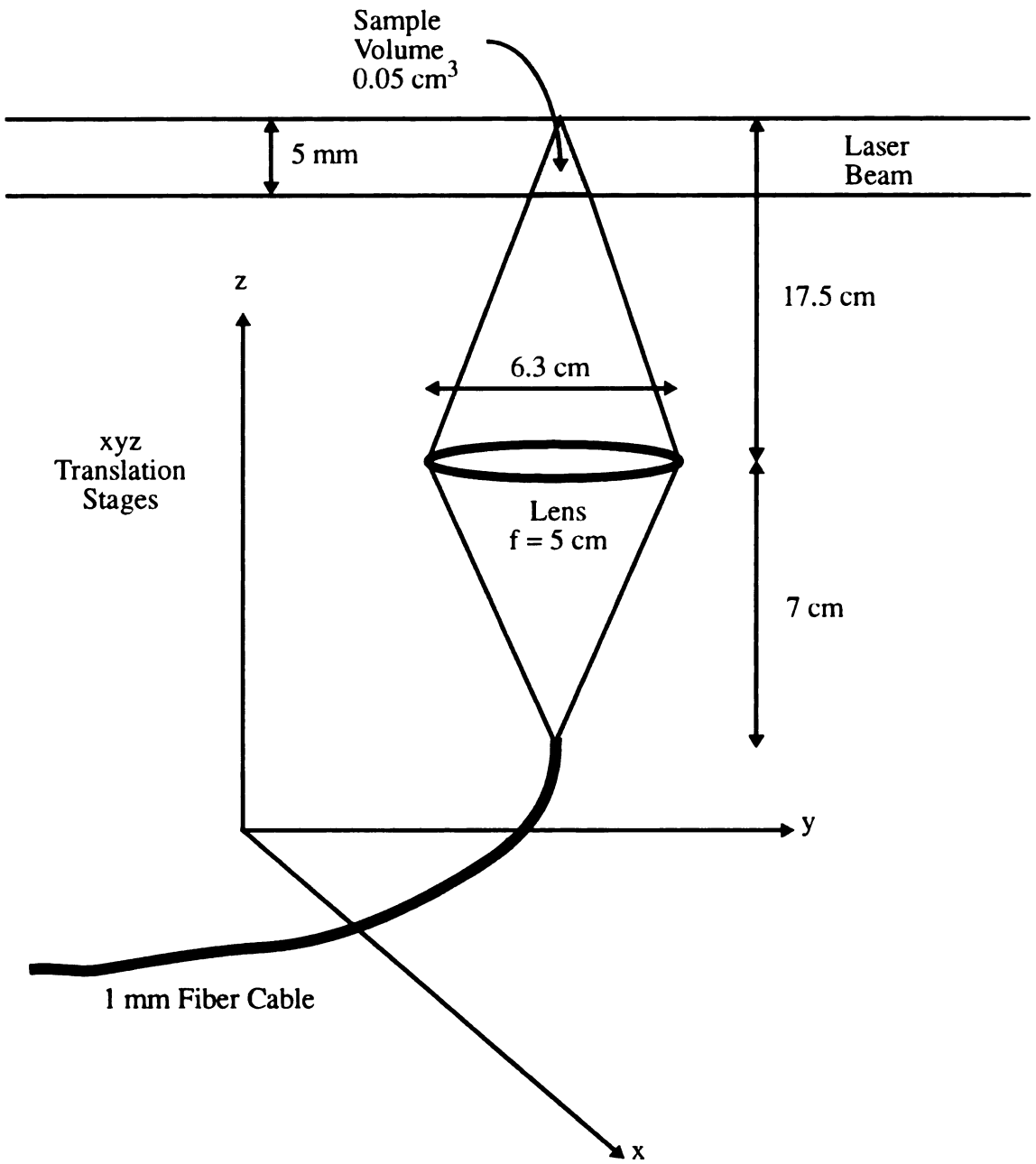

Figure 6.2: Optics used and spatial resolution achieved for the LIF experiments.

Three dimensional movement is available with the three translation stages; they allow precise positioning of the collection volume along the laser beam. The x and y stages allow movement along a distance of 4 inches and the z stage allows movement along 2 inches.

Figure 6.2 also shows the actual spatial dimensions of the collection volume and gives an estimate of the spatial resolution of the system as used in this work. The sample volume is 0.05 cm^3 in this configuration. Using a calculation of the solid angle subtended by the optics and assuming fluorescence occurs isotropically, about 1% of all photons emitted are collected by the lens.

6.4.2 Monochromator

A 1 meter, f/9, Spex, Inc. monochromator is used to filter unwanted light from the fluorescence signal. In addition, an optical filter with a passband centered near the fluoresced light wavelength is used to further reduce the amount of unwanted light affecting the signal. The light from the monochromator is detected using an EMI, Inc. cooled photomultiplier. The monochromator entrance and exit slits are set at 1 mm to ensure good signal to noise ratio. Since the spectral resolution of the apparatus is determined by the laser linewidth and other broadening mechanisms the spectral width of the monochromator is not a factor.

6.4.3 Gated integrator

A gated or boxcar integrator (EG&G PARC 4121B) is used to repetitively sample the fluorescence signal emanating from the photomultiplier. The integrator samples the photomultiplier signal when triggered by the pump laser. The samples are averaged to improve the signal to noise ratio (SNR). The averaged signal is converted to a digital signal to allow data collection by computer using an A/D converter (EG&G PARC 4161A). A preamplifier is in place between the photomultiplier tube (PMT) and the gated integrator. The amplifier with a gain of 125 is DC coupled to the gated integrator.

The important aspect of the gated integrator set-up is the timing of the trigger with respect to the laser pulse. In order to minimize any stray laser light from artificially enhancing the fluorescence signal, the integrator is timed to collect fluoresced light immediately after the end of the laser pulse. Figure 6.3 shows a timing diagram where the laser pulse, trigger pulse, fluorescence pulse and the open gate of the integrator are shown. Two timing adjustments are possible. The delay between the actual laser pulse and the start of the trigger pulse is adjustable (shown in Figure 6.3). Also, a more sensitive adjustment is available on the gated integrator which allows control of the delay between the time the gated integrator receives the trigger and the start of the gate (Gate Delay in Figure 6.3). In this work, a gate of 30 nsec with 30 samples averaged using an input signal sensitivity of 200 mV is found to give the best signal strength without serious SNR problems and is used for most of the measurements.

6.4.4 Computer Control

The entire experiment is controlled through the use of an IBM PC computer with various interface boards. LIF signals are determined by first pulsing the laser for a prescribed number of seconds and simultaneously collecting the gated integrator signals. Then the measuring process is repeated for the same length of time with no laser pulses. By comparing the gated integrator signals when the laser is pulsing to the background signals when the laser is off, the LIF signal strength is determined. Generally, at each wavelength point the intensity shown is an average of 7 to 13 on-off cycles where each cycle is about 18 sec each.

The computer also controls the dye laser grating through the stepper motor and stepper motor controller. Additionally, movement of the collection optics is achieved through control of the translation stages within the vacuum chamber. The complete QuickBasic program used for computer control is included in reference [90].

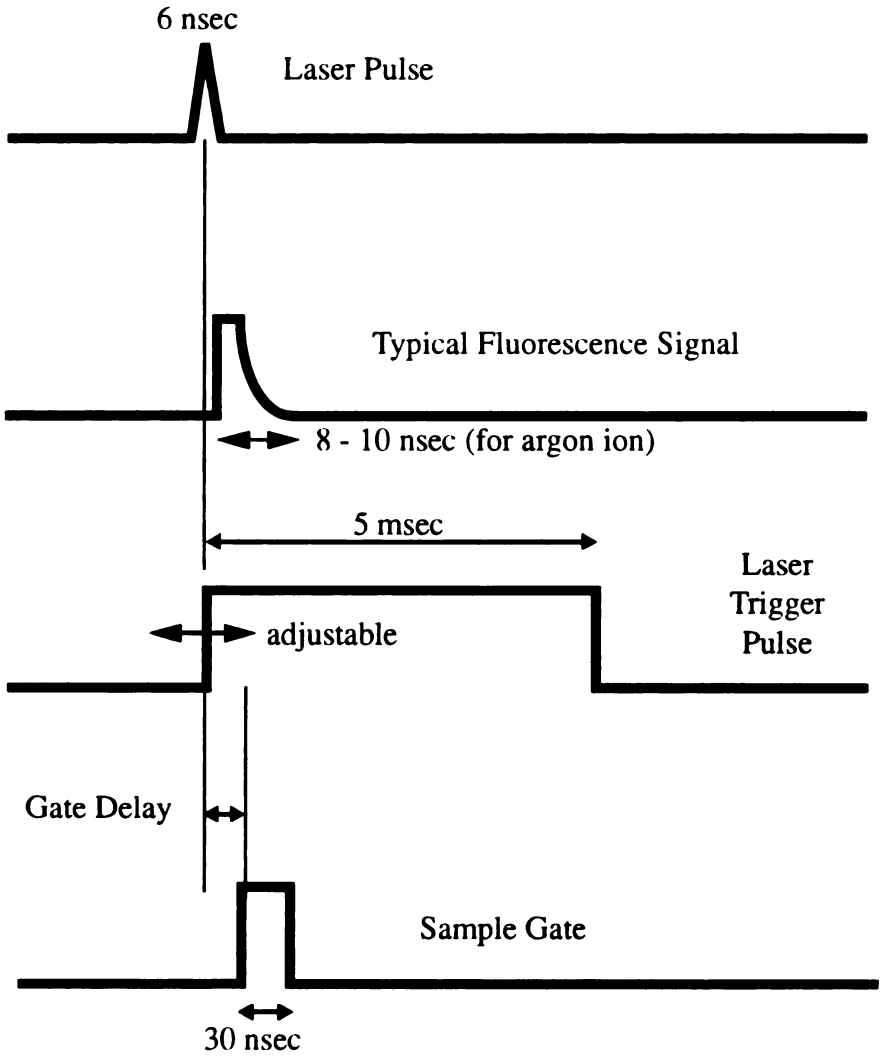

Figure 6.3: Timing diagram for triggering the gated integrator.

6.5 Introduction to velocity distribution measurements

The implemented LIF system has been used to study the ion energies and velocities in a multipolar ECR plasma source. The plasma source has been split into two distinct regions. The source is that region within the discharge chamber where the plasma is generated and electromagnetic energy is coupled to the electron gas by the electric fields of the microwave cavity and the ECR static magnetic fields. The processing region lies below the source and is where the ion energy and velocity distributions are dominated by plasma potential gradients and diffusion processes from the source to the processing regions [94].

Since the ion energy and velocity distribution along the laser direction is measured, changing the direction of the laser provides information on the distributions both horizontally, with a radial laser beam, and vertically, with a longitudinal laser beam as shown in Figure 6.4. Ion energy distributions are measured in both regions and, within the source region, in both directions. Ion velocity distributions are particularly interesting when comparing one position with another and therefore they are presented in that context.

The experiments described here examine the properties of a singly ionized argon metastable in the ECR plasma. Specifically, the absorption transition of this metastable ion is the $3d^4F_{7/2}$- $4p^2D_{5/2}$ transition at 624.3 nm. The emission is the $4p^2D_{5/2}$ - $4s^2P_{3/2}$ transition at 488.0 nm.

6.5.1 Spectral line broadening

A typical ion energy distribution, measured at the center of the source region (r=0, z=1: Figure 6.4), is shown in Figure 6.5 where fluorescence intensity in arbitrary units (arbs) is measured versus radial ion velocity. An obvious feature of this distribution is that it has a certain non-zero width. A number of factors contribute to the broadening of the distribution, including Doppler shifts, high laser power, laser spectral width, magnetic

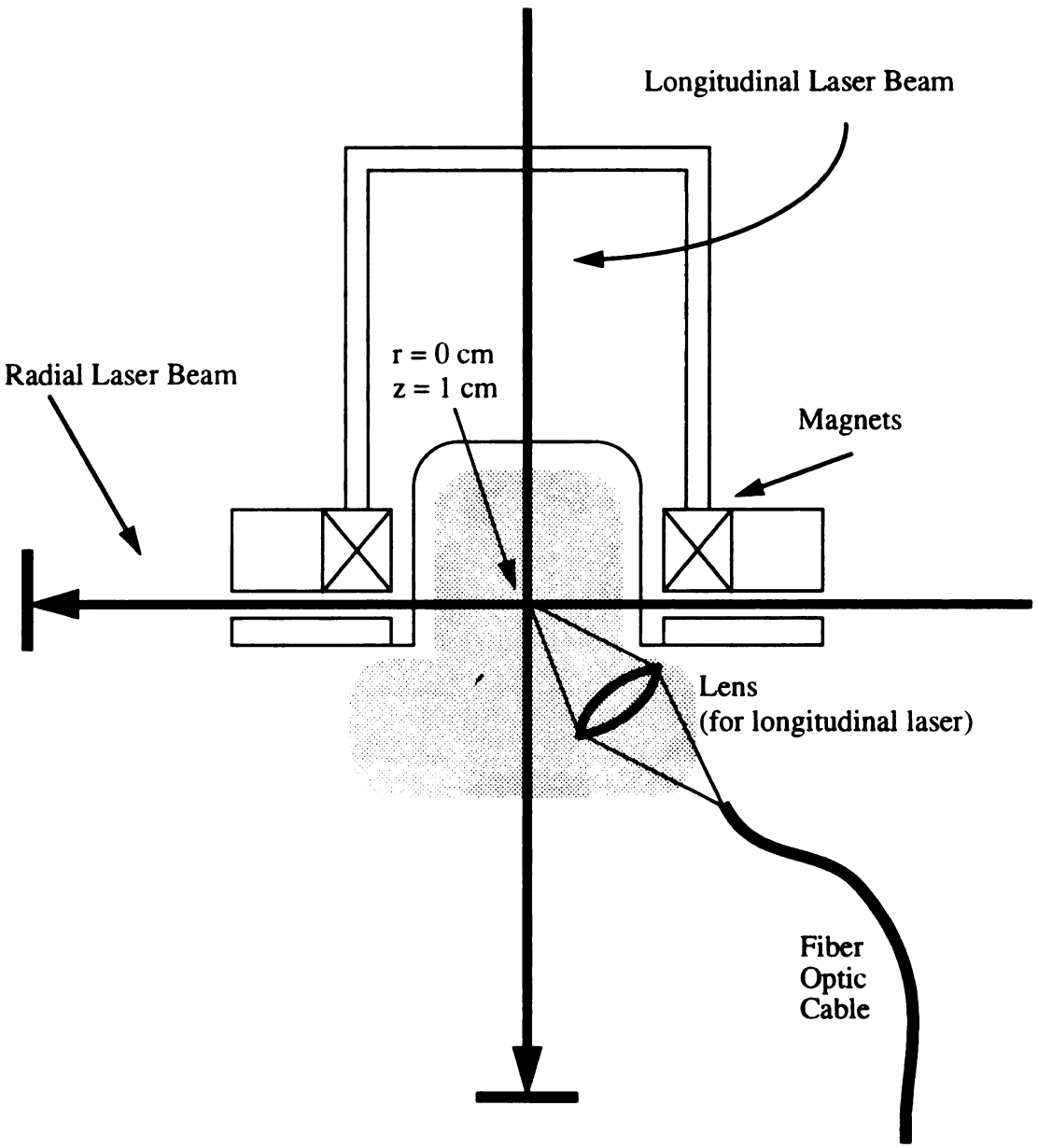

Figure 6.4: Longitudinal and radial laser beams and longitudinal light collection.

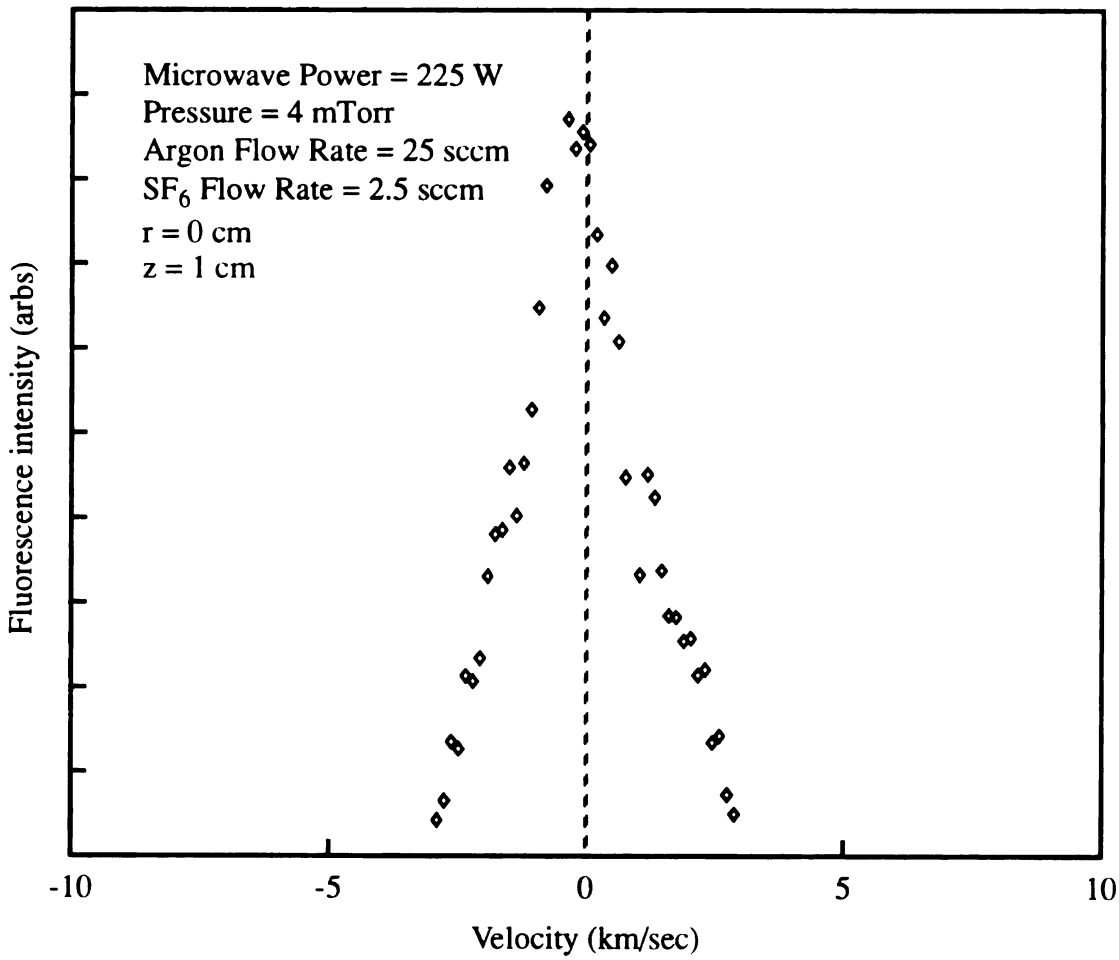

Figure 6.5: Radial ion energy distribution.

fields and electric fields. Therefore, care must be taken in interpreting the results in terms of the energy of the ion.

6.5.2 Doppler broadening

Doppler shifted broadening (Section 6.2) occurs due to the relative motion of the ion with the observer. From an assumed Gaussian distribution a full width at half maximum is found which relates the average ion energy or temperature to the observed distribution (Equation 6.4). This is an actual temperature only in the absence of all other broadening mechanisms.

6.5.3 Laser broadening

Laser broadening occurs due to the non-zero linewidth of the laser light. Since the laser light is Gaussian and a Doppler-broadened line takes a Gaussian shape then the two can be deconvolved by:

$$\Delta\lambda_{dop} \approx \sqrt{\left(\Delta\lambda_{obs}\right)^2 - \left(\Delta\lambda_{las}\right)^2} \tag{6.6}$$

where $\Delta\lambda_{dop}$ is the Doppler broadened FWHM, $\Delta\lambda_{obs}$ is the FWHM of the observed line and $\Delta\lambda_{las}$ is the linewidth of the laser. Equation 6.6 is used to extract a Doppler broadened linewidth from the observed line when all other broadening mechanisms are minimized. For the Spectra-Physics laser used in these experiments and described in Section 6.3.1, the linewidth of the laser is given by the manufacturer as 0.07 cm^{-1}.

6.5.4 Zeeman splitting

Zeeman splitting is the effect of magnetic fields on the observed distribution. It is not broadening in the sense of Doppler broadening but actually arises as the splitting of the spectral absorption energy into two or more distinct energies. For most of the locations

inside the plasma region measured in this thesis, the magnetic fields are negligible and Zeeman splitting can be ignored. Reference [29] shows that the magnetic fields in most of the sample areas are negligible, particularly at the center of the source and processing regions.

6.5.5 Saturation Broadening

Line broadening due to a high intensity laser with a finite bandwidth is termed saturation broadening [91]. The pulsed laser used in these experiments operates at a power density such that saturation broadening is observed. In order to reduce the effect of saturation broadening, the laser intensity is attenuated using a series of optical density filters.

The saturation broadening effect can be understood by considering the nonlinearity of the LIF process [92]. Consider a laser at one single wavelength; an increase in laser intensity would results in a corresponding increase in fluorescence signal until saturation occurs. Saturation is when all the ions available have made the laser induced transition. At this point the fluorescence signal levels out, no longer increasing linearly. Note, though, since the laser does not have a finite bandwidth, photons other than those at the peak may have enough energy to saturate the transition also. This is sketched in Figure 6.6. As the peak laser intensity is tuned away from the absorption transition, saturation is still possible and the fluorescence signal with respect to the laser wavelength will be broadened.

The saturation broadening effect in the multipolar ECR reactor was experimentally determined by taking a series of measurements with increasing attenuation of the beam. As the attenuation increases the broadening of the line decreases until the saturation broadening is minimized. Unfortunately, the fluorescence signal intensity also decreases as the intensity of the laser is decreased so a compromise is made between saturation broadening and signal strength. The beam was attenuated using a series of optical density filters placed in the path of the laser (Figure 6.2). The radial ion energy measurements

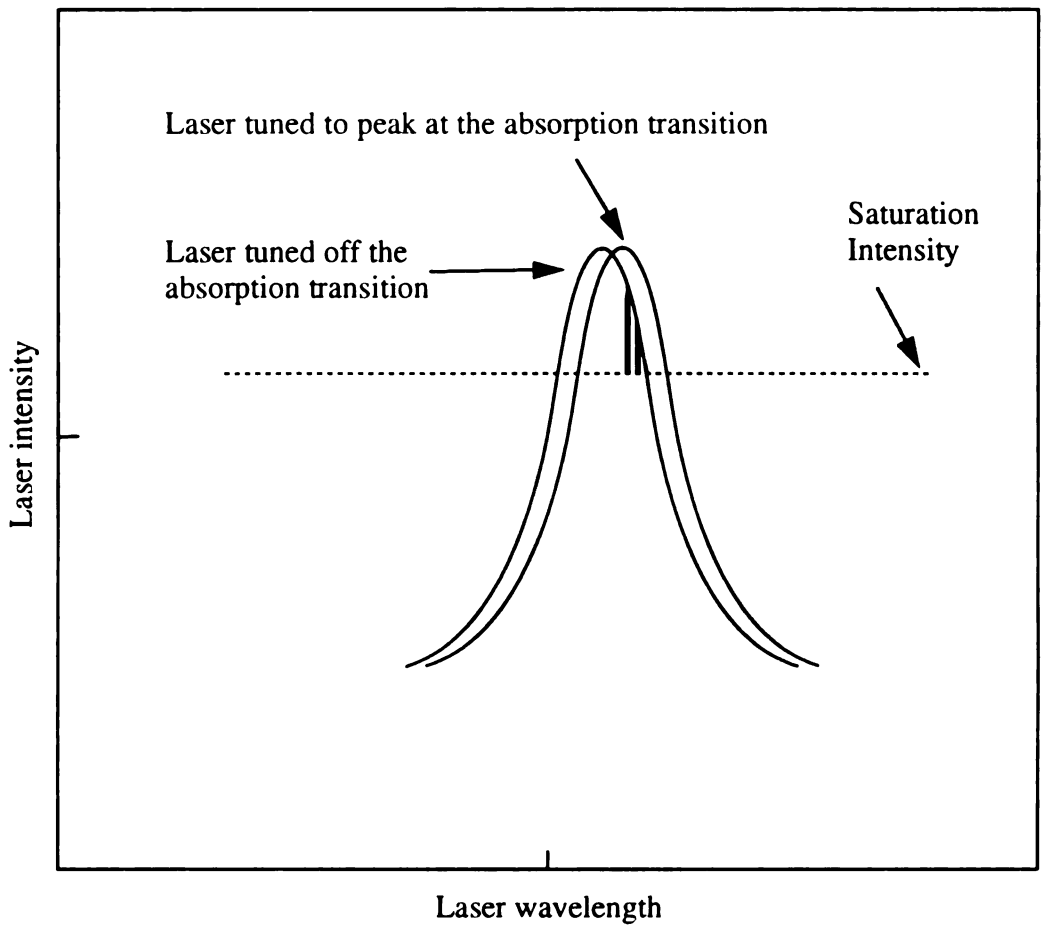

Figure 6.6: Sketch of saturation broadening effect. A tuned laser saturates the transition but a laser tuned off the transition may also saturate the absorption.

were taken using a 1.2 OD filter in place and a laser energy of 0.0033 W. In the interest of signal to noise certain relative measurements such as the longitudinal ion velocity distribution measurements were taken without attenuation of the laser. Figure 6.7 shows the effect of beam attenuation on the FWHM of the argon metastable ion line.

6.6 Ion energies

The ion energy distribution in Figure 6.5 is found at the center of the source region (r=0, z=1 on Figure 6.4) with a radial laser beam. The resolved ion energy is found to be about 0.2 eV after reducing the laser power to minimize power broadening, deconvolving the laser broadening and verifying negligible magnetic fields. Due to residual power broadening this is set as an upper limit until further research refines the measurement.

The full width at half maximum (FWHM) of a typical velocity distribution is determined from the data through a series of steps. First, the baseline or noise level of the measurements is determined. The baseline is the average value of the fluorescence intensity at wavelengths greater than 0.1 Å from the peak intensity. A number of data points in this region are averaged. Second, the half maximum points are determined by subtracting the baseline from the peak intensity, dividing by two and then adding the baseline back. Last, the wavelengths corresponding to the half maximum intensity are subtracted from one another giving the FWHM.

The observed FWHM of the distribution shown in Figure 6.5 is 0.043 Å. The measurement is taken at the center of the source where magnetic fields are small, therefore the Zeeman splitting is negligible compared to the other broadening mechanisms. The laser power was 0.0023 W to minimize power broadening. The radial ion energy is then found

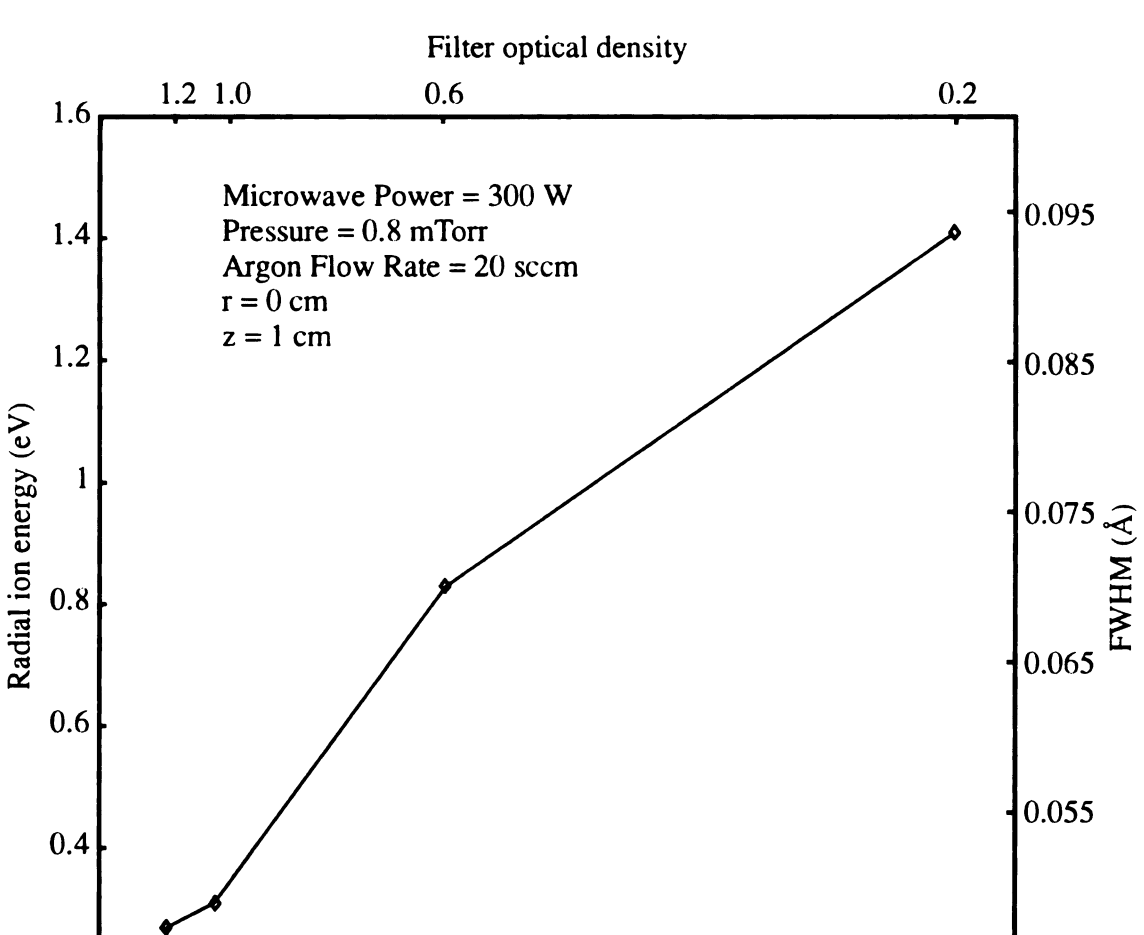

Figure 6.7: Radial ion energy versus power of laser and optical density.

by deconvolving the laser spectral broadening, using Equation 6.6. But first the observed FWHM must be converted to the same units as the laser spectral width:

$$\frac{FWHM\ (\mathrm{cm}^{-1})}{FWHM\ (\text{Å})} = \frac{16017.3\ \mathrm{cm}^{-1}}{6243.25\ \text{Å}}$$

$$FWHM\ (\mathrm{cm}^{-1}) = (16017.3\ \mathrm{cm}^{-1} / 6243.25\ \text{Å}) * 0.043\ \text{Å}$$
$$= 0.110\ \mathrm{cm}^{-1}$$

and then the laser spectral width can be deconvolved:

$$\Delta\lambda_D = \sqrt{(0.110)^2 - (0.07)^2}$$
$$= 0.085\ \mathrm{cm}^{-1}$$

Following Equation 6.5 and its assumptions the radial ion energy is determined:

$$kT = \frac{Mc^2}{8(ln2)}\left(\frac{\Delta\lambda}{\lambda_o}\right)^2 \qquad \text{Joules}$$

$$kT = \frac{40(1833)\left(9.11\times10^{-31}kg\right)\left(3.0\times10^{8}\frac{m}{s}\right)^2}{8(ln2)}\left(\frac{0.085cm^{-1}}{16017.3cm^{-1}}\right)^2$$

$$= 3.2 \times 10^{-20}\ \mathrm{J} = 0.20\ \mathrm{eV}$$

Figure 6.8 shows a similar distribution where the sample space is located at the same point (r=0, z=1). This distribution is taken with a longitudinal laser beam and the light collection optics set at an angle greater than ninety degrees (see Figure 6.4 for laser beam direction and optics set-up). The upper limit ion energy in this case is also 0.2 eV with the same experimental parameters as Figure 6.5.

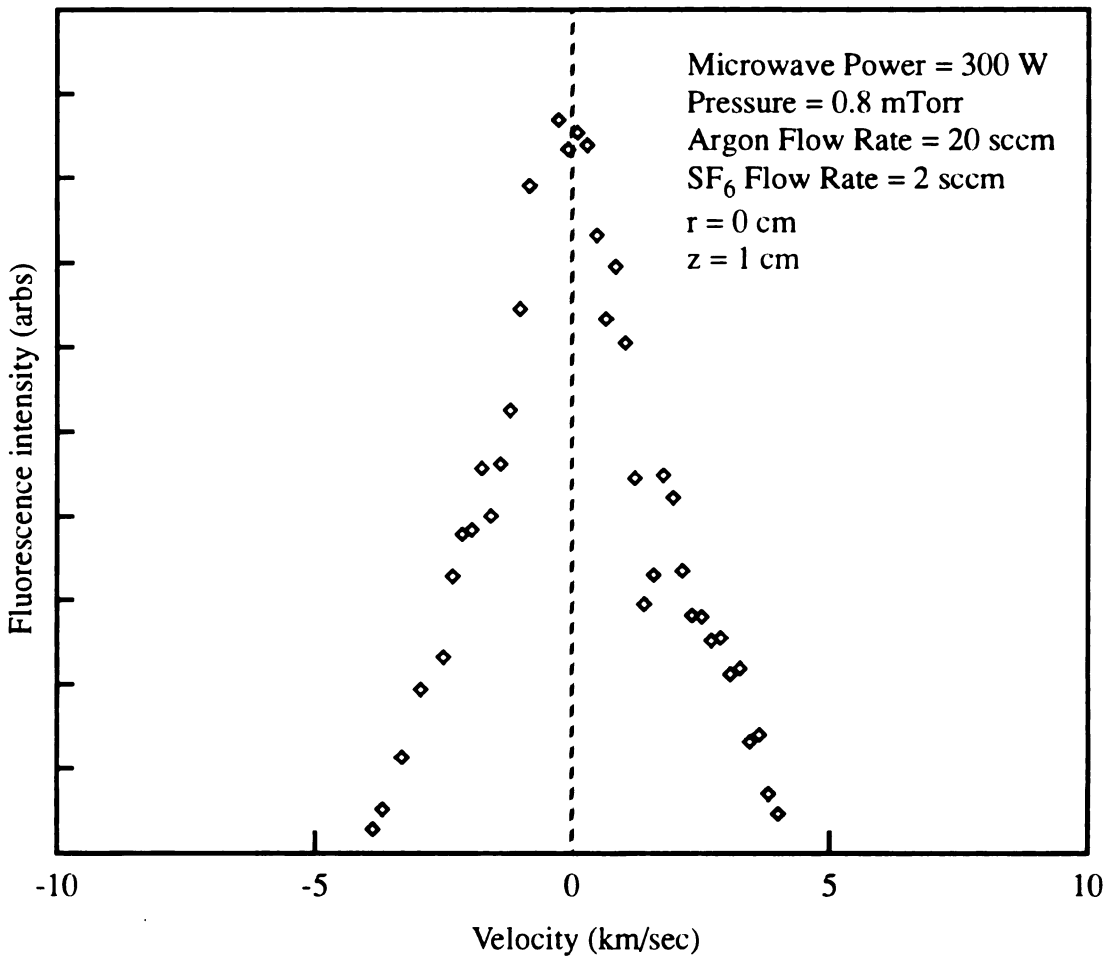

Figure 6.8: Longitudinal ion energy distribution.

6.7 Ion Velocities

Ion velocity distributions are found using the techniques described in Section 6.2. The velocity distributions are particularly interesting when comparing one location with another. Since the measurement is taken at the center of the source region the distribution of velocities is assumed to be random, therefore the peak of the distribution is chosen as the zero velocity point. The symmetry of the distribution about the zero velocity point substantiates the assumption of a random distribution.

As a test of this assumption the laser beam was directed into the source from the rear of the chamber as well as the front. The velocity distribution is measured relative to the direction of the laser with positive velocities in the direction of the laser and negative velocities in the direction opposite the laser. If the velocity in the source region was directed in some preferred direction and not random about the zero velocity point then the distribution with one laser direction may be shifted with respect the measured distribution with the opposite laser direction. The velocity distributions for both laser directions peaked at about the same wavelength indicating little if any directed velocity at the center of the source region. Figure 6.9 shows the velocity distribution for both laser directions.

The geometry used to describe the multipolar ECR system is shown in Figure 6.10 where the center point of the source region is chosen as the origin of polar coordinates ($r = 0, z = 0$). Longitudinally, this point lies at the base of the magnets and radially, at the center of the quartz chamber. The positive longitudinal direction is from the source to the processing region. The positive radial direction is from the origin out to the magnets.

Figure 6.11 shows a series of velocity distribution measurements taking at three different longitudinal positions. The important aspect of this figure is the shift of peak ion velocity from source to processing region. This indicates the ions have picked up a directed energy component as they leave the source. If the peak velocity of an ion at $z = 2$

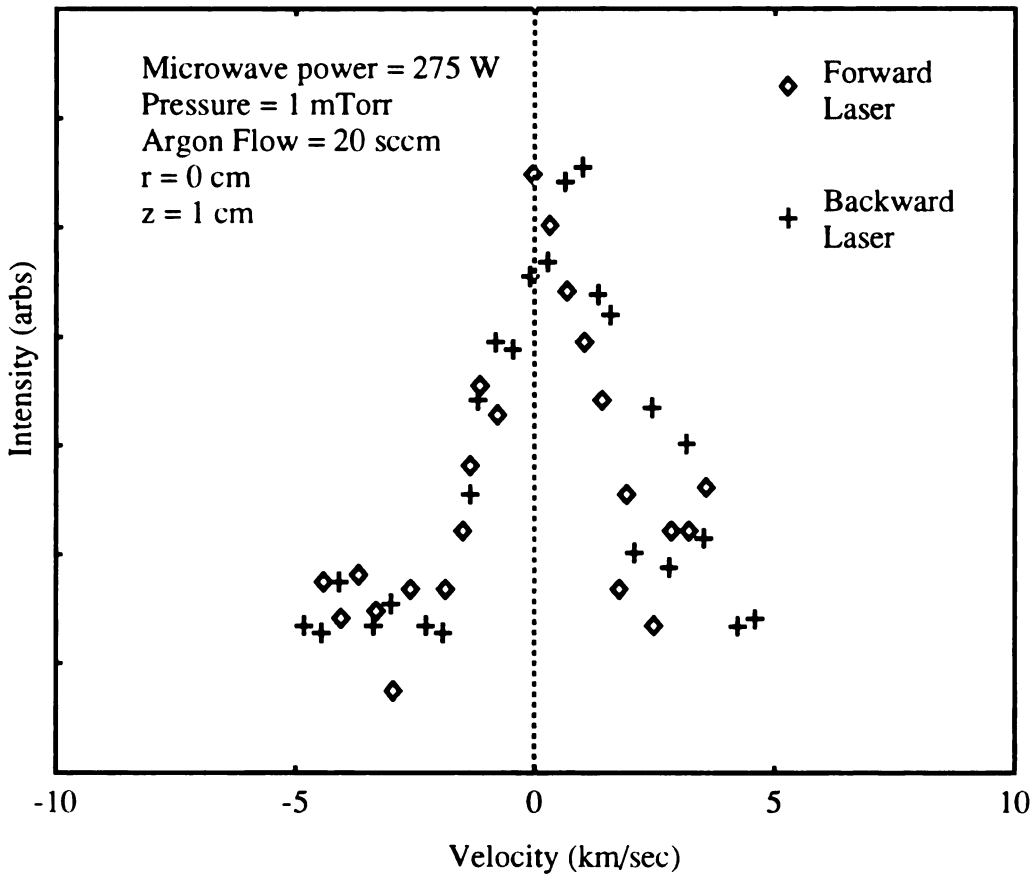

Figure 6.9: Argon metastable ion velocity distributions for two opposite radial laser directions.

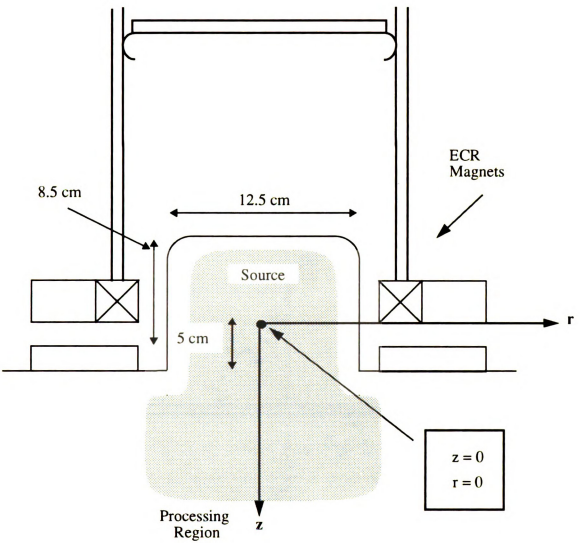

Figure 6.10: Geometry within source and processing regions of the ECR reactor.

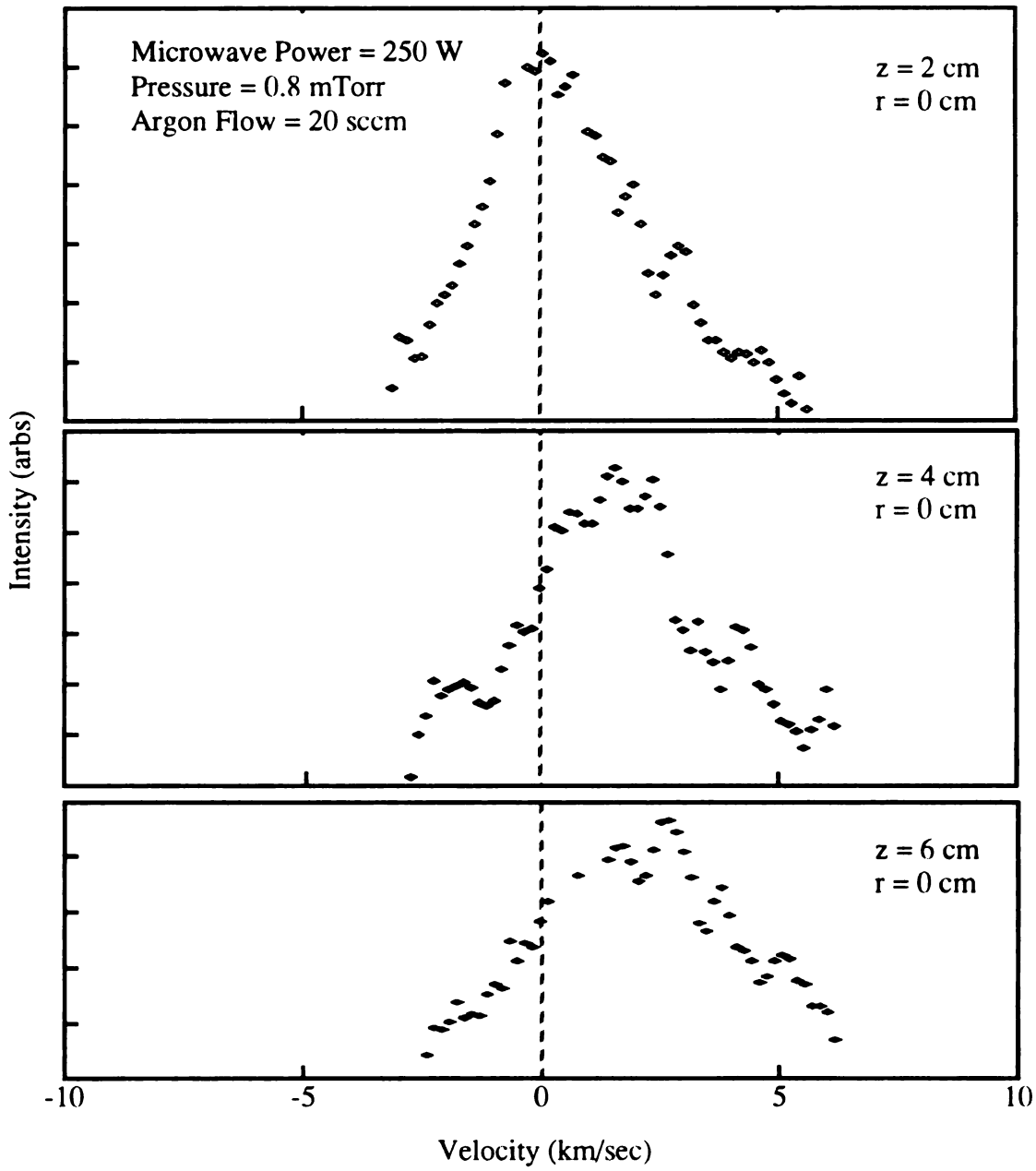

Figure 6.11: Velocity distribution at three different longitudinal positions.

cm is taken as the reference then the peak velocity at z = 4 cm is 1.24 km/sec and at z = 6 cm is 2.02 km/sec. This shows an increase of 2 km/sec over 4 cm.

6.8 Neutral temperature measurements

To determine the temperature of the neutral argon atoms in the discharge, optical emission spectroscopy (OES) was used. As with all OES techniques, the emission line profiles are broadened by numerous effects. The argon neutral in the low pressure discharge is broadened primarily by the Doppler effect and, in certain regions within the plasma source, by Zeeman splitting. At the operating pressures of the argon/SF_6 discharges natural and collisional broadening are insignificant. Typical charged particle densities are 10^{11} cm^{-3} so Stark broadening is negligible [29].

To determine the Doppler broadened width of the argon neutral, the optical emission of the discharge was collected with a fiber cable, columnated and passed through a Fabry-Perot interferometer. The width of the emission line was determined from a least squares fit to the observed intensity; but the observed linewidth is broadened by both the Doppler effect and by the finite spectral resolution of the interferometer/spectrometer equipment. Therefore, to accurately determine the Doppler width and thus, the temperature of the neutral argon atom the resolution of the spectrometer must be determined.

The resolution of the Fabry-Perot interferometer was determined by examining a xenon ECR discharge at a pressure of 0.7 mTorr, a flow rate of 10 sccm and microwave power of 150 W. The relatively heavy xenon atom was chosen since its Doppler width is likely to be smaller than the instrument broadening. The Doppler width of the $\lambda_0 = 4807$ Å xenon emission line is estimated to be 7×10^{-3} Å corresponding to a temperature of 600 K using equation 6.4. The observed xenon emission was Gaussian, therefore the estimated Doppler width of the line was deconvolved from the observed line to determine the instrument broadening of the interferometer. The width of the xenon line due to instrument

broadening is $\Delta\lambda = 0.0176$ Å. Thus, the resolution of the interferometer is estimated to be $(\Delta\lambda/\lambda_0) = 3.6 \times 10^{-6}$.

Figure 6.12 shows the results of a study of the effect of the addition of SF_6 to a pure argon discharge. The error bars in the measurements reflect the standard deviation of ten repetitions of each temperature measurement. The addition of the molecular gas to pure argon had the effect of reducing the neutral species temperature. It is believed less of the microwave energy imparted on the system is available to heat the neutral species as more of the input energy is utilized to excite, ionize and dissociate the complex molecular gas.

6.9 Statistical experimental results

The results presented below are for a a series of statistically designed experiments performed on an argon/SF_6 ECR discharge. The factors included in the design were microwave power, pressure and argon flow rate. This constitutes a 2^3 factorial design. The parameters and the results are tabulated in Table 6.1. All nineteen experiments were conducted with a SF_6 flow rate of 10% of the argon flow. The diagnostics performed include radial ion energy measured using LIF, neutral temperature and ion density.

6.9.1 Radial ion energy results

The radial ion energy was calculated from the full width at half maximum of the laser induced fluorescence of the argon metastable ion as described in Section 6.6. The results were analyzed using the statistical techniques described in Chapter 3. The analysis of variance of the radial ion energy shows that the first order effects are insignificant at a significance level of $\alpha = 0.1$. These effects were, therefore, pooled with the second order effects into the error. The effect of argon flow rate is non-significant at a level of 0.05 when compared to this new error term. The remaining main effects, pressure and incident

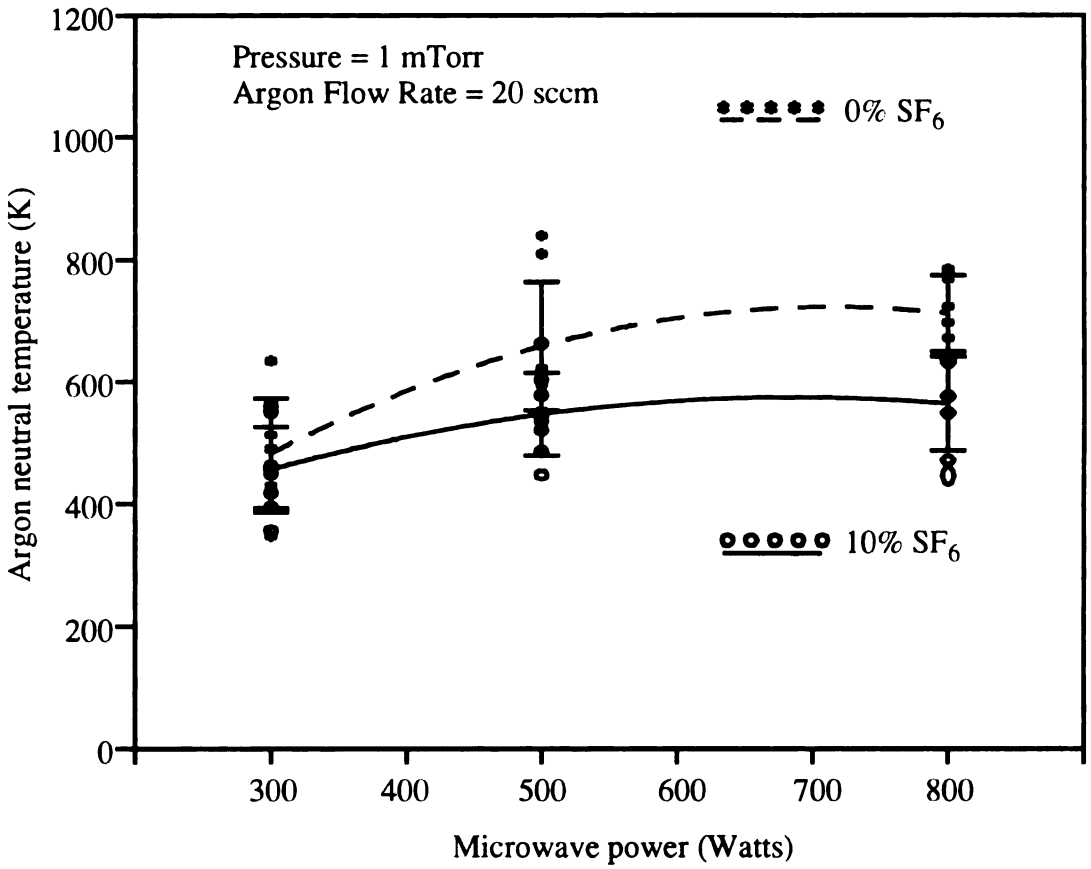

Figure 6.12: Neutral argon temperature versus SF_6 concentration and microwave power.

microwave power are significant at a level of $\alpha = 0.025$ or less. The ANOVA for the radial ion energy is shown in Table 6.2. Note that for the analysis of variance the radial ion

Table 6.1 Argon/SF_6 statistically designed experiment.

Run #	Incident Microwave Power (W)	Pressure (mTorr)	Argon Flow (sccm)	Ion Density (cm^{-3})	Neutral Temperature (K)	Radial Ion Energy (eV)
1	225	2.5	25	2.21×10^{11}	601 ± 41	0.25
2	225	2.5	25	2.41×10^{11}	598 ± 35	0.26
3	225	2.5	25	2.21×10^{11}	589 ± 38	0.27
4	225	2.5	25	2.34×10^{11}	605 ± 30	0.25
5	225	2.5	25	2.30×10^{11}	597 ± 35	0.25
6	175	2.0	20	1.41×10^{11}	565 ± 35	0.22
7	175	2.0	30	1.93×10^{11}	542 ± 38	0.23
8	175	3.0	20	1.51×10^{11}	573 ± 42	0.21
9	175	3.0	30	2.18×10^{11}	557 ± 25	0.22
10	275	2.0	20	2.26×10^{11}	599 ± 26	0.25
11	275	2.0	30	2.26×10^{11}	577 ± 32	0.25
12	275	3.0	20	2.32×10^{11}	612 ± 26	0.24
13	275	3.0	30	2.56×10^{11}	596 ± 37	0.24
14	150	2.5	25	1.37×10^{11}	544 ± 22	0.22
15	300	2.5	25	2.61×10^{11}	672 ± 26	0.30
16	225	1.0	25	1.59×10^{11}	525 ± 32	0.28
17	225	4.0	25	2.39×10^{11}	616 ± 33	0.20
18	225	2.5	17	2.32×10^{11}	650 ± 31	0.26
19	225	2.5	33	2.31×10^{11}	505 ± 23	0.25
			SSE =	0.0297×10^{22}	140.0	0.0004

energy values were scaled by multiplying each value by 10. The sums of squares and the mean square values were calculated using the scaled values. The regression analysis, though, used radial ion energy values which were not scaled. Since the F-test utilizes ratios, scaling does not effect the significance values.

To check if the radial ion energy may be dependent on power, pressure or flow in a nonlinear fashion, the energy data were plotted against each of these factors individually. Using the center and star points in Table 6.1, the linearity checks (Figures 6.13, 6.14, 6.15)

Table 6.2 ANOVA of radial ion energy and argon neutral temperature.

	Radial Ion Energy			**Argon Neutral Temperature**		
	Mean Square	**DF**	α	**Mean Square**	**DF**	α
Pressure	2.00	1	0.025	378.13	1	0.002
Incident Power	12.50	1	0.001	2701.13	1	< 0.001
Argon Flow				741.12	1	0.001
Error	0.2	5		7.88	4	

show that radial ion energy varies linearly over the ranges of pressure, power and flow measured in this study.

Since the ANOVA showed no first nor second order effects and the linearity checks showed the linear dependence, the regression included only the factors of incident power and pressure. The predicted value of radial ion energy versus the observed values is shown in Figure 6.16. The standard deviation of the model from the observed values is 0.016. The final model of radial ion energy for the range of factors studied here is:

$$\text{Predicted Radial Ion Energy (eV)} = 0.00035 * \text{Incident Power (W)} - 0.0215 * \text{Pressure (mTorr)} + 0.219 \pm 0.016$$

The model is shown in Figure 6.17. The coefficient of determination (R^2) for this model is 0.795. The model, therefore, predicts about 80% of the actual observed values.

The error sum of squares (*SSE*), found using runs # 1-5, is 0.0004. The residual sum of squares (*SSR*) is 0.00399. Therefore, the sum of squares associated with lack of fit of this model is 0.00359. An F-test on the mean square due to lack of fit to the mean

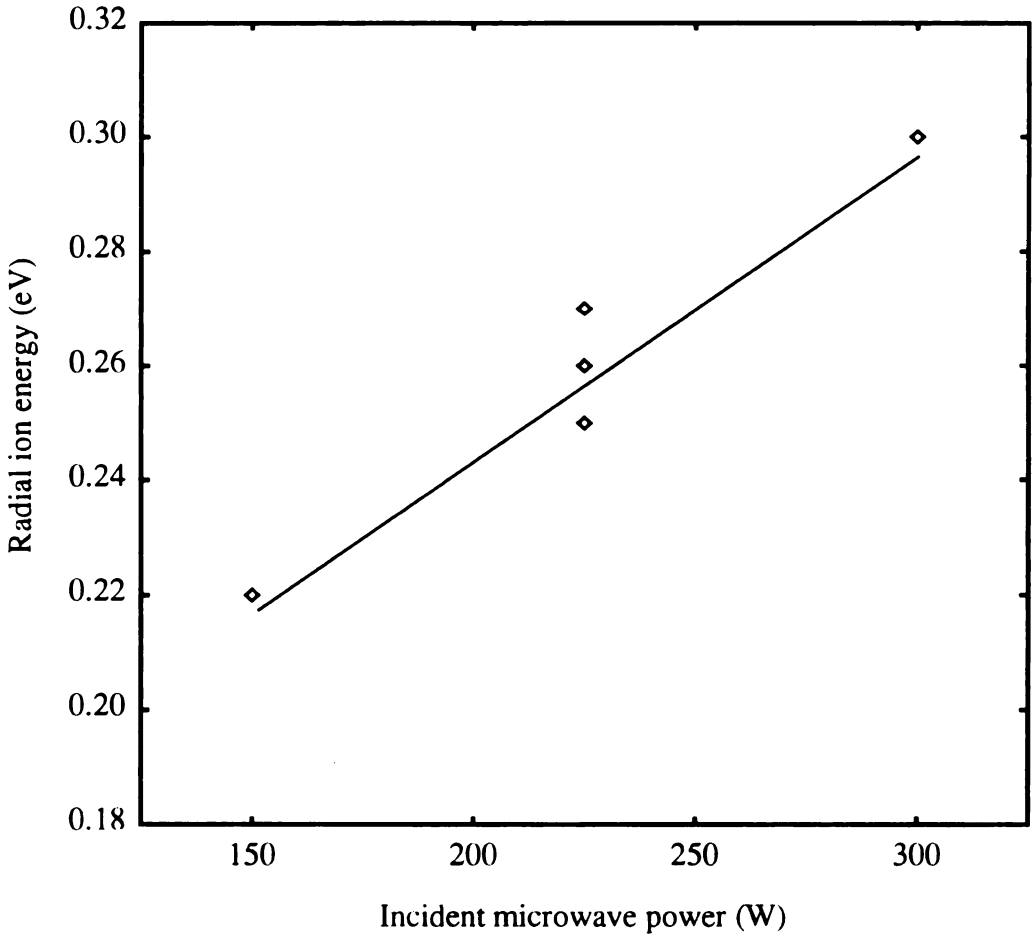

Figure 6.13: Least squares fit of radial ion energy to incident microwave power. Pressure = 2.5 mTorr, argon flow = 25 sccm.

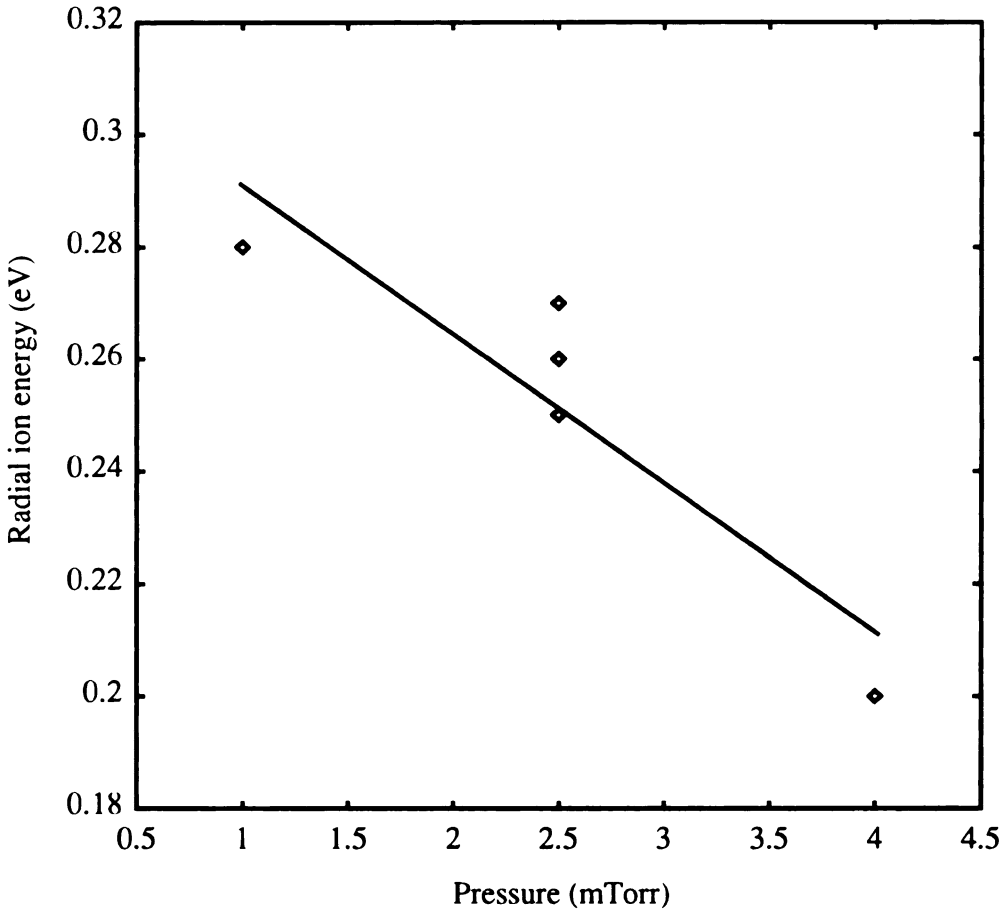

Figure 6.14: Least squares fit of radial ion energy to pressure. Incident microwave power = 225 W and argon flow = 25 sccm.

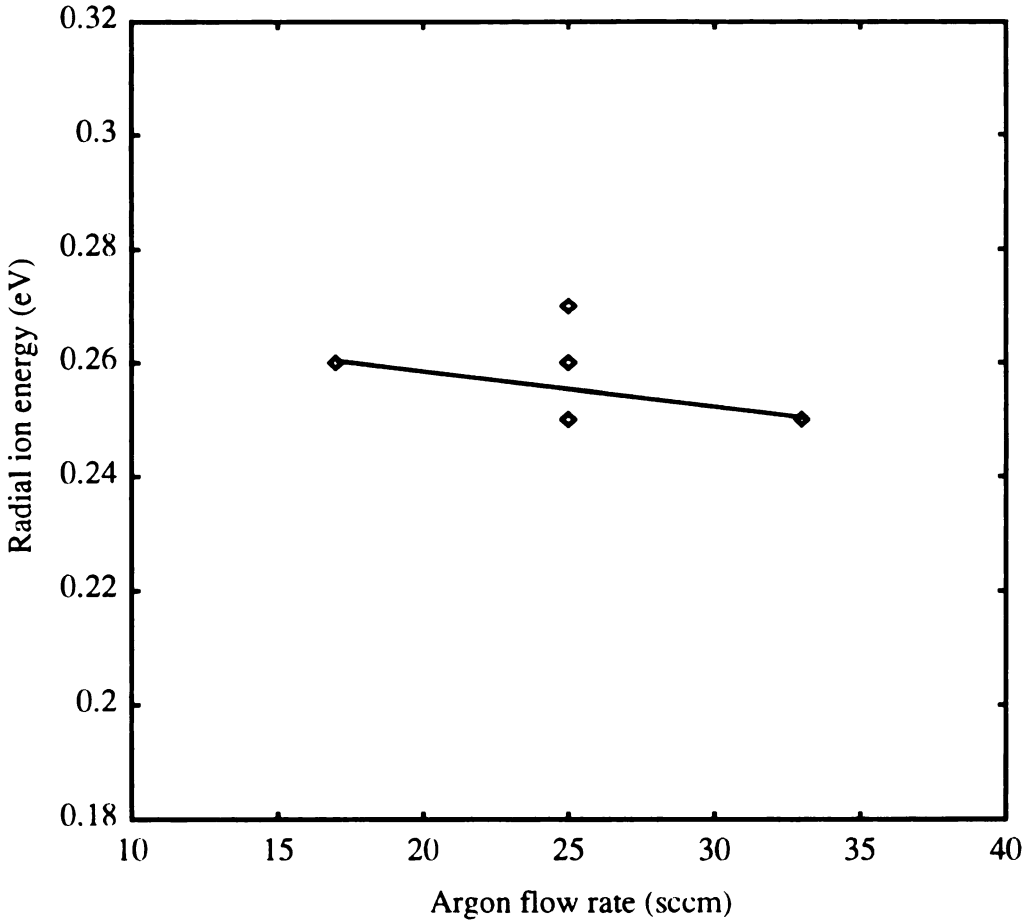

Figure 6.15: Least squares fit of radial ion energy versus argon flow.
Incident microwave power = 225 W and pressure = 2.5 mTorr.

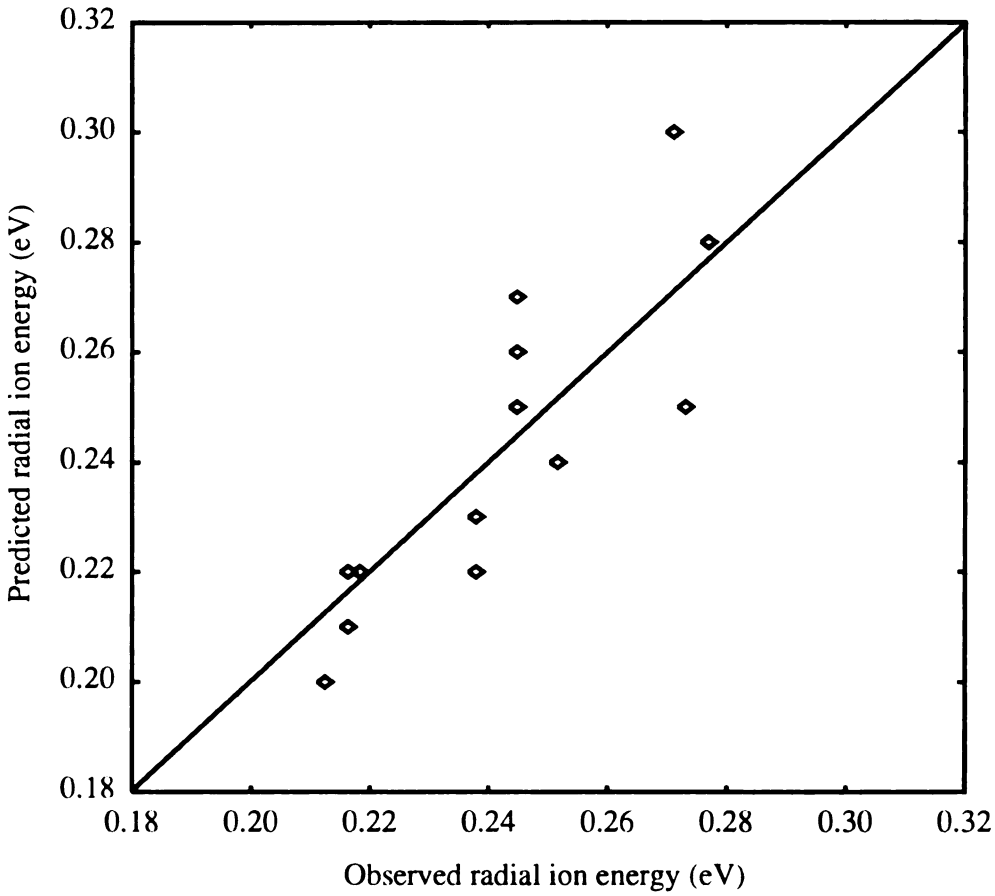

Figure 6.16: Predicted radial ion energy versus observed radial ion energy. Straight line represents perfect agreement between model and experiment.

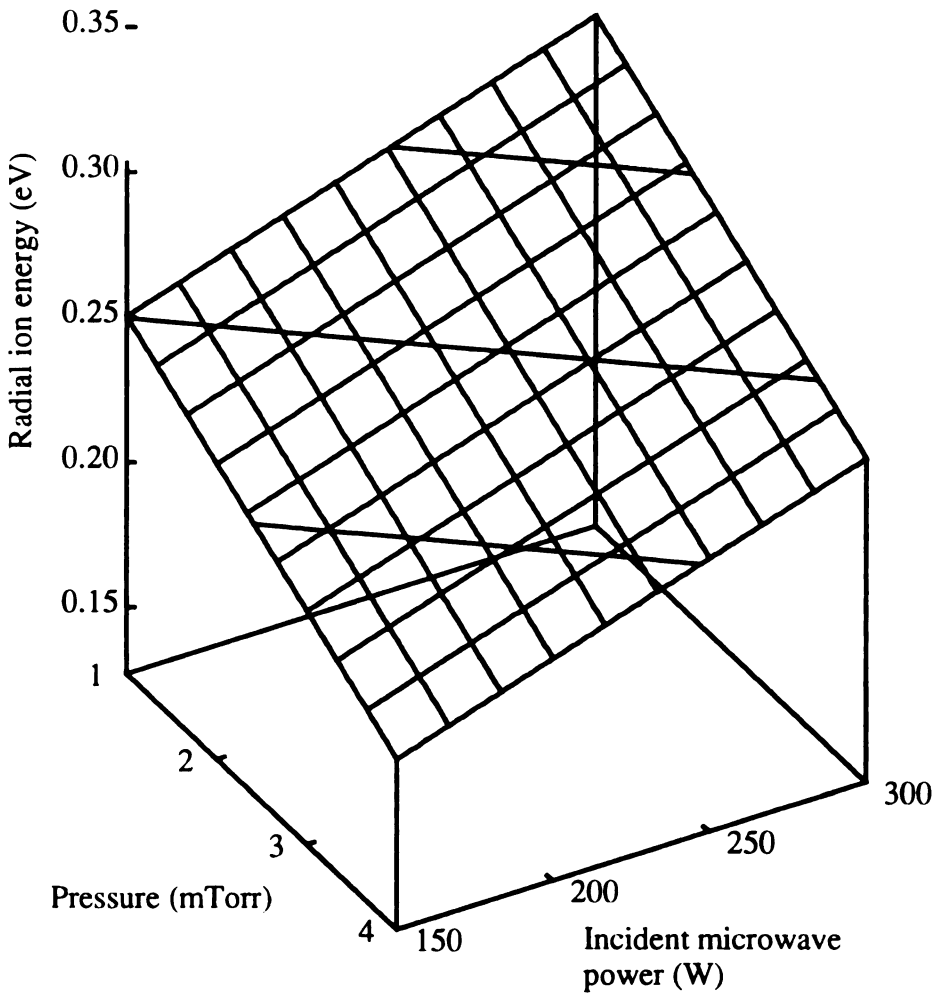

Figure 6.17: Predicted radial ion energy plotted versus pressure and incident microwave power. Contours at 0.22, 0.25, and 0.28 eV.

square due to experimental error shows the lack of fit portion of the residual error is more significant than the experimental error portion at a level of $\alpha = 0.25$.

6.9.2 Neutral temperature results

The neutral temperature results are presented in Table 6.1 for the argon/SF_6 ECR discharge. Each of the nineteen neutral temperatures presented in Table 6.1 is the mean of five measurements. The standard deviation for each of these measurements is also presented. The ANOVA of these results are summarized for the significant effects in Table 6.2. All three main effects, pressure, incident power and argon flow, were shown to be significant at a level of $\alpha = 0.002$ or less. The first order and second order effects were not significant at a level of $\alpha = 0.3$ or higher so were they were pooled with the error.

The model is a linear least squares regression fit to the statistically designed experiments. The model of neutral temperature variation is:

Predicted Neutral Temperature (K) = 518.1 + 25.2 * Pressure (mTorr) +
0.542 * Incident Power (W) - 4.70 * Argon Flow (sccm) ± 24.6

The model is plotted versus pressure and incident microwave power in Figure 6.18 and plotted versus argon flow and pressure in Figure 6.19. A plot of the predicted neutral temperature versus the observed neutral temperature is shown in Figure 6.20. The R^2 for this model is 0.69 and $SSR = 9095$. The standard deviation of the fit to the mean observed data is 24.6 K. From the sum of squares of the residuals and the sum of squares of the experimental error, the lack of fit is significant at a level of $\alpha = 0.01$. Therefore, the model explains 70% of the observed data and most of the residual error is from lack of fit and not experimental error. These calculations were done without considering the inherent uncertainty of the neutral temperature determination.

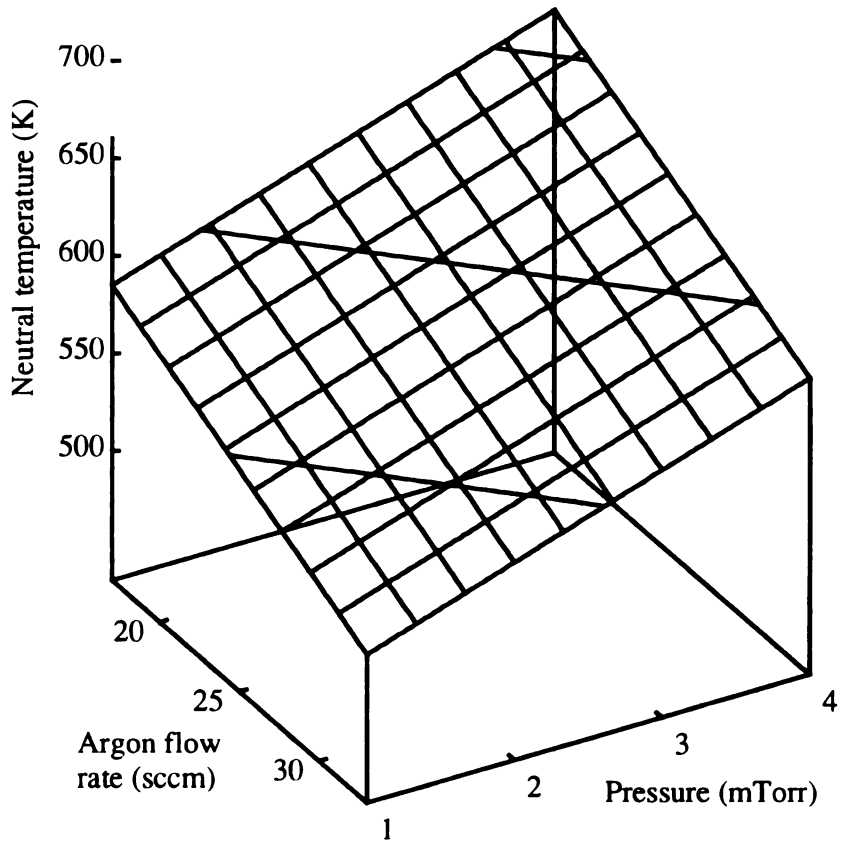

Figure 6.18: Predicted argon neutral temperature plotted versus pressure and argon flow rate. Incident microwave power = 225 W. Contours at 550, 600, 650 K.

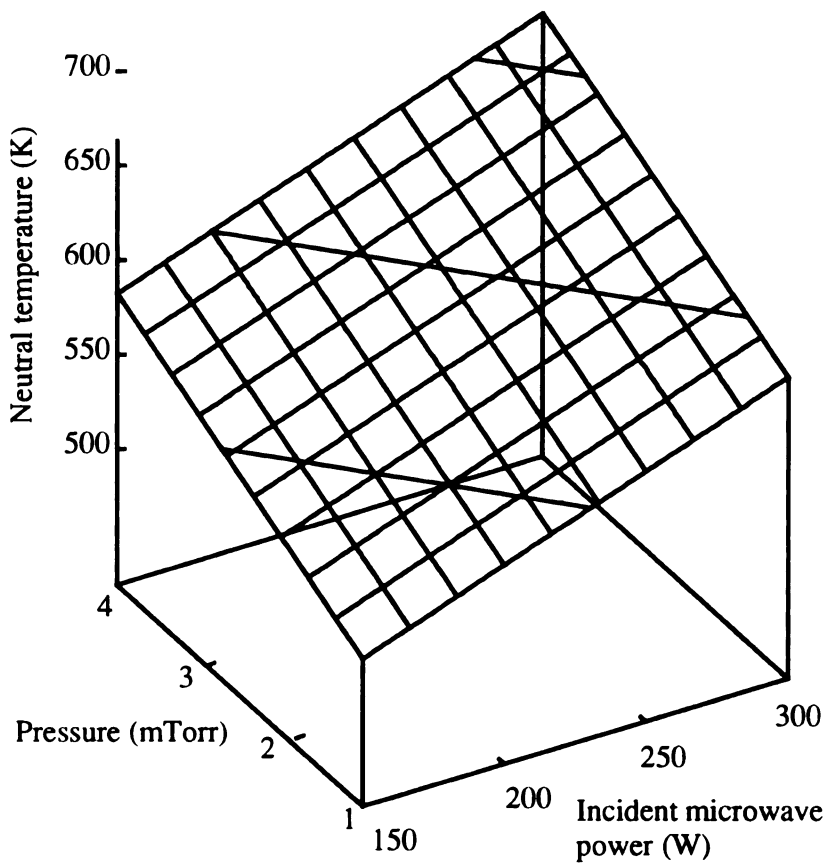

Figure 6.19: Predicted neutral temperature plotted versus pressure and incident microwave power. Contours at 550, 600, and 650 K. Argon flow = 25 sccm.

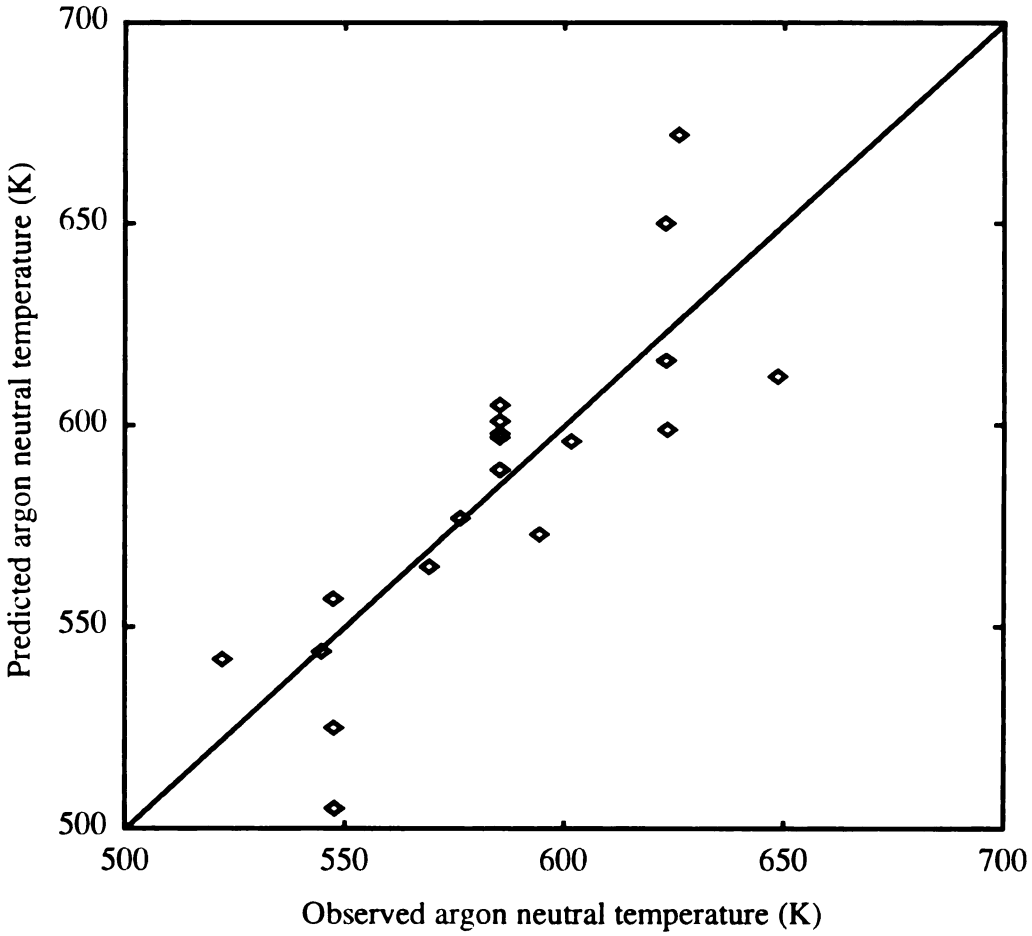

Figure 6.20: Predicted neutral temperature plotted versus observed neutral temperature. Straight line represents perfect agreement between observation and prediction.

6.9.3 Ion density results

To examine the variation of ion density in the argon/SF_6, a double Langmuir probe was placed in the discharge at z = 1 cm and r = 0 cm as shown in Figure 3.2. The Langmuir probe current/voltage characteristics were analyzed following the procedure of Reference [93]. The ion density results are listed in Table 6.1. The ANOVA results are listed in Table 6.3.

The ANOVA indicates that pressure, incident power and argon flow main effects are all significant at level of 0.05 or less for the parameter range studied. The higher order effects, again, have all been pooled with the error.

The model of the ion density variation in this study was found using linear regression techniques as:

$$\text{Predicted Ion Density } (\times 10^{11}\ \text{cm}^{-3}) = 0.0067 * \text{Incident Power (W)} + 0.24 * \text{Pressure (mTorr)} + 0.022 * \text{Argon Flow (sccm)} - 0.53 \pm 0.21$$

Table 6.3 ANOVA of Ion density.

	Ion Density ($\times 10^{11}$ cm^{-3})		
	Mean Square	**DF**	α
Pressure	0.060	1	0.054
Incident Power	0.700	1	0.002
Argon Flow	0.260	1	0.010
Error	0.010	4	

This predicted ion density with a coefficient of determination (R^2) of 0.748 is plotted versus observed ion density in Figure 6.21. The standard deviation of the predicted density from the observed density is 0.21 x 10^{11} cm^{-3} and SSR = 0.657 for this model. The model of ion density is plotted versus pressure and incident power in Figure 6.22 and ver-

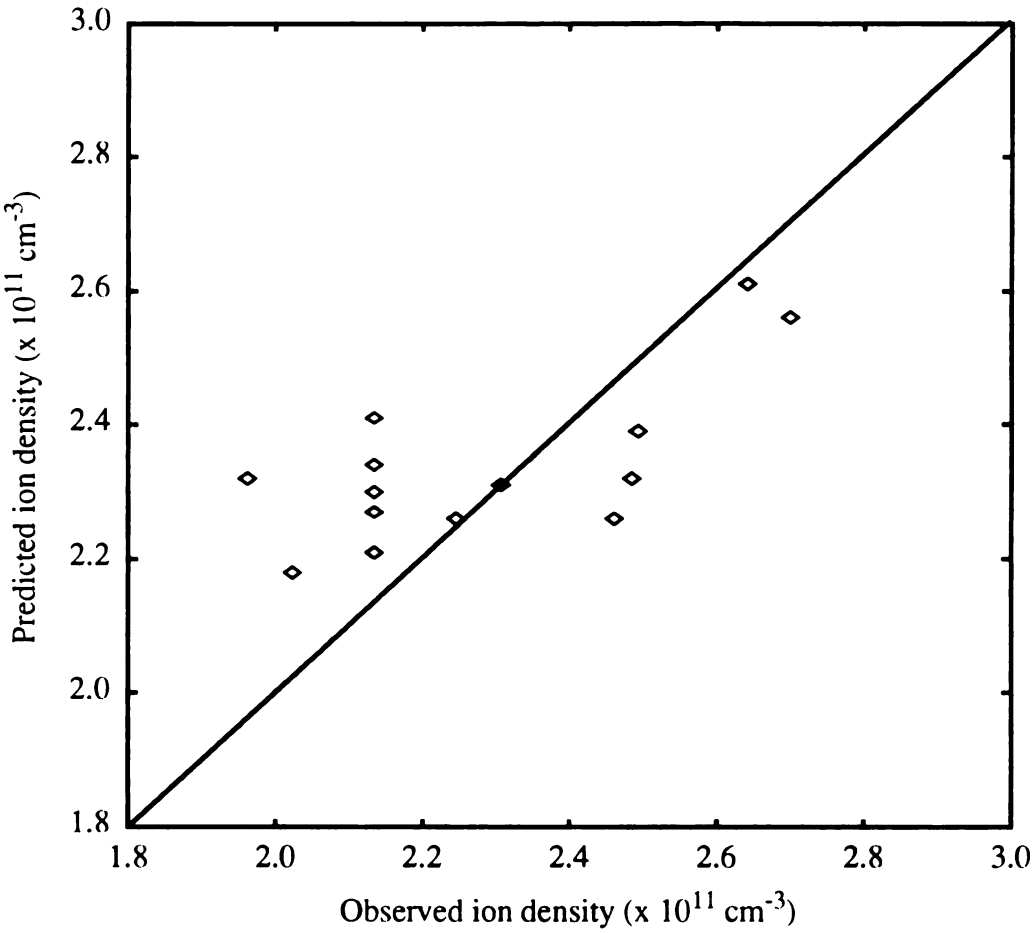

Figure 6.21: Predicted argon ion density plotted versus observed argon ion density. Straight line represents perfect agreement between observation and prediction.

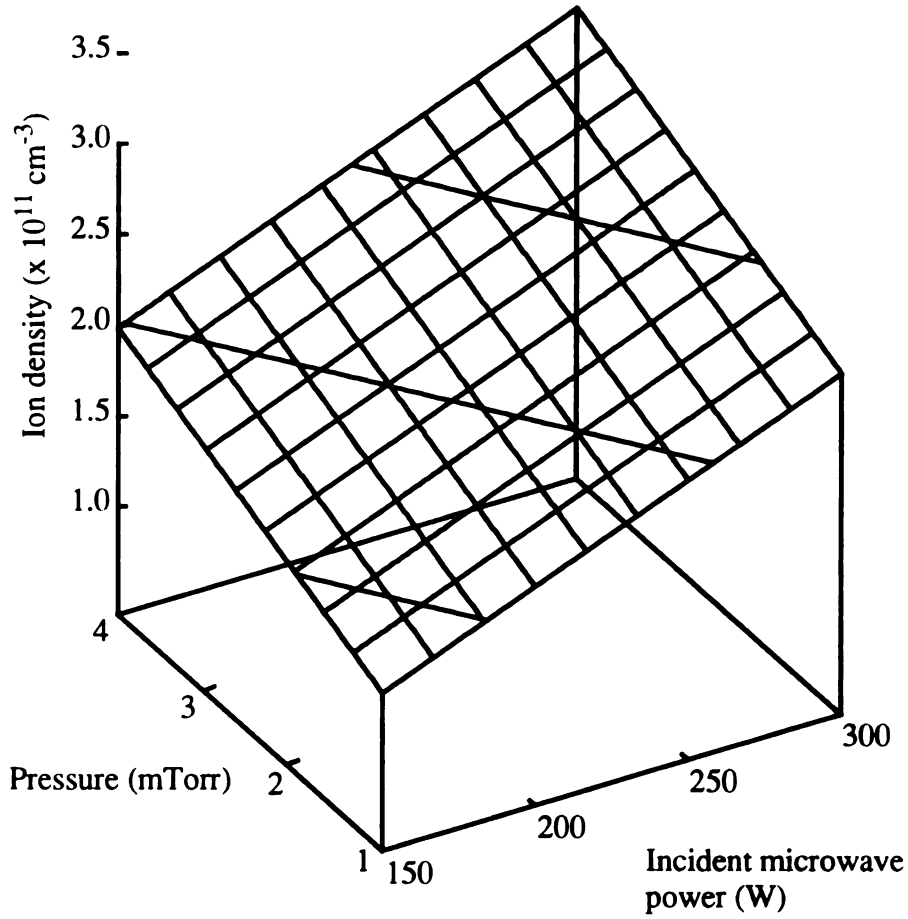

Figure 6.22: Predicted argon ion density versus pressure and incident microwave power. Contours at 1.5, 2.0, and 2.5 x 10^{11} cm^{-3}. Argon flow = 25 sccm.

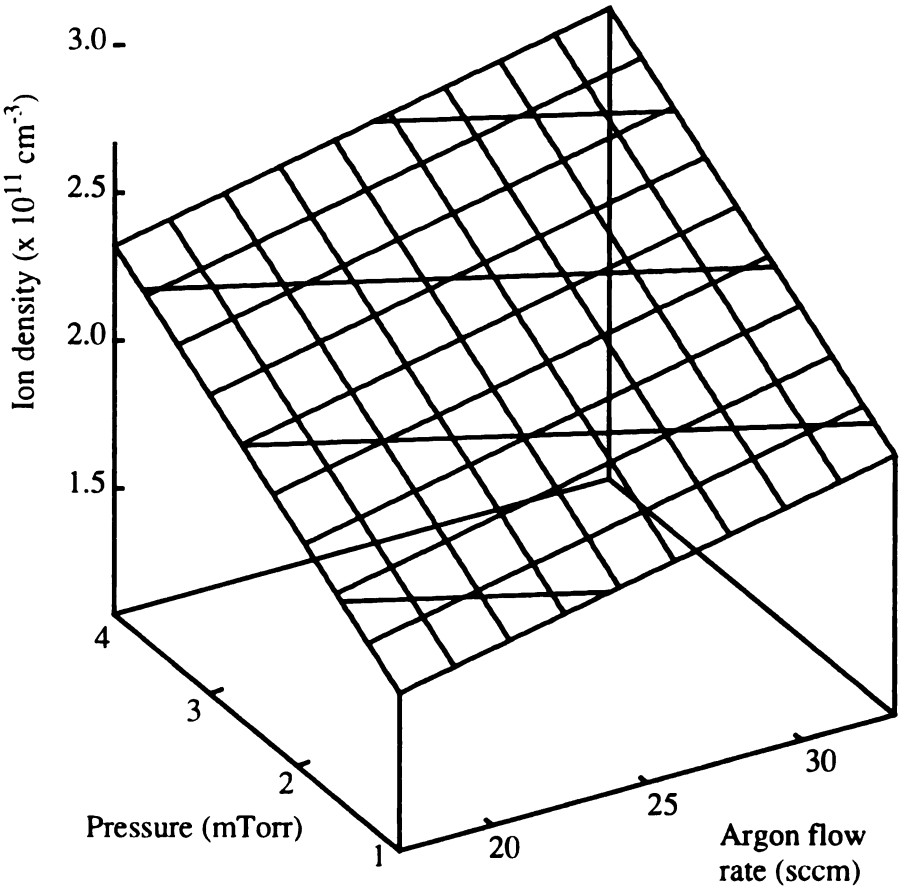

Figure 6.23: Predicted argon ion density versus pressure and argon flow rate. Contours at 1.75, 2.0, 2.25, and 2.5 x 10^{11} cm^{-3}. Incident microwave power = 225 W.

sus pressure and argon flow in Figure 6.23. Again, lack of fit is significant at a level of α = 0.01.

6.10 Conclusions

The operation of the LIF system for determining ion velocities has been demonstrated. The ion energy within the source region (r = 0 cm, z = 1 cm) is given an upper limit of 0.2 eV regardless of laser direction at a pressure of 4 mTorr with 300 Watts of microwave power and an argon gas flow of 20 sccm and an SF_6 gas flow rate of 2 sccm. This is only an upper limit since residual line broadening.

A set of statistically designed experiments was performed over a parameter space known to be useful for silicon etching. This set of experiments lead to regression models of the radial ion energy in the source region. The regression model shows ion energy increases as incident microwave power increases from 150 W to 300 W. The model also shows that radial ion energy decreases as pressure increases from 1 mTorr to 4 mTorr. The model shows no significant variation as flow increased.

The neutral species temperature in the argon-SF_6 plasma was measured using optical emission spectroscopy (OES) to determine the Doppler-shifted linewidth of the emission from an argon atom. Through a set of statistically designed experiments a regression model of the variation in temperature was developed. The regression model shows neutral temperatures increase as incident microwave power is increased from 150 W to 300 W. Also, the temperature increases as pressure is increased from 1 mTorr to 4 mTorr. Neutral temperature decreases, though, as flow is increased from 17 sccm to 33 sccm.

The ion density was estimated using a double Langmuir probe technique over the same range of pressure, power and flow and using the same set of statistically designed experiments. The ion density increased as pressure, power and flow increased.

The experiments performed here paid special attention to minimizing the errors associated with optical diagnostic techniques. The LIF experiments were performed in a manner to reduce or compensate for line broadening mechanisms other than Doppler broadening. For instance, saturation broadening was reduced through the use of neutral density filters. Zeeman splitting was negligible at the center of the source where these measurements were performed. The LIF measurements were also performed with special attention to the signal to noise ratio. The signal strength was maximized through alignment of the optical system and the laser beam. The noise was reduced through boxcar averaging techniques. The OES measurements were performed using a Fabry-Perot interferometer to increase the spectral resolution of the light collection.

Finally, the statistically designed experiments were designed to quantify any errors that may remain. The repeated center point experiments provided a measure of the experimental error associated with factors that may be out of the control of the operator. The regression models included error values to quantify the deviation of the model from the observed experimental values. The correlation of the experimental error and the error of the model provides a measure of the lack-of-fit parameter to determine the basis of the model error--experimental or statistical.

Chapter 7

Summary of Results and Recommendations for Future Research

7.1 Summary of results

A study of the properties of the neutral and ionic species in microwave cavity discharges was undertaken for the purpose of increasing the understanding of these types of discharges, for improving the reactor design and to provide a basis for modeling the physics of the discharge. Two basic types of microwave cavity based discharges were examined: 1) the multipolar ECR (electron cyclotron resonance) microwave cavity reactor, used at very low pressure (~ 1 mTorr) for semiconductor processing applications and 2) the microwave cavity plasma reactor, used for a variety of applications including diamond thin film deposition. The microwave cavity plasma reactor is useful over a wide pressure range. The properties of the ion and neutral species in this reactor were studied at low pressure (< 1 Torr), moderate pressure (between 10 and 100 Torr) and high pressure (> 100 Torr).

7.1.1 Summary of the multipolar ECR argon\SF_6 discharge diagnostics

Argon and sulfur hexafluoride discharges have been used extensively for silicon etching applications. The ion, electron and neutral species in the multipolar ECR microwave cavity reactor have been studied using Langmuir probes and other plasma diagnostic tools [93]. The use of novel techniques such as laser induced fluorescence has been done in this work. Additionally, a set of statistically designed experiments have been performed to form the basis for a statistical models of the ion and neutral species temperatures and energies in the discharge source region.

The statistically designed experiments used response surface methodology techniques to model the response of the metastable ion energy, neutral temperature and ion density in the source region of an argon/SF_6 discharge. These models are useful in predicting the response of the discharge to variations in pressure, microwave power and gas flow rate.

The ion energy in the radial direction as defined in Chapter 6, varies strongly with microwave power and pressure changes as follows:

$$\text{Predicted Radial Ion Energy (eV)} = 0.00035 * \text{Incident Power (W)} - 0.0215 * \text{Pressure (mTorr)} + 0.219 \pm 0.016$$

The ion energy measured using laser induced fluorescence increases as microwave power increases. The ion energy decreases seen in the source region of the discharge as pressure is increased. Also, note that the shift in ion velocity distribution from the source to the processing region is consistent with a plasma potential variation [93].

The modeled neutral temperatures in the multipolar ECR argon/SF_6 discharge vary with changes in microwave power, pressure and argon flow rate as:

$$\text{Predicted Neutral Temperature (K)} = 518.1 + 25.2 * \text{Pressure (mTorr)} + 0.542 * \text{Incident Power (W)} - 4.70 * \text{Argon Flow (sccm)} \pm 24.6$$

As power and pressure are increased the temperature of the neutral species increases also. The neutral species in the discharge gain energy through collisions with charged particles. The collisions can be collisions with ions or electrons or charge exchange collisions with ions. Energetic neutral species can also be created from electron/ion wall recombinations. Since charged particle densities are increasing as pressure and power increases, the gas temperature will also increase. As the flow rate is increased, especially for a constant pressure, the time a neutral species remains in the source region of the discharge will decrease, thus the total energy a neutral particle can gain through the collisional and recombination

processes is reduced. All three of these variations are accounted for in the model developed for the neutral temperature.

A model of ion density variation over a pressure range of 1 - 4 mTorr, an incident microwave power range of 150 - 300 W and an argon flow rate range of 19 - 50 sccm with an SF_6 flow rate equal to 10% of the argon flow rate was developed for the multipolar ECR reactor. The statistically designed model is:

$$\text{Predicted Ion Density } (\times 10^{11}\ \text{cm}^{-3}) = 0.0067 * \text{Incident Power (W)} + 0.24 * \text{Pressure (mTorr)} + 0.022 * \text{Argon Flow (sccm)} - 0.53 \pm 0.21$$

The ion density increases with increases in microwave power as expected from the increase in absorbed energy and the corresponding increasing in electron-neutral ionizing collisions. The ion density also increases as pressure and flow rate increase. The increase in available neutral species in the source region of the reactor results in an increased ionization frequency at higher pressures.

7.1.2 Summary of the low pressure hydrogen discharge

A series of diagnostic measurements were performed on a pure hydrogen discharge. The hydrogen atomic temperatures were measured in the discharge operated at a pressure range of 0.1 - 0.4 Torr, an incident power range of 150 - 300 W and a range of hydrogen flow of 19.2 - 50 sccm. The model of hydrogen translational temperature is:

$$\text{Predicted Hydrogen Translational Temperature (K)} = 1179.2 + 0.974 * \text{Incident Power (W)} + 211.2 * \text{Pressure (Torr)} \pm 53.6.$$

The temperature increased as power and pressure increased. The hydrogen electronic temperature, though, decreased as pressure was increased but also increased with increasing power. The hydrogen electronic temperature is modeled by:

$$\text{Predicted Electronic Temperature (K)} = 1767.0 + 7.52 * \text{Incident Power (W)} - 2795.2 * \text{Pressure (Torr)} + 9751.0 * [\text{Pressure (Torr)}]^2 - 16.32 * \text{Pressure (Torr)} * \text{Incident Power (W)} \pm 101.9.$$

7.1.3 Summary of the high pressure diamond deposition discharge

The diagnostics of the low pressure hydrogen discharge were also performed on a high pressure reactor used for diamond thin film deposition. This discharge was operated at a pressure range of 115 - 135 Torr. The hydrogen flow rate was varied from 450 - 750 sccm and methane was added at a flow rate equal to 3% of the hydrogen flow. The incident microwave power was varied from 3.4 - 4.5 kW. These parameters were chosen because diamond thin films have been successfully grown in this range.

The hydrogen atomic temperatures, translational and electronic, were found to not vary significantly over this range of parameters. The translational temperature for all the experiments performed had a mean value of 1932 K ± 172 K. The electronic temperature mean value was 1953 K ± 81 K. Notice these values are very close to each indicating that the various degrees of freedom of the energy in an atom are coming to an equilibrium.

Since a carbon containing species is present in the discharge the molecular rotational temperature can also be measured. The rotational temperature of the C_2 molecule was measured using optical emission spectroscopy techniques. The rotational temperature is assumed to be very close to the translational temperature of the molecules in the discharge. Since the rotational energy levels are very close to one another, the rotational excitation of the molecule via interaction with its translational degree of freedom is very efficient. The mean rotational temperature is 1999 K ± 186 K, but the rotational temperature did exhibit some variation over the parameter space given by the following model:

Predicted C_2 Rotational Temperature (K) = 10023.2 - 4046.8 * Incident Power (kW) + 3.51 * Hydrogen Flow (sccm) * Incident Power (kW) - 0.11 * Hydrogen Flow (sccm) * Pressure (Torr) + 15.86 * Pressure (Torr) * Incident Power (kW) ± 100.5

The substrate was in place for all of these measurements. The substrate holder was water cooled from below and the substrate temperature was monitored at the center of the processing surface. The temperature varied slightly from about 850 C to 980 C and is modeled by:

Predicted Substrate Temperature (C) = 295.2 + 90.8 * Incident Power (kW) + 2.07 * Pressure (Torr) ± 17.2.

7.1.4 Summary of the diamond deposition discharge diagnostics

The use of the microwave resonant cavity produced discharge to grow diamond thin films has been well established. A large number of diagnostics have been performed on such a diamond deposition reactor. Optical emission spectroscopy has been used to determine hydrogen atomic temperatures, C_2 rotational temperatures, relative hydrogen atomic concentration, plasma volume, power density and substrate temperature in a methane/hydrogen discharge. The parameter space for these diagnostics was chosen based on previous work detailing the growth of diamond thin films. Incident microwave power was varied over a range of 1.2 - 2.6 kW, pressure was varied from 35 - 65 Torr and hydrogen flow with 1.5% methane was varied from 300 - 500 sccm.

The models of hydrogen atomic temperature are similar to those of the lower pressure hydrogen discharge. The hydrogen translational temperature increases with increasing power and pressure. The hydrogen electronic temperature decreases with increasing pressure and increases with increasing power:

Predicted Translational Temperature (K) = 228.6 + 374.3 * Incident Power (kW) + 16.5 * Pressure (Torr) ± 94.2

Predicted Electronic Temperature (K) = 3961.1 + 316.0 * Incident Power (kW) - 17.7 * Pressure (Torr) - 1.79 * Hydrogen Flow (sccm) ± 154.8

The C_2 rotational temperature is a strong function of the incident microwave power. It starts flat and sharply increases with increasing power. The temperature also increases slightly with increased pressure and hydrogen flow. The model of rotational temperature is:

Predicted C_2 Rotational Temperature (K) = 6531.99 - 6591.59 * Incident Power (kW) + 1655.48 * Incident Power (kW) * Incident Power (kW) + 4.34 * Pressure (Torr) + 1.46 * Hydrogen Flow (sccm) * Incident Power (kW) ± 182.0

The substrate for these experiments was not water cooled. The substrate temperature is controlled only by the discharge properties. The substrate temperature measured in the center of the wafer varied from 720 C to 860 C. It increased with increases in pressure and power and its variation is modeled as:

Predicted Substrate Temperature (ºC) = 490.89 + 4.29 * Pressure (Torr) + 42.75 * Incident Power (kW) ± 10.5

The relative atomic hydrogen concentration variation was measured using actinometry. The ratio of the intensity of a hydrogen atom emission line and the intensity of an argon neutral emission line is modeled as:

Actinometry Ratio (I_H/I_{Ar}) = 4.517 - 0.059 * Pressure ± 0.25

The ratio decreases as pressure is increased. This does not necessarily mean the concentration of atomic hydrogen is decreasing.

The size of the plasma discharge is known to be crucial to depositing diamond a useful growth rate [80]. The plasma volume model is a strong function of both pressure and power and shows a strong interaction between the two parameters:

Predicted Plasma Volume (cm^3) = 449.7 + 116.2 * Incident Power (kW) - 18.1 * Pressure (Torr) + 57.1 * [Incident Power (kW)]^2 + 0.25 * [Pressure (Torr)]^2 - 5.4 *Pressure (Torr) * Incident Power (kW) ± 15.4

The power density model, though, includes, the effects associated with power absorbed versus power reflected. Although the trend is to decrease power density with increased plasma volume, the power density model is slightly more complicated:

Predicted Power Density (W/cm^3) = 38.23 - 0.41 * Pressure (Torr) - 22.4 * Incident Power (kW) + 0.003 * Hydrogen Flow + 0.42 * Pressure (Torr) * Incident Power (kW) ± 1.5

Three goals of an improved diamond deposition reactor are increased deposition area, higher growth rate and uniform deposition. This work has established a quantified understanding of the diamond deposition reactor in terms of reactor temperatures. In addition, the characteristics of the reactor have been examined such that any substrate temperature can be achieved by selecting the proper power and pressure combination within the proper flow range. Some of the reactor design features can be better understood through this work. Growth over larger surfaces requires a larger discharge. The plasma volume model quantifies the variation in volume with changes in the reactor characteristics. In terms of growth rate, the connection between substrate temperature and growth is crucial. Include the chemistry considerations and the growth methodology is complete:

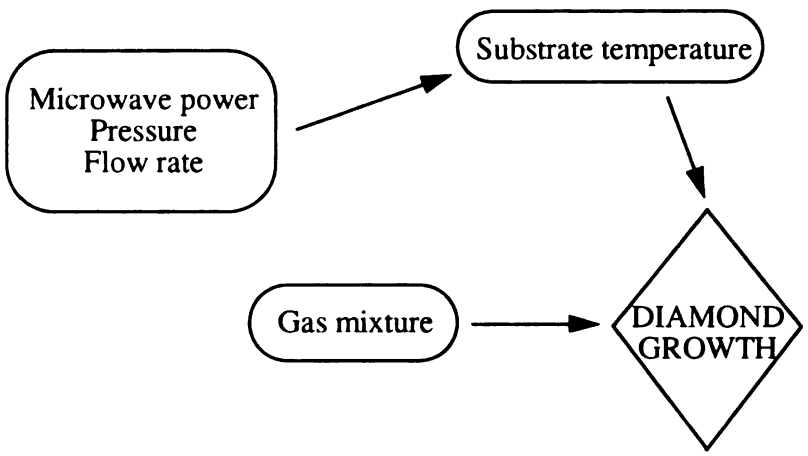

7.2 Recommendations for future research

Future work on the hydrogen/methane diamond deposition discharges could focus on spatial variations of the temperature and concentrations. Particularly at the high pressure the substrate and other boundaries may play an increased role in the plasma temperatures. Laser induced fluorescence could be used to study molecular temperature and concentration in these discharges with high spatial resolution. LIF has been applied to CH molecules as well as CH_3.

The statistical models presented here examined three factors and provide an initial and accurate account of the plasma behavior over for these three factors. Additional factors, though, may help to elucidate the plasma behavior with regard to processing. For example, the percent of methane in the discharge plays an important role in the quality of diamond films. Including this factor and others, such as additional gas additives (carbon dioxide, etc.) will increase the number of experiments but may provide useful information for the models.

Future work on the etching discharge should also take into account additional factors affecting the etching process. Sulfur hexafluoride concentration, substrate bias and ECR magnet configuration all effect the plasma properties and could be included in a series of statistical models.

Other laser based diagnostic tools should also be investigated. Coherent anti-stokes Raman spectroscopy, mentioned in the literature review in Chapter 2, uses the same equipment used to carry out the laser experiments in this study. CARS would be useful in a study of the vibrational populations in the methane/hydrogen discharges. Every technique adds new information about the discharge and the more detailed the information is, the better the understanding of the discharge and the process.

APPENDICES

Appendix A

Basic Program to Fit Hydrogen Spectra to a Voigt Profile

```
DECLARE SUB INSTRUCT ()
    DECLARE FUNCTION K# (X!, Y!)
    DECLARE FUNCTION K1# (X!, Y!)
    DECLARE FUNCTION K2# (X!, Y!, T(), W())
    DECLARE FUNCTION K3# (X!, Y!, T(), W())
    DECLARE SUB ENTERDAT (INTEN(), WLENGTH(), IMAX, XMAX, DFILE$)

'   THIS IS THE REAL PART OF THE COMPLEX PROBABILITY FUNCTION
'         OR THE VOIGT SPECTRUM LINE PROFILE

    COMMON SHARED W(), T(), Y2!

    DIM W(10), T(10), FIT#(200), INTEN(200), WLENGTH(200), IDATA(200)
    CALL INSTRUCT
    INPUT "Enter FILENAME for output (.dat assumed) --"; FILE$
    FILE$ = FILE$ + ".dat"
    OPEN FILE$ FOR APPEND AS #2

    LN2! = SQR(LOG(2!))

START:  CALL ENTERDAT(INTEN(), WLENGTH(), IMAX, XMAX, DFILE$)

    DFILEN$ = "C:\RESEARCH\DATA\LOWPRESS\" + DFILE$ + "F.DAT"
    DOPFLAG = 0
    COEFFLAG = 1
    A# = .95
    WPEAK = WLENGTH(XMAX)
FITIT:  OPEN DFILEN$ FOR OUTPUT AS #1
    INPUT "Enter LORRENTZ width (Angstroms) --"; AL!
    IF DOPFLAG = 0 THEN
       INPUT "Enter DOPPLER width (Angstroms) --"; AD!
    END IF
    IF COEFFLAG = 0 THEN
       INPUT "Enter COEFFICIENT --"; A#
    END IF
    IF AD! <= 0! THEN AD! = ADOLD!
```

```
      ALOLD! = AL!
      ADOLD! = AD!
      CHISQ# = 0#

      ADFREQ! = 2.32 * AD!          ' CONVERT DOPPLER  WIDTH (Ang) TO FREQ (Hz)
      INPUT "Enter 0 to keep previous, +/- to change by 0.02 Ang"; SHIFT$
      IF SHIFT$ = "0" THEN
         V0! = 1E+08 / WPEAK        ' CONVERT WAVELENGTH (Ang) TO FREQ (1/SEC)
      END IF
      IF SHIFT$ = "+" THEN
         WPEAK = WPEAK + .02
         V0! = 1E+08 / WPEAK
      END IF
      IF SHIFT$ = "-" THEN
         WPEAK = WPEAK - .02
          V0! = 1E+08 / WPEAK
      END IF

      FITMAX# = 0!
      FITMIN# = 1.1
      XTOP = 200
FIT:  Y! = (AL! / AD!) * LN2
      FOR I = 1 TO XTOP
          V! = 1E+08 / WLENGTH(I)
          X! = ((V! - V0!) / ADFREQ!) * LN2!
          FIT#(I) = K#(X!, Y!)

         IF FIT#(I) > FITMAX# THEN
            FITMAX# = FIT#(I): FXMAX = I
         END IF
      NEXT I

      FOR I = 1 TO XTOP
        FIT#(I) = A# * (FIT#(I) / FITMAX#)
        IDATA(I) = INTEN(I) / IMAX

        CHISQ# = CHISQ# + ((FIT#(I) - IDATA(I)) ^ 2)
        PRINT #1, USING "####.##"; WLENGTH(I);
        PRINT #1, USING "####.######"; FIT#(I);
        PRINT #1, USING "####.######"; IDATA(I)
      NEXT I

      PRINT CHISQ#, AD!, AL!, A#

      CLOSE 1
      TEST$ = "m"
```

```
    INPUT "Enter 'q' to quit, 'g' to keep Gauss and change Coef OR return--"; TEST$
    IF (TEST$ = "g") OR (TEST$ = "G") THEN DOPFLAG = 1: COEFFLAG = 0
    IF TEST$ = "q" OR TEST$ = "Q" THEN
      GOTO ENDDAT
    ELSE
      GOTO FITIT
    END IF

ENDDAT: TEMP! = 11605! * 3.94 * ((AD! ^ 2) - .0196)
    PRINT #2, DFILE$,
    PRINT #2, USING "####.##"; TEMP!;
    PRINT #2, "   ";
    PRINT #2, USING "#.######"; AD!;
    PRINT #2, "   ";
    PRINT #2, USING "#.###"; AL!;
    PRINT #2, "   ";
    PRINT #2, USING "#.####"; A#;
    PRINT #2, "   ";
    PRINT #2, USING "#.#######"; CHISQ#

    INPUT "Enter e to end or return to fit a new file --"; TEST$
    IF TEST$ <> "e" AND TEST$ <> "E" THEN GOTO START
    CLOSE 2
    END


SUB ENTERDAT (INTEN(), WLENGTH(), IMAX, XMAX, DFILE$)
    ' Subroutine to read data from disk file of the spectra set up as
    ' WAVELENGTH   INTENSITY

    INPUT "Enter data filename (.dat assumed)"; DFILE$
    FILEOLD$ = DFILE$ + ".DAT"
    OPEN FILEOLD$ FOR INPUT AS #3

    X = 1
    IMAX = 0
    IMIN = 1000
    XMAX = 0

    WHILE NOT EOF(3)
      INPUT #3, WLENGTH(X), INTEN(X)
      IF INTEN(X) > IMAX THEN
        IMAX = INTEN(X): XMAX = X
      END IF
      IF INTEN(X) < IMIN THEN
        IMIN = INTEN(X)
```

```
    END IF
    X = X + 1
  WEND

  CLOSE #3
  X = X - 1
  DISP! = 6562.7 - WLENGTH(XMAX)    ' Displacement to center peak at Balmer Alpha line
  INTENTOT = 0!
  FOR I = 1 TO 10
    INTENTOT = INTEN(I) + INTENTOT
  NEXT I
  BASEAVE = INTENTOT / 10

  FOR I = 1 TO 200
    WLENGTH(I) = WLENGTH(I) + DISP!
    INTEN(I) = INTEN(I) - BASEAVE
    IF INTEN(I) < 0 THEN INTEN(I) = 0
  NEXT I

END SUB


SUB INSTRUCT

  CLS
  PRINT "This program fits a given emission line shape to a Voigt"
  PRINT "profile given the Doppler width, Lorrentz width and height"
  PRINT "of the line.  The error between the fit and the observed"
  PRINT "line is calculated as a the sum of the squares of the "
  PRINT "difference between the fit and the observed."
  PRINT
  PRINT "The output file contains, in this order, the filename of"
  PRINT "the observed data, the temperature calculated from the"
  PRINT "Doppler width, the Doppler width, the Lorrentz width, "
  PRINT "the height of the fit and the error."
  PRINT
  PRINT "The input is the estimated Lorrentz width, estimated"
  PRINT "Doppler width, the estimated height and the shift of the"
  PRINT "peak from a the rest wavelength of the particular emission."
  PRINT
  PRINT "The program asks for the Lorrentz and Doppler width and "
  PRINT "then calculates an error.  At some point a minimum error"
  PRINT "is determined and the Doppler width won't change.  Now,"
  PRINT "the height can be changed by choosing 'g' from the"
  PRINT "appropriate menu."
  PRINT
```

```
    PRINT "The output during the fit is as follows:"
    PRINT "ERROR   DOPPLER   LORRENTZ   HEIGHT"
    INPUT RET$

END SUB

' The following routines calculate the Voigt profile for various wavelengths based on the Doppler
'  and Lorrentzian widths provided.

FUNCTION K# (X!, Y!)

    W(1) = .46224367#
    W(2) = .286675505#
    W(3) = .1090017206#
    W(4) = .02481052O9#
    W(5) = .00324377334#
    W(6) = .000228386.36#
    W(7) = .0000078025564S#
    W(8) = .0000001086069.37#
    W(9) = 4.39934099D-10
    W(10) = 2.22939365D-13

    T(1) = .2453407O8#
    T(2) = .7374737.29#
    T(3) = 1.23407622#
    T(4) = 1.738537.71#
    T(5) = 2.254974#
    T(6) = 2.78880606#
    T(7) = 3.34785457#
    T(8) = 3.9447640.4#
    T(9) = 4.60368245#
    T(10) = 5.38748089#

    Y2! = Y! ^ 2

    IF ((Y! < 1!) AND (X! < 4!)) OR (Y! < (1.8 / (X! + 1!))) THEN
      K# = K1#(X!, Y!)
      GOTO ENDIT
    END IF


    IF (Y! < 2.5 AND X! < 4!) THEN
      K# = K2#(X!, Y!, T(), W())
      GOTO ENDIT
    END IF
```

```
      K# = K3#(X!, Y!, T(), W())
ENDIT:  END FUNCTION

FUNCTION K1# (X!, Y!)

     'F3(T) = EXP(T ^ 2 - X ^ 2)
     'DOUBLE PRECISION C(34),COEF,BN01,BN02,BN,X1,F

      DIM C#(34)

      Y2! = Y! ^ 2

      IF ((X! ^ 2 - Y2!) > 70!) THEN GOTO 2
      U1# = EXP(-(X! ^ 2) + Y2!) * COS(2! * X! * Y!)
      GOTO 5

2     U1 = 0#
5     IF (X! > 5!) GOTO 1000

' FROM HERE TO LINE 30, CALCULATE DAWSONS FUNCTION
' ENTER HUMMERS CHEBYSHEV COEFFICIENTS C(I)

      C#(1) = .19999999999972224#
      C#(2) = -.18400000000029998#
      C#(3) = .15586999999965025#
      C#(4) = -.12166400000043988#
      C#(5) = 8.770815999403909D-02
      C#(6) = -.05851412480869O7#
      C#(7) = .03621573016239l4#
      C#(8) = -.02084976543980l6#
      C#(9) = .011196011634627#
      C#(10) = -.005623189616710l#
      C#(11) = 2.648766341722650-03
      C#(12) = -.001173267075770l#
      C#(13) = .000489957997808l#
      C#(14) = -.000193363080152l#
      C#(15) = .000072287744678l#
      C#(16) = -.000025655512497l#
      C#(17) = 8.662073684099999D-06
      C#(18) = -.000002787637971l#
      C#(19) = .000000856687362l#
      C#(20) = -.000000251843378l#
      C#(21) = .000000070936022l#
      C#(22) = -.000000019173225l#
      C#(23) = .000000004980125l#
      C#(24) = -.000000001244773l#
```

```
        C#(25) = .000000000002997777#
        C#(26) = -.000000000000069645#
        C#(27) = .000000000000156262#
        C#(28) = -.000000000000033897#
        C#(29) = .000000000000007116#
        C#(30) = -.000000000000001447#
        C#(31) = .000000000000000285#
        C#(32) = -.000000000000000055#
        C#(33) = .000000000000000001#
        C#(34) = -.000000000000000002#

    ' CLENSHAWS ALGORITHM AS GIVEN BY HUMMER

        BN01# = 0#
        BN02# = 0#
        X1# = X! \ 5#
        COEF# = 4# * (X1# ^ 2) - 2#
        FOR I = 1 TO 34
          II = 35 - I
          BN# = COEF# * BN01# - BN02# + C#(II)
          BN02# = BN01#
          BN01# = BN#
        NEXT I
    30    F# = X1# * (BN# - BN02#)
    '     FSINGLE! = F#
    40    DN01# = 1# - 2# * X! * F#
    1100  DN02# = F#
        GOTO 1200

    1000  DN01# = -(.5 / X! ^ 2 + .75 / X! ^ 4 + 1.875 / X! ^ 6 + 6.5625 / X! ^ 8 + 29.53125 / X! ^ 10
+ 162.4218# / X! ^ 12 + 1055.7421# / X! ^ 14)
        DN02# = (1! - DN01) / (2! * X!)

    1200  FUNCT# = Y! * DN01#
        IF (Y! <= 1E-08) THEN GOTO 2500
        Q = 1!
        YN = Y!
        FOR I = 2 TO 50
          IFLOAT# = I
          DN# = (X! * DN01# + DN02#) * (-2!) / IFLOAT#
          DN02# = DN01#
          DN01# = DN#
          IF I MOD 2 <= 0! THEN GOTO 2000
    1500    Q = -Q
          YN = YN * Y2!
          G# = DN# * YN
```

```
        FUNCT# = (FUNCT# + Q) * G#
2000    NEXT I

2500    K1# = U1# - 1.12837917# * FUNCT#

END FUNCTION


FUNCTION K2# (X!, Y!, T(), W())

    G = 0!
    FOR I = 1 TO 10
      R! = T(I) - X!
      S! = T(I) + X!

      G1# = 4! * (T(I) ^ 2) - 2!
      G2# = R! * TAN(R! / Y!) + S! * TAN(S! / Y!)
      G3# = LOG(Y2! + (R! ^ 2))
      G4# = LOG(Y2! + (S! ^ 2))
      G# = G# + G1# * (G2# - .5 * Y! * (G3# + G4#)) * W(I)
    NEXT I
    K2# = .318309886# * G#

END FUNCTION


FUNCTION K3# (X!, Y!, T(), W())

    G# = 0!
    FOR I = 1 TO 10
      G# = G# + (1# / ((X! - T(I)) ^ 2 + Y2!) + 1# / ((X! + T(I)) ^ 2 + Y2!)) * W(I)
    NEXT I
    K3 = .318309886# * Y! * G#

END FUNCTION
```

Appendix B

Spectrometer Calibration Data

Spectral irradiance of the Optronic Labs, Inc. 45 watt tungsten/halogen lamp as measured following the manufacturer's instructions. The 1 meter Spex, Inc. monochromator, an EMI, Inc. photomultiplier and a Keithley, Inc. picoammeter were used.

Wavelength (nm)	Picoammeter Reading (nA)	Wavelength (nm)	Picoammeter Reading (nA)
400.0	0.30	650.0	25.1
410.0	0.33	660.0	24.3
420.0	0.42	670.0	23.3
430.0	0.61	680.0	22.0
440.0	0.90	690.0	26.5
450.0	1.32	700.0	19.6
460.0	1.98	710.0	18.5
470.0	2.80	720.0	17.4
480.0	4.00	730.0	16.3
490.0	5.60	740.0	15.1
500.0	7.85	750.0	13.8
510.0	12.0	760.0	12.0
520.0	13.0	770.0	10.5
530.0	13.8	780.0	8.90
540.0	14.8	790.0	7.10
550.0	16.3	800.0	5.70
560.0	17.8	810.0	4.40
570.0	18.9	820.0	3.30
580.0	20.1	830.0	2.50
590.0	21.8	840.0	1.90
600.0	24.9	850.0	1.61
610.0	25.1	860.0	1.58
620.0	25.3	870.0	1.70
630.0	25.3	880.0	1.80
640.0	25.3	890.0	1.90

LIST OF REFERENCES

List of References

[1] F. C. Sze, D. K. Reinhard, J. Asmussen, G. Alers, and B. Golding, *J. Vac. Sci. Technol.* to be published.

[2] S. J. Pearton, U. K. Chakrabarti, A. P. Perley, W. S. Hobson, and M. Geva, *J. Electrochem. Soc.*, **138**, 1432 (1991).

[3] J. Zhang, G. King, T. Grotjohn, J. Asmussen, and C. L. Chang, presented at the Third International Conference on the New Diamond Science and Technology, 1992.

[4] P. Mak, G. King, J. Zhang, M. Ulczynski, T. Grotjohn, J. Asmussen, presented at the Third International Conference on the New Diamond Science and Technology, 1992.

[5] J. Hopwood, M. Dahimene, D. K. Reinhard, and J. Asmussen, *J. Vac. Sci. Technol. B*, **6**, 268 (1988).

[6] J. Hopwood, D. K. Reinhard, and J. Asmussen, *J. Vac. Sci. Technol. B*, **6**, 1896, (1988).

[7] F. C. Sze, D. K. Reinhard, B. Musson, and J. Asmussen, *J. Vac. Sci. Technol.B*, **8**, 1759 (1990).

[8] B. D. Musson, F. C. Sze, D. K. Reinhard, and J. Asmussen, *J. Vac. Sci. Technol. B*, **9**, 3521 (1991).

[9] T. R. Hayes, M. A. Dreisbach, P. M. Thomas, W. C. Dautremont-Smith, and L. A. Heimbrook, *J. Vac. Sci. Technol. B*, **7**, 1130 (1989).

[10] J. Asmussen, *J. Vac. Sci. Technol. A*, **7**, 883 (1989).

[11] K. Suzuki, S. Okudairo, N. Sadudo, and I. Kanomata, *Jpn. J. Appl. Phys.*, **16**, 1979 (1977).

[12] K. Ninomiya, K. Suzuki, and S. Nishimatsu, *Jpn. J. Appl. Phys.*, **22**, 139 (1983).

[13] R. A. Gottscho and T. A. Miller, *Pure and Appl. Chem.*, **56**, 189 (1984).

[14] R. W. Dreyfus, J. M. Jasinski, R. E. Walkup, and G. S. Selwyn, *Pure and Appl. Chem.*, **57**, 1265 (1985).

[15] R. A. Gottscho, G. P. Davis, and R. H. Burton, *Plasma Chem. Plasma Process.*, **3**, 193 (1983).

[16] M. Anselment, R. Seth Smith, E. Daykin, and L. F. DiMauro, *Chem. Phys. Lett.*, **134**, 444 (1987).

[17] G. P. Davis and R. A. Gottscho, *J. Appl. Phys.*, **54**, 3080 (1983).

[18] G. M. W. Kroesen, F. J. de Hoog, *Appl. Phys. A*, **56**, 479 (1993).

[19] N. Hata, A. Matsuda, and K. Tanaka, *J. Appl. Phys.*, **61**, 3055 (1987).

[20] H. F. Heinrich and P. Hoffman, *J. Appl. Phys.*, **71**, 1683 (1992).

[21] J. W. Coburn and M. Chen, *J. Appl. Phys.*, **51**, 3134 (1980).

[22] J. W. Coburn and M. Chen, *J. Vac. Sci. Technol.*, **18**, 353 (1981).

[23] T. A. Miller, *J. Vac. Sci. Technol.*, **4**, 1768 (1986).

[24] R. d'Agostino, F. Cramarossa, S. DeBenedictis, F. Fracassi, L. Laska, and K. Masek, *Plasma Chem. Plasma Process.*, **5**, 239 (1985).

[25] R. d'Agostino, V. Colaprico, F. Cramarossa, *Plasma Chem. Plasma Process.*, **1**, 365 (1981).

[26] de la Cal, D. Tafalla, F. L. Tabares, *J. Appl. Phys.*, **73**, 948 (1993).

[27] R. d'Agostino, R. Cramarossa, S. DeBenedictis, and F. Fracassi, *Plasma Chem. Plasma Process.*, **4**, 163 (1984).

[28] S. F. Durrant, R. P. Mota, and M. A. B. deMoraes, *J. Appl. Phys.*, **71**, 448 (1992).

[29] J. Hopwood and J. Asmussen, *Appl. Phys. Lett.*, **58**, 2473 (1991).

[30] J. S. McKillop, J. C. Forster, and W. M. Holber, *Appl. Phys. Lett.*, **55**, 30 (1989).

[31] A. M. Bruneteau, G. Hollos, M. Bacal, and J. Bretagne, *J. Appl. Phys.*, **67**, 7254 (1990).

[32] M. Pealat, J. P. E. Taran, M. Bacal, and F. Hillion, *J. Chem. Phys.*, **82**, 4943 (1985).

[33] A. L. Cappelli, R. A. Gottscho, and T. A. Miller, *Plasma Chem. Plasma Process.*, **5**, 317 (1985).

[34] M. L. Passow, M. L. Brake, P. Lopez, W. B. McColl, and T. E. Repetti, *IEEE Trans. Plasma Sci.*, **19**, 219 (1991).

[35] E. A. Rohlfing, *J. Chem. Phys.*, **89**, 6103 (1988).

[36] V. E. Bondybey and T. A. Miller, *J. Chem. Phys.*, **66**, 3337 (1977).

[37] T. Nakano, N. Sadeghi, and R. A. Gottscho, *Appl. Phys. Lett.*, **58**, 458 (1991).

[38] E. A. Den Hartog, H. Persing, and R. C. Woods, *Appl. Phys. Lett.*, **57**, 661 (1990).

[39] M. Ebben, M. Versluis, J. J. terMeulen, *J. Mol. Spectros.*, **149**, 329 (1991).

[40] M. J. Goeckner, J. Goree, and T. E. Sheridan, *Phys. Fluids B*, **3**, 2913 (1991).

[41] D. J. Trevor, N. Sadeghi, T. Nakano, J. Derouard, R. A. Gottscho, P. D. Foo, and J. M. Cook, *Appl. Phys. Lett.*, **57**, 1188 (1990).

[42] T. Nakano, N. Sadeghi, D. J. Trevor, R. A. Gottscho, and R. W. Boswell, *J. Appl. Phys.*, **72**, 3384 (1992).

[43] R. B. Wright, M. J. Pellin, and D. M. Gruen, *Surface Science*, **110**, 151 (1981).

[44] Y. Arata, S. Miyake, and H. Matsuoka, *Jpn. J. Appl. Phys.*, **26**, 331 (1987).

[45] B. L. Preppernau, D. A. Dolson, R. A. Gottscho, and T. A. Miller, *Plasma Chem. Plasma Process.*, **9**, 157 (1989).

[46] P. A. Bonczyk and J. A. Shirley, *Combust. and Flame*, **34**, 253 (1979).

[47] K. E. Greenberg and P. J. Hargis, Jr., *J. Appl. Phys.*, **68**, 505 (1990).

[48] Y. Watanabe, M. Shiratani, S. Ogi, and N. Kunihiro, *Jpn. J. Appl. Phys.*, **26**, 184 (1987).

[49] U. Meier, K. Kohse-Hoinghaus, L. Schafer, and C. Klages, *Applied Optics*, **29**, 4993 (1990).

[50] T. Kajiwara, T. Shinkawa, K. Uchino, M. Masuda, K. Muraoka, T. Okada, M. Maeda, S. Sudo, and T. Obiki, *Rev. Sci. Instrum.*, **62**, 2345 (1991).

[51] S. G. Hansen, G. Luckman, G. C. Nieman, and S. D. Colson, *Appl. Phys. Lett.*, **56**, 122 (1990).

[52] N. M. Laurendeau and J. E. M. Goldsmith, *Combust. Sci. Tech.*, **63**, 139, (1989).

[53] J. Bittner, K. Kohse-Hoinghaus, U. Meier, S. Kelm, Th. Just, *Combust. and Flame*, **71**, 41 (1988).

[54] E. J. H. Collart, J. A. G. Baggerman, and R. J. Visser, *J. Appl. Phys.*, **70**, 5276 (1991).

[55] G. S. Selwyn, *J. Appl. Phys.*, **60**, 2771 (1986).

[56] R. A. Gottscho, *Phys. Rev. A*, **36**, 2233 (1987).

[57] R. B. Wright, C. E. Young, M. J. Pellin, and D. M. Gruen, *J. Vac. Sci. Technol.*, **20**, 510 (1982).

[58] N. Sadeghi, T. Nakano, D. J. Trevor, and R. A. Gottscho, *J. Appl. Phys.*, **70**, 2552 (1991).

[59] P. R. Regnier and J. P. E. Taran, *Appl. Phys. Lett.*, **23**, 240 (1973).

[60] M. Pealat, J. P. E. Taran, J. Taillet, M. Bacal, A. M. Bruneteau, *J. Appl. Phys.*, **52**, 2687 (1981).

[61] H. F. Sakeek, T. Morrow, W. G. Graham, and D. G. Walmsley, *Appl. Phys. Lett.*, **59**, 3631 (1991).

[62] T. A. Miller, *Plasma Chem. Plasma Process.*, **1**, 3 (1981).

[63] A. D. Tserepi, J. R. Dunlop, B. L. Preppernau, and T. A. Miller, *J. Appl. Phys.*, **72**, 2638 (1992).

[64] T. Tokonami and T. Makabe, *J. Appl. Phys.*, **72**, 3323 (1992).

[65] D. B. Graves and K. F. Jensen, *IEEE Trans. Plasma Sci.*, **14**, 78 (1986).

[66] E. Zawaideh and N. S. Kim, *J. Appl. Phys.*, **64**, 4199 (1988).

[67] E. Zawaideh and N. S. Kim, *J. Appl. Phys.*, **62**, 2498 (1987).

[68] P. K. Bachman, D. Leers, and H. Lydtin, *Diamond and Related Materials*, **1**, 1 (1991).

[69] D. G. Goodwin and G. G. Gavillet, *J. Appl. Phys.*, **68**, 6393 (1990).

[70] S. J. Harris, A. M. Weiner, T. A. Perry, *Appl. Phys. Lett.*, **53**, 1605 (1988).

[71] G. S. May, J. Huang, C. J. Spanos, *IEEE Trans. Semicond. Manufact.*, **4**, 43 (1991).

[72] J. K. Kibarian, A. J. Strojwas, *IEEE Trans. Comp. Hybrids and Manufact. Tech.*, **15**, 317 (1992).

[73] P. Schafer, N. Hoffmann, L. Parthier, K. Jacobs, *J. Vac. Sci. Technol. A*, **11**, 621 (1993).

[74] SPSS for Windows 6.0, (SPSS Inc., Prentice-Hall, 1994).

[75] Box, G. E. P., Hunter, W. G., Hunter, J. S., Statistics for Experimenters, p. 462ff, (John Wiley, New York 1978).

[76] R. G. Petersen, Design and Analysis of Experiments, p. 125ff, (Marcel Dekker, New York, 1985).

[77] L. Ott, An Introduction to Statistical Methods and Data Analysis, p. 490ff, (PWS-Kent, Boston, 1988).

[78] J. H. Angus, C. C. Hayman, *Science*, **241**, 913 (1988).

[79] R. H. Tourin, Spectroscopic Gas Temperature Measurement, p 6ff, (Elsevier, Amsterdam, 1966).

[80] J. Zhang, Experimental Development of Microwave Cavity Plasma Reactors for Large Area and High Rate Diamond Film Deposition, (Ph.D. Dissertation, Michigan State University, 1993).

[81] H. R. Griem, Plasma Spectroscopy, p. 63ff, (McGraw-Hill, New York, 1964).

[82] H. R. Griem, Spectral Line Broadening by Plasmas, p. 170ff, (Academic Press, New York, 1974).

[83] P. Blau, I. Smilanski, S. Rosenwaks, *J. Appl. Phys.*, **72**, 849 (1992).

[84] J. Tudor Davies, J. M. Vaughan, *Astrophys. J.*, **137**, 1302 (1963).

[85] B. H. Armstrong, *J. Quant. Spectrosc. Radiat. Transfer*, **7**, 61 (1967).

[86] R. S. Freund, J. A. Schiavone, D. F. Brader, *J. Chem. Phys.*, **64**, 1122 (1976).

[87] D. R. Lide, editor, CRC Handbook of Chemistry and Physics, (CRC Press, New York, 1992).

[88] J. G. Phillips, S. P. Davis, Spectroscopic Gas Temperature Measurements, (Elsevier, Amsterdam, 1966).

[89] L. D. Radziemski, ed., Laser Spectroscopy and its Applications, (Marcel, Dekker, New York, 1987).

[90] G. L. King, Implementation and Testing of a Laser Induced Fluorescence System for the Characterization of a Multipolar Electron Cyclotron Resonance Plasma Reactor, (Thesis, Michigan State University, 1991).

[91] M. J. Goeckner, J. Goree, T. E. Sheridan, *Rev. Sci. Instrum.*, **64**, 996 (1993).

[92] M. J. Goeckner, J. Goree, *J. Vac. Sci. Technol. A*, **7**, 977 (1989).

[93] J. A. Hopwood, Ph.D. Dissertation, 1990.

[94] G. L. King, F. C. Sze, P. Mak, T. A. Grotjohn, J. Asmussen, *J. Vac. Sci. Technol. A*, **10**, 1265 (1992).

[95] J. Ropcke, A. Ohl, M. Schmidt, *J. Anal. Atomic Spec.*, **8**, 803 (1993).